This is to certify that the
dissertation entitled

DESIGN, ANALYSIS AND OPERATION OF PMSMS
FOR HEV APPLICATIONS

presented by

Abdul Rehman Tariq

has been accepted towards fulfillment
of the requirements for the

Ph.D. degree in Electrical Engineering

E G Strangas

Major Professor's Signature

December 7, 2010

Date

PLACE IN RETURN BOX to remove this checkout from your record.
TO AVOID FINES return on or before date due.
MAY BE RECALLED with earlier due date if requested.

DATE DUE	DATE DUE	DATE DUE

DESIGN, ANALYSIS AND OPERATION OF IPMSMS FOR HEV APPLICATIONS

By

Abdul Rehman Tariq

A DISSERTATION

Submitted to
Michigan State University
in partial fulfillment of the requirements
for the degree of

DOCTOR OF PHILOSOPHY

Electrical Engineering

2010

ABSTRACT

DESIGN, ANALYSIS AND OPERATION OF IPMSMS FOR HEV APPLICATIONS

By

Abdul Rehman Tariq

Energy conservation and clean environment are the basic driving factors for the development of Hybrid and Electrical Vehicles (HEVs). Efficient electrical machines are one of the key components of HEVs. Interior Permanent Magnet Synchronous Machines (IPMSMs) are getting more room in the vehicle industry due to their high power density, wide speed range and high efficiency. This document presents the different aspects of the design, analysis and operation IPMSMs for HEVs applications. Finite Element Method (FEM) and analytical methods are used for performance analysis. The issues addressed are efficient machine design for a specific driving cycle, quantitative analysis of machine's performance under overload conditions, effect of magnet materials on machine design and an analytical framework for faster calculation of machine losses and torque.

An efficient design of IPMSM is proposed for series hybrid bus based upon the maximization of the Average Driving Cycle Efficiency (ADCE) for a typical urban driving cycle. An optimized machine design is the outcome of many design iterations and procedure involves FEM analysis for every design. Design iterations were tuned for machine geometry and winding topology. Torque speed envelopes and efficiency maps were computed by post processing of the FEM simulations data and Matlab programming. Inverter losses and the power required for machine and inverter cooling was also included in the computation of ADCE.

A method based upon the quantitative analysis is suggested to design and evaluate the performance of an IPMSM under overload conditions with increased cooling. Issues of demagnetization of the magnets and the current magnitude and angle limits were calculated using the FEM. The procedure was demonstrated to design and analyze an IPMSM to maximize the overloading capacity.

An analysis is presented for performance evaluation of high power density IPMSMs for elevated operating temperature using different magnet materials. The effect of change in the characteristics of the permanent magnets with temperature variation is taken into account in the design evaluation. NdFeB and SmCo magnet machines can be designed for a specific temperature range. The availability of rare earth magnet materials (NdFeB and SmCo) across the world at affordable cost, is becoming an issue. In this situation, the ferrite magnets could be the only option for design of high power density PM machines. Different machine designs including IPM and flux squeeze were analyzed and their performance is compared to explore an efficient machine design using ferrite magnets.

FEM takes hours to set up, run and data post-processing of the experiments for every iteration. An iterative method based upon large elements and Magnetic Equivalent Circuit (MEC) of the machine is developed to reject out the relatively non-efficient designs at early stage of the design optimization. It encompasses the time stepping transient solution of the magnetic scalar potential of a set of equations derived from the MEC of an IPMSM. Finally, losses and efficiency of the machine were calculated from magnetic scalar potential of MEC nodes in much reduced time than required by the FEM.

Six PMSMs are designed and manufactured during this research work. First IPMSM is in use for various experiments in the machines test laboratory for more than two years. Three more machines are built using different magnet materials (one each of NdFeB, SmCo and ferrite magnets) in the housing of off the shelf induction machines. Two high power, water cooled IPMSMs were designed for the power train of series hybrid bus and their manufacturing was arranged through a vendor.

DEDICATION

Dedicated to my family i.e. my wife, son, daughter, parents, brothers and sisters.

ACKNOWLEDGMENT

First of all, all praise and thanks to Allah (God) almighty, the most beneficent, the most merciful, who is the creator and controller of the universe and with his will, I was able to complete this task.

I would like to express my infinite gratitude to my advisor, Prof. Elias G. Strangas, for his guidance and support throughout my studies at MSU. His tremendous efforts to transform my engineering attitude towards research will always be remembered. He always maintained a friendly environment in the discussions related to research work as well as current affairs of the world.

My deep thanks to the committee members Prof. Fang Z. Peng, Prof. Guoming Zhu and Prof. André Benard for their time and valuable inputs. It helped a lot to improve my confidence level and presentation of the research work. I also owe special thanks to my favorite grad school teacher, Prof. Hassan Khalil, who inspired me to rejoin MSU for PhD after four years of my Masters.

Particular thanks to all my colleagues and friends with whom I spent my time in technical and non-technical discussions during my stay at MSU, and who helped me in manufacturing of machines. They are Carlos Nino, Sajjad Zaidi, Qaiser Malik, Xuefei Chen, Jianping Gao, Jinxin Fan, Waqar Qureshi, Ahmed Majeed Khan, Shanelle Foster, Arslan Qaiser, Jawad Zaheer, Andrew Babel, Eduardo Montalvoortiz, Awais Kamboh, Ramin Amiri and many others. I would also like to thank my undergrad, college and high school teachers and friends, who helped in my studies at different levels. Although, life has taken us to different paths, I am still grateful to them to help set my knowledge base for higher studies.

My many thanks to my wife Aliya, son Ali and daughter Qudsia for maintaining happy and wonderful family life for me, and helping me to do my research work. My this stay for studies abroad would have been very tough and arduous without all of them. I appreciate their patience for my reduced family time due to my commitments related to the studies and research.

My special thanks to my parents, brothers, sisters, nephews and nieces for their support and prayers, and who had been waiting for me to come back home after completion of my studies so that I can share with them the happiness and sorrows of their lives. I can not forget my dear mother who passed away while waiting for my return back to my home country. May her soul rest in peace and may Allah bless her a nice place in the heavens in the hereafter.

TABLE OF CONTENTS

LIST OF TABLES

LIST OF FIGURES

Chapter 1

Preamble

1.1 Synopsis and Objectives

Energy conservation and clean environment are the driving factors for the development of hybrid and electrical vehicles (HEVs). High power efficient electrical machines are the key components of the HEVs. Interior Permanent Magnet Synchronous Machines (IPMSMs) are widely used in the vehicle industry due to their high power density, wide speed range and high efficiency. Since HEVs will share a significant part of the automobile market in near future, more investigation is being carried out for deployment of IPMSMs. This document presents the research work done in the area of design and performance analysis of IPMSMs.

Design of an efficient machine for a specific application in reduced time is always the need for timely completion of the development projects. Efficiency of IPMSMs varies in its operating range defined by torque and speed. The torque speed requirements of the traction machines also vary for different vehicles and driving cycles. Efficiency of the complete driving cycle of the traction drive is more important machine design parameter than the efficiency of traction machine at one operating point. The optimum machine design (having maximum efficiency for the complete driving cycle) needs many iterations and Finite Element Method (FEM) based upon solving a set of electromagnetic equations in time domain takes long time for each design iteration. A fast but relatively less accurate method than FEM is presented here to calculate the iron and magnet losses and torque of IPMSMs. Machine operation limits in terms of maximum overload current and magnet demagnetization are also studied to evaluate the machine performance under various operating conditions.

1.2 Principal Contributions

This thesis presents the research work in the area of efficient design, analysis and operation of the IPMSM for hybrid vehicle application. The major contributions of the research work are the followings:

1.2.1 Design of IPMSM based upon ADCE

Average Driving Cycle Efficiency (ADCE) is the efficiency of traction drive that depends upon the energy consumption during the complete driving cycle of the vehicle. A method is worked out for the calculation of ADCE of a series hybrid bus. In this regard, the coefficients of iron losses were calculated from the manufacturer's data of iron laminations. Computation of iron and magnets losses was carried out with using FEM.

1.2.2 Machine operation overload

A frame work based upon the quantitative analysis of machine's operation under overload conditions is presented to evaluate its performance with increased cooling. Issues of demagnetization of the magnets and the current angle limits with varying machine load current are calculated using FEM. A method is proposed to design an IPMSM for higher overloading capacity.

1.2.3 Effect of magnet materials on design of PMSMs

An analysis is presented to evaluate the performance of PMSMs for elevated temperature applications. It provides in-depth understanding of the usage of the different magnet materials for a specific design requirement. Furthermore, the machine design options are explored for design of high power density PMSMs without using rare earth magnet materials. Ferrite magnets are used in interior magnet as well as in the flux squeeze design, and feasible design options are proposed in case of unavailability of rare earth magnets.

1.2.4 Acceleration of machine design

An iterative numerical method based upon the Magnetic Equivalent Circuit (MEC) of an IPMSM is formulated for calculation of iron and magnet losses and torque in reduced time than the FEM. IPMSMs, especially those having multilayered magnets and non-symmetric elements of rotor geometry, operate in deeper saturation than induction and switched reluctance machines. Iron and magnet losses calculation of IPMSM using MEC has not been explored much in the past and this work contributes towards this objective. The proposed method is aimed to be fast and have comparable results with that of the FEM. The machine geometry is entered to a Matlab based program that solves the MEC of IPMSM considering the non-linearities in the lamination material due to magnetic saturation. In order to have its true modeling, manufacturer's supplied BH curve is used instead higher order polynomials approximations.

1.3 Organization of Thesis

Chapter 2 presents the basic configurations of HEVs and IPMSMs. It gives an overview of hybrid vehicles, configuration of PMSM and their winding distribution. Mathematical dq axis model of a PMSM is discussed for efficient machine operation. Chapter 3 describes about the partial differential equations associated with the electromagnetic principles of electrical machines and machine design procedure using the FEM. It also presents the cross saturated model of PMSM and calculation of copper, iron and magnet losses.

Chapter 4 presents a procedure for machine design and evaluation based upon the ADCE of the traction drive. The cross saturated model of IPMSM was used to calculate the current and its angle for efficient machine operation. Chapter 5 describes the quantitative analysis of IPMSMs for its overload conditions. Considering magnet demagnetization, the safe operating region in terms of current, its angle and torque speed range is explained. Design consideration are also presented for IPMSMs that can be overloaded to its maximum level.

Chapter 6 mentions the design consideration using different magnet materials for elevated operating temperatures. The variation in the magnet properties and their demagnetization characteristics are explained. Comparison of torque speed envelope and efficiency is presented for machines designed for a specific application. Furthermore, the design of high power density PMSMs are explored without using rare earth magnet materials. Ferrite magnets are used in different designs to achieve maximum possible power density.

An analytical method based upon the MEC is discussed for IPMSMs to calculate iron and magnet losses and torque in Chapter 7. The proposed method is applied to two different machines, and results are compared with those of the FEM. Chapter 8 gives the summary of and discusses the future work. The experimental work that includes desiging, building and testing of the various PMSMs are described in Appendix A.

Chapter 2

Background

Energy conservation needs of the world are the driving factor for the minimization of the energy losses. Significant losses occur in energy conversion devices. Automobiles constitute a very vast segment of energy consumption devices and the majority of the vehicles are driven by converting the chemical energy of gasoline to mechanical energy of the wheels by Internal Combustion Engines (ICEs). Due to low efficiency of engines, a significant portion of the energy is converted into heat.

Hybrid and Electric Vehicles (HEVs) utilize an electric motor as well as an ICE to provide efficient operation and to reduce the emissions pollution. Vehicle design complexity increases in hybrid vehicles due to sophisticated control and power mixing from two energy sources.

2.1 Configurations of HEVs

There are two basic configurations of the hybrid vehicles, series and parallel hybrid. In series hybrid, one only energy converter provides the propulsion power. The ICE drives an electrical generator that delivers the power to energy storage devices and propulsion motor. The system configuration of series hybrid vehicle is shown in Fig.2.1. In parallel hybrid,

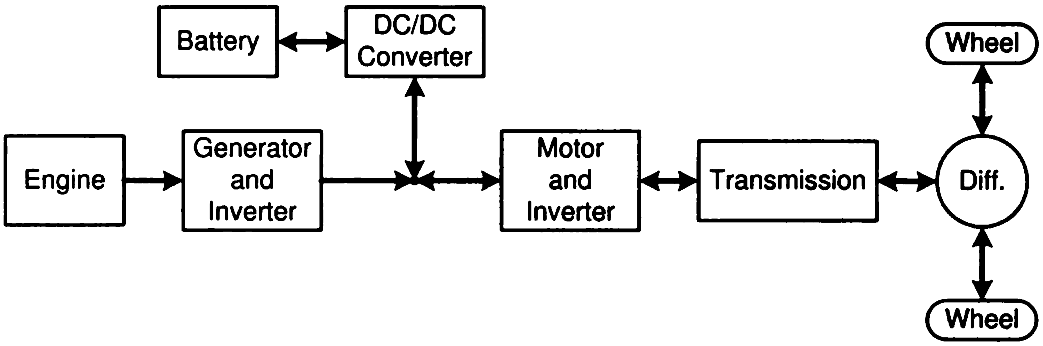

Figure 2.1: Series hybrid configuration

more than one energy source can provide the propulsion power. ICE and electric motor are configured in parallel with a mechanical coupling that combines the torque produced by two sources. The system configuration of parallel hybrid vehicles is shown in Fig. 2.2.

In the series hybrid configuration, the entire mechanical energy from the engine is converted into electrical energy, and the traction machine solely produces the mechanical energy required for vehicle motion and its acceleration. The traction drive has relatively large size because it has to provide sufficient torque for acceleration. A downsized engine drives the generator, which supplies electrical power to the traction motor. The generator also charges the batteries when they are below than a certain state of charge. The traction motor returns energy to the batteries/capacitor during braking.

In the parallel hybrid configuration, the engine and motor are connected to the drive shaft through planetary gears. Power requirements of the motor in parallel hybrid is much

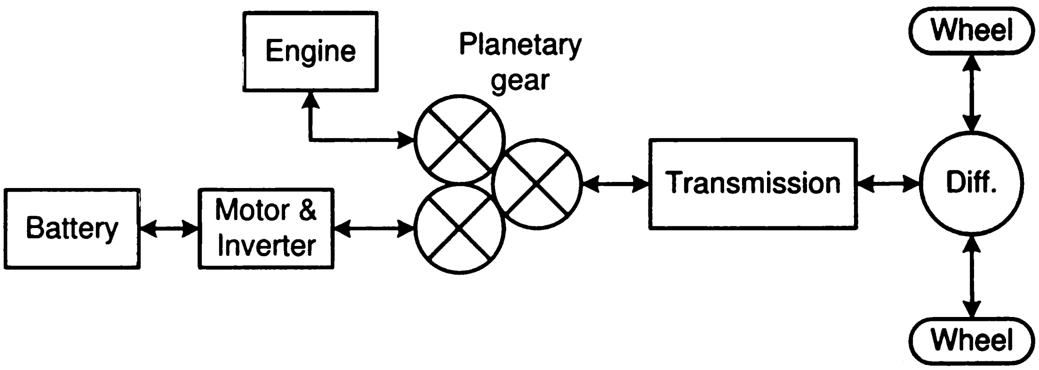

Figure 2.2: Parallel hybrid configuration

lower than that of a series hybrid because engine complements for total power requirement of the vehicle. The propulsion power may be supplied by engine or battery or by both of them together.

Series/parallel hybrid configuration or their combination can be used in a vehicle and selection depends on the system operation to minimize the energy losses. Series hybrid configuration is more suitable for an urban bus, which operates at lower speed and stops frequently. Energy transformation from mechanical to electrical form and vice versa happens by electrical devices and they are more efficient than conventional engines and mechanical energy transformation devices. To maximize the efficiency of a series hybrid bus, all subsystems (engine, generator, motor etc.) have to be designed and operated at their efficient operating range. Efficient electrical machines are one of the key components of the hybrid vehicles.

2.2 Permanent Magnet Synchronous Machines

Electric drives are categorized based upon their operating principles. Conventional DC, synchronous and induction machines are relatively less efficient machines. Permanent magnet brushless DC and Permanent Magnet Synchronous Machines (PMSMs) have permanent magnets in them and exhibit high power density and efficiency despite of the additional electronics required for their operation. PMSMs are replacing other electrical machines rapidly, especially in the vehicle industry due to their low losses, easy control and wide speed range. They are more suitable in the applications requiring reduced volume e.g. automotive, aircraft, and portable generator industries.

Three phase PMSMs are basically AC machines that have three phase windings in the stator slots. The windings current is approximately sinusoidal and produces a rotating space vector of the magnetic flux. There are magnets in the rotor that produce a constant flux. Based upon the rotational construction, there are two configurations of PMSMs; interior

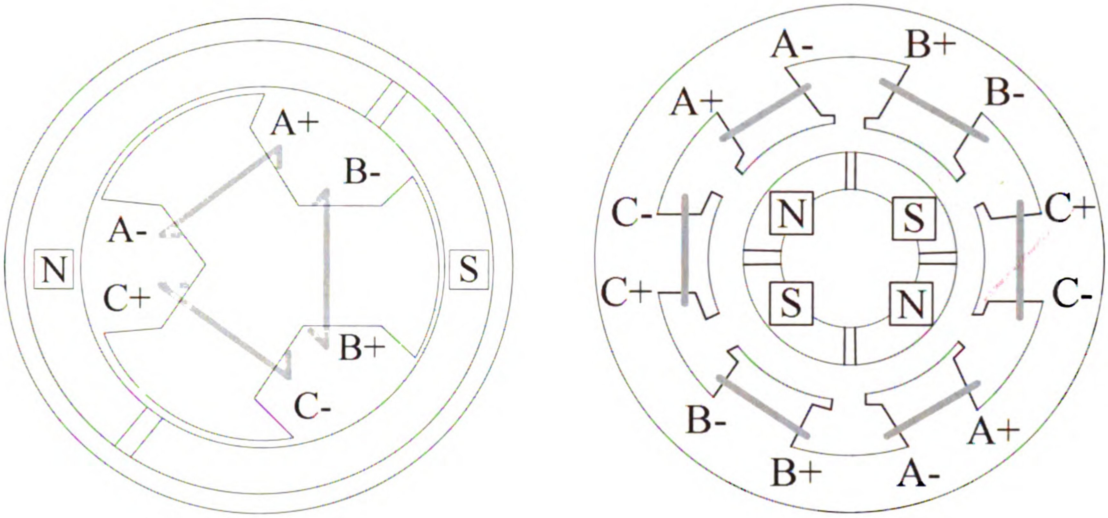

(a) Exterior Rotor (b) Interior Rotor

Figure 2.3: General configuration of PMSMs

and exterior rotor as shown in Figure 2.3.

2.2.1 Location of permanent magnets

Permanent magnets can be installed on the rotor in several configurations. Their location affects the characteristics of the machine, maximum torque, maximum speed and power density. Based upon the rotor magnets configuration, the PMSM can be: Surface PMSM, Inset PMSM and Interior PMSM as shown in Figure 2.4.

In a surface magnet motor the magnets are usually magnetized radially. Since the permeability of rare-earth magnets is almost equal to that of the air, d and q axis inductances are usually considered to be equal. This offers simple construction of the motor, which is less expensive because the magnets can be attached to the rotor surface.

Inset PM rotor has its magnets in the cavities on the rotor surface. It provides an additional component of the torque due to saliency. Its construction is relatively more complex than surface PM. However, in case of interior rotor machine for both surface and inset PM machines, keeping the magnets on the shaft against centrifugal force is an additional issue to consider in the machine design.

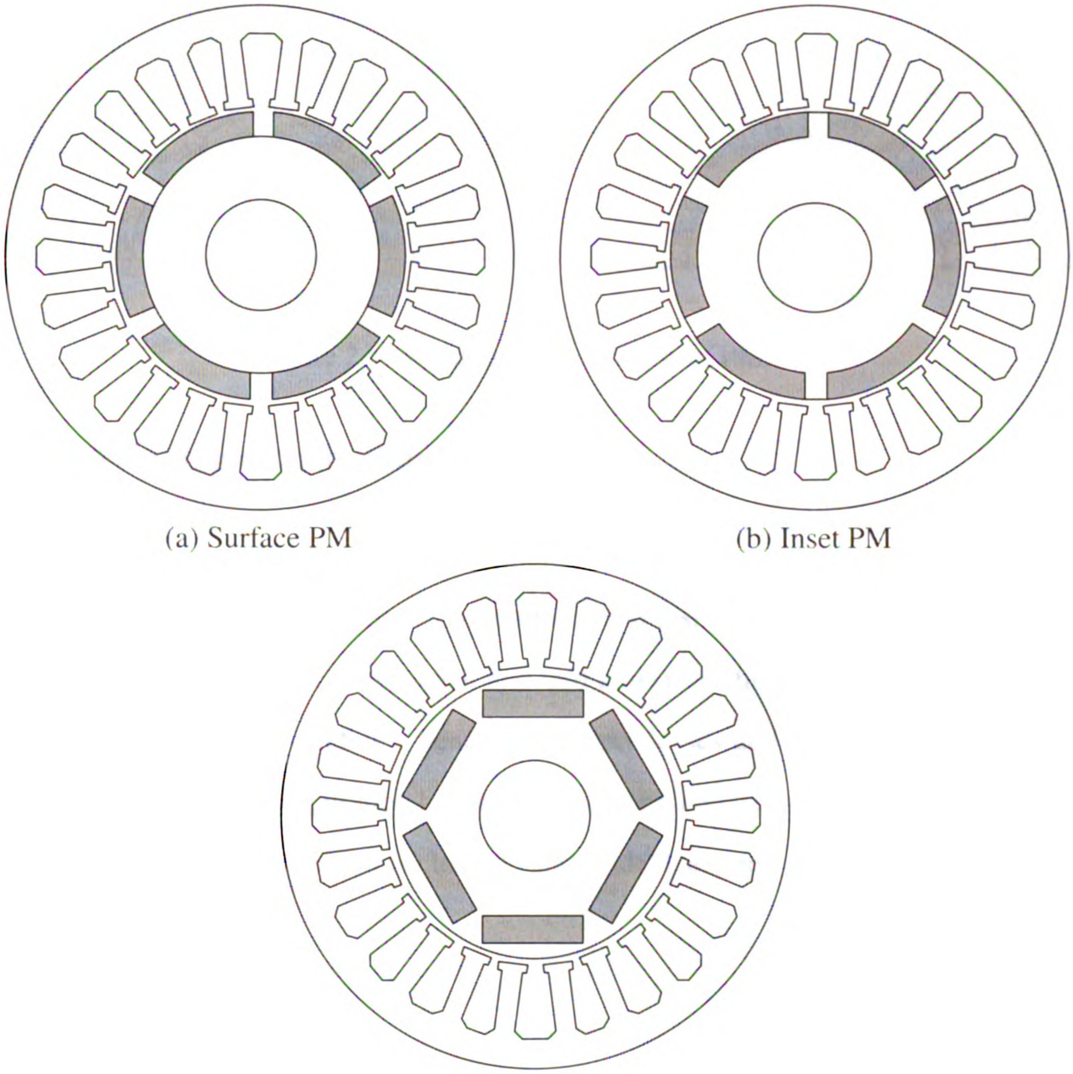

(a) Surface PM (b) Inset PM

(c) Interior PM

Figure 2.4: Permanent magnets location in the interior rotor configuration

The embedded or interior PM rotor has permanent magnets embedded in the deep slots. In IPMSM, the stator synchronous inductance in the q-axis is greater than the synchronous inductance in the d-axis, this saliency produces an additional reluctance torque that makes it suitable for traction applications where high torque and wide speed range is desired.

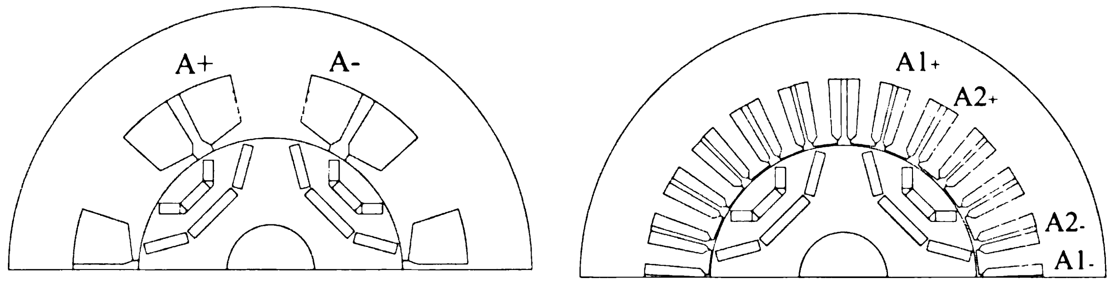

(a) Concentrated (b) Distributed

Figure 2.5: Winding configuration of PMSMs

2.2.2 Winding distribution

The stator windings distribution affects the efficiency and size of the machine. Figure 2.5 shows two basic configurations: concentrated and distributed windings. Concentrated windings are usually designed for small and mid power machines. Their basic advantage is the reduction of end windings, hence the copper losses and leakage flux is reduced. Distributed windings configuration has longer end turns, and has more copper losses, however it provides back emf which is closer to sinusoidal back-emf, and hence this topology reduces iron losses.

2.3 dq Axis Model of PMSMs

The *dq* model of a PMSM can be developed in stator or rotor frame of reference. The model in the rotor frame of reference is preferred because it is simpler. It allows to decouple the flux into magnetization and torque components; the current can be decomposed in the same fashion. The phase diagram of *dq* model of a PMSM is shown in Fig. 2.6. The rotor flux linkages are assumed constant and aligned with the direct axis, while the flux component in the quadrature axis is taken as zero. The core losses are neglected. The stator flux is also represented by two components: direct and quadrature fluxes.

The stator voltage equations in the rotor frame of reference are:

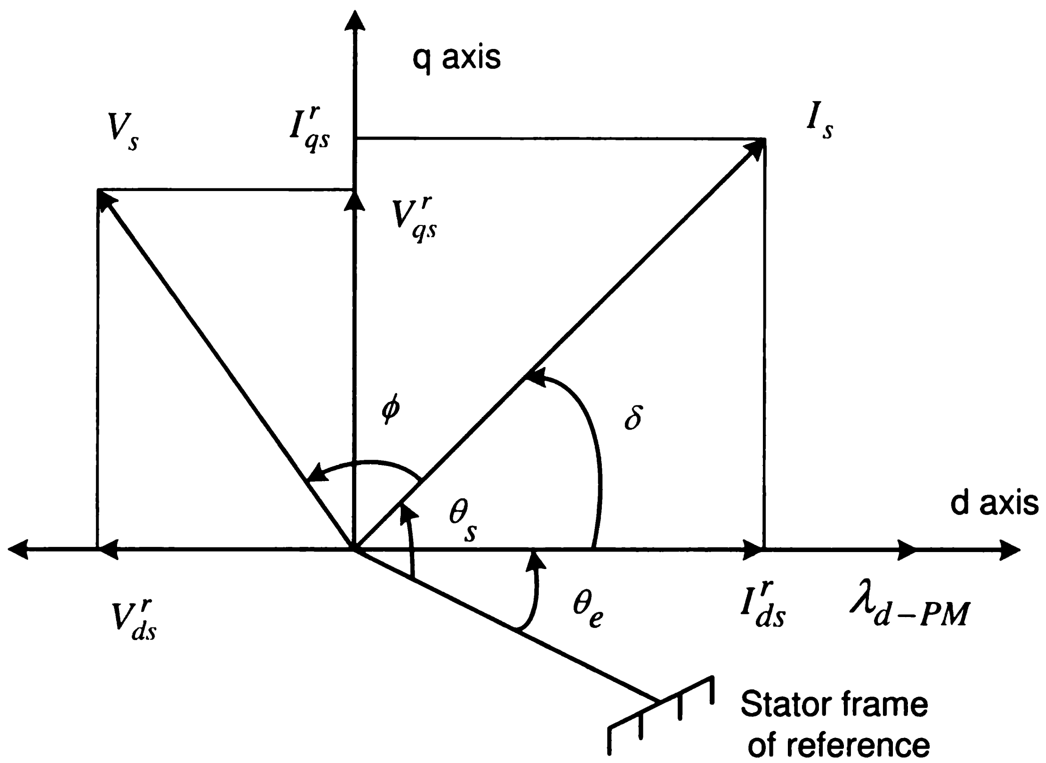

Figure 2.6: Phasor diagram of a PMSM

$$v_d = R_s i_d - \omega_e \lambda_q + \frac{\partial \lambda_d}{\partial t} \tag{2.1}$$

$$v_q = R_s i_q + \omega_e \lambda_d + \frac{\partial \lambda_q}{\partial t} \tag{2.2}$$

where R_s is the stator resistance, v and i are the stator voltage and current and the subscripts d and q refer to the corresponding direct and quadrature axes components. λ is the the stator flux linkages and ω_e is the electrical frequency. The direct and quadrature axis fluxes in the rotor frame of reference are:

$$\lambda_d = \lambda_{d-PM} + L_d i_d \tag{2.3}$$

$$\lambda_q = L_q i_q \tag{2.4}$$

where λ_{d-PM} is the stator flux linkages due to the PM. The inductances L_d and L_q model the stator flux change due to the stator currents. In general these inductances are not equal, because the reluctance of direct and quadrature paths are not the same. In the IPMs shown in Fig. 2.5, the direct axis reluctance is bigger than quadrature axis reluctance, this produces that $L_d < L_q$. The electrical torque τ_e is given by:

$$\tau_e = \frac{3}{2}\frac{P}{2}\left(\lambda_d i_q - \lambda_q i_d\right) \tag{2.5}$$

where P is the number of poles. Substituting (2.3) and (2.4) in (2.5), the torque is calculated as:

$$\tau_e = \frac{3}{2}\frac{P}{2}\left(\lambda_{d-PM} i_q + \left(L_d - L_q\right) i_d i_q\right) \tag{2.6}$$

The first component of the torque, τ_m, is called 'Permanent magnets torque'. It is produced due to the interaction between the rotor flux and the quadrature axis current. The second component, τ_r, is produced due to the relative change of the reluctance of the machine with the rotor position and is called 'Reluctance Torque'.

$$\tau_m = \frac{3}{2}\frac{P}{2}\left(\lambda_{d-PM} i_q\right) \tag{2.7}$$

$$\tau_r = \frac{3}{2}\frac{P}{2}\left(\left(L_d - L_q\right) i_d i_q\right) \tag{2.8}$$

$$\tau_e = \tau_m + \tau_r \tag{2.9}$$

2.4 Modes of Operation of PMSM

PMSMs are usually operated in vector control in dq axis model for efficient machine operation. The operation of the machine is restricted by mechanical and electrical limits that define its torque speed range. The electrical limits of the machine are the maximum current and the maximum voltage. The maximum current is determined by the capability to remove heat from the machine and depends on the design of the cooling system. The maximum voltage is restricted by the peak voltage available from the inverter and the winding insulation grade. The mechanical limits are set by maximum torque and speed handling capacity of the shaft and bearings, and it is defined by the machine design configuration and its electrical limits.

The basic objectives to determine the modes of operation for calculation of torque speed range of PMSMs are to have high dynamic performance and low operational energy losses while operating within voltage and current limits. The operation in the machine is divided basically in two regions; constant torque and constant power [1]. These regions overlap each other at base speed or corner speed.

The operation below base speed is limited by the maximum machine current. The induced voltage is lower than the maximum available from the inverter. In this region, the criterion for efficient machine operation is to use the maximum torque available restricted by the maximum current, named as 'maximum torque per ampere'.

When the machine speed is higher than the base speed, the induced voltage (product of the flux and speed) would exceed its maximum limit. At this point, it is necessary to control the flux in order to operate the machine at the inverter voltage limit. The stator current is controlled in a such way that one component i_d, reduces the direct axis flux and hence the induced voltage. Under this condition the maximum current limit should be satisfied too. The component i_q is chosen in such a way that the current limit is satisfied and the torque produced at this point is maximum but lower than the maximum torque per ampere for the same stator current. This control technique is called 'direct flux weakening control'. Fig. 2.7 shows the block diagram used to control the PMSM for efficient modes of operations.

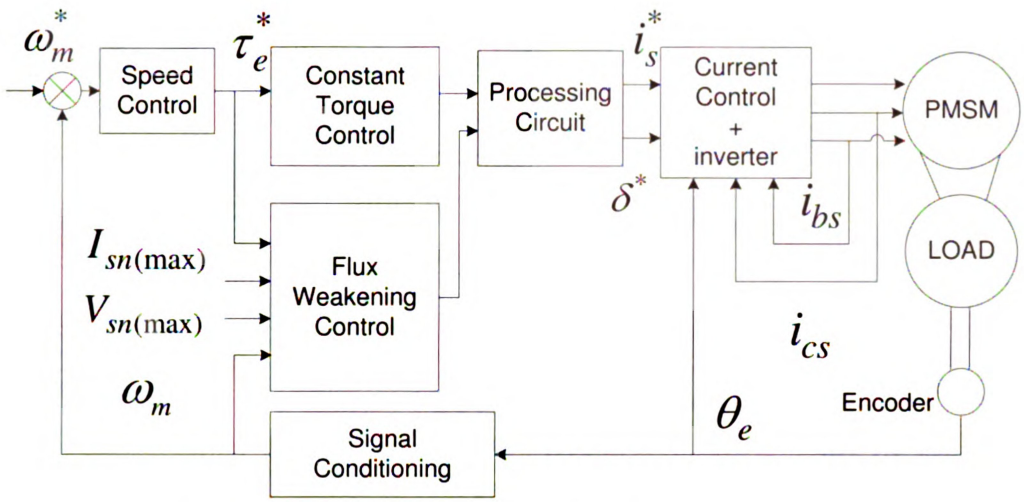

Figure 2.7: Schematic of the PMSM-drive control strategy

2.4.1 Maximum torque per ampere

The Maximum Torque Per Ampere (MTPA) control operates the motor in the region where the induced voltage is lower than the maximum voltage. Then (2.6) is satisfied under the restriction of maximum current and to maximum torque production. Considering the case where the current is equal to the maximum current $I_{\max}$, this current can be decomposed in terms of i_d and i_q as:

$$i_d = I_{\max}\cos(\delta) \qquad \text{and} \qquad i_q = I_{\max}\sin(\delta) \tag{2.10}$$

were δ is the angle between the current space vector and rotor d-axis. Substituting (2.10) in (2.6), the torque is given by:

$$\tau_e = \frac{3}{2}\frac{P}{2}\left(\lambda_{d-PM} I_{\max}\sin(\delta) + (L_d - L_q)\, I_{\max}^2 \sin(2\delta)\right) \tag{2.11}$$

The torque per ampere is given by:

$$\frac{\tau_e}{I} = \frac{3}{2}\frac{P}{2}\left(\lambda_{d-PM}\sin(\delta) + 0.5 * (L_d - L_q)\, I_{\max}\sin(2\delta)\right) \tag{2.12}$$

The angle where the maximum torque occurs is given by:

$$\frac{\partial\left(\frac{T_e}{I}\right)}{\partial\delta} = \frac{\partial}{\partial\delta}\left(\frac{3}{2}\frac{P}{2}\left(\lambda_{d-PM}\sin(\delta) + 0.5 * \left(L_d - L_q\right) I_{\max}\sin(2\delta)\right)\right) = 0 \quad (2.13)$$

solving for δ

$$\delta = \cos^{-1}\left(\frac{-\lambda_{d-PM}+\sqrt{\lambda_{d-PM}^2 + 8I_{\max}^2\left(L_d - L_q\right)^2}}{4\left(L_d - L_q\right)I_{\max}}\right) \quad (2.14)$$

δ lies between 90° and 180° in order to have positive reluctance torque when $L_d < L_q$, which is the usual case in IPMSMs. For an specified value of stator current $I_s = I_{\max}$, the angle is calculated from (2.14) and the current commands are calculated from (2.10).

2.4.2 Direct flux weakening control

Beyond the base speed, the PMSMs operate in direct flux weakening control. At base speed, the machine's terminal voltage reaches its limit and the current space vector angle δ should be increased as the speed increases. The value of δ is selected such that it maximizes the output torque and keeps the motor within the voltage and current limit. It is clear that in this region (2.14) is not longer satisfied. Combining (2.1), (2.2) and neglecting the voltage drop in the resistor the maximum voltage in steady state can be written as:

$$\begin{aligned} V_{\max}^2 &= V_d^2 + V_q^2 \\ &= \left(\omega_e\lambda_q\right)^2 + \left(\omega_e\lambda_d\right)^2 \\ &= \left(\omega_e L_q I_q\right)^2 + \left(\omega_e\left(\lambda_{d-PM}+L_d I_d\right)\right)^2 \end{aligned} \quad (2.15)$$

It is also required to produce the maximum torque available at this point, so the machine operates at its maximum current. The maximum voltage then becomes:

$$V_{\max}^2 = \omega_e^2 \left[L_q^2 \left(I_{\max}^2 - I_d^2 \right) + \left(\lambda_{d-PM} + L_d I_d \right)^2 \right] \tag{2.16}$$

Re-arranging,

$$\begin{aligned} V_{\max} &= \omega_e \sqrt{I_d^2 a + b I_d + \lambda_{d-PM}^2 + c} \\ &\text{where} \\ a &= L_d^2 - L_q^2 \\ b &= 2\lambda_{d-PM} L_d \\ c &= {\lambda_{d-PM}}^2 + L_q^2 I_{\max}^2 \end{aligned} \tag{2.17}$$

For fixed input voltage, speed and stator current, the value of I_d is calculated from equation (2.17), and I_q is calculated by: $I_q = \sqrt{\left(I_{\max}^2 - I_d^2 \right)}$.

Chapter 3

Machine Design, Cross Saturated Modeling and Losses Calculation

3.1 Introduction

High power Permanent Magnets Synchronous Machines (PMSMs) are well known for their high power density and better efficiency. Due to their small volume and high flux density, their iron core saturates deeply and they operate in the the region of magnetic non-linearity, still they have higher efficiency than that of the induction machines for the same output power. The optimized design of high power efficient machines is a vital requirement for energy conservation need of the world.

Most of the analytical design methods of electromagnetic devices work well within the linear region of the BH curve of the iron core. However their accuracy reduces for devices operating in magnetic saturation. The Finite Element Method (FEM) is a very popular tool for the design and analysis of electromagnetic devices. Due to division of iron core into small elements, each element is solved for its electromagnetic problem. In this way, it encompasses very well the non-linearities of the BH curve.

In this chapter, the procedure of the machine design and its performance calculation is discussed, which has been adopted in the following chapters for design and analysis of various PM machines. Since FEM are time consuming, they are usually run for specific current and speed for a machine geometry. An analytical machine model is used to evaluate the machine performance at the desired torque speed range of the machine under different current and voltage. Cross saturated model of PMSMs is an improved analytical method and is it discussed and used here. Calculation of machine parameters were obtained from the post processing of FEM simulations data using cross saturated model and they were used to calculate torque speed curve. A Matlab code was written for processing of the FEM data and calculation of torque speed envelope of the machine.

Calculation procedure of machine losses are also discussed here. Copper losses of the machine are calculated by analytical method by calculating the conductor size and its length. Iron and magnet losses are calculated from the FEM. FEM requires the coefficients of iron losses. Computation of iron losses coefficients form the manufacturer's supplied losses data of the laminations is also discussed here.

Section 3.2 talks about machine design procedure, in which initial analytical design method is discussed in section 3.2.1. The theory of FEM for electrical machines is presented in section 3.2.2.1 and procedure of FEM design iterations is discussed in section 3.2.2.2. Section 3.3 talks about cross saturated model for PMSMs which is used with FEM for design analysis. Calculation of electrical losses is described in section 3.4, in which section 3.4.1, 3.4.2 and 3.4.3 present the calculation of copper, iron and magnet losses respectively.

3.2 Machine Design Procedure

Generally, machine design is an iterative process. Once machine design variables such as geometry, magnets, windings, voltage and current limits are set, its performance indices e.g. inductances, torque, speed, losses, efficiency are evaluated and compared with the desired parameters. The iterations of machine design variables are performed until desired design parameters are met or approached with reasonable accuracy. Initial design is obtained from analytical methods, and most of the FEM iterations are performed after this for the fine tuning and optimization.

3.2.1 Initial analytical design

The main inputs for design of electrical machine are the required output power, current density, maximum flux density, losses and efficiency at various operating points. Current density is usually based upon the machine cooling system. Generally, air cooled PMSMs use current density of less than 10 A/mm^2, whereas water cooled utilize up to 20 A/mm^2. High power density in PMSM dictates the flux density in the iron to be in the range of 2.0 to 2.5 T. An estimate of stator teeth and back iron thickness is provided from the flux of permanent magnets and winding mmf using linear relationship of the magnetic circuit permeances.

Permanent magnets are represented by a flux source in parallel with a permeance. Flux of a permanent magnets is $\phi_r = B_r A_m$ and its parallel permeance is $G_m = \dfrac{B_r A_m}{H_c l_m}$, where H_c and B_r are coercivity and remanent flux density of the permanent magnet. l_m is the length of the magnet in the direction of flux through it, and A_m is its area perpendicular to the flux direction.

Similarly, current carrying stator windings are modeled by time varying magnetomotive force (mmf). The mmf for each stator tooth is calculated from a presumed winding configuration, number of turns and the stator current. With time varying current, the mmf of each stator tooth varies at each time step.

3.2.2 FEM design

3.2.2.1 Governing equations used in the FEM

Transient magnetic application of FEM deals with the time dependent electromagnetic fields, that are related by the following Maxwell's equations:

$$\nabla \times \vec{E} = -\frac{\partial \vec{B}}{\partial t} \tag{3.1}$$

$$\nabla \cdot \vec{B} = 0 \tag{3.2}$$

$$\nabla \times \vec{H} = \vec{J} \tag{3.3}$$

$$\vec{J} = \sigma \vec{E} \tag{3.4}$$

$$\vec{B} = \mu \vec{H} \tag{3.5}$$

where

$\vec{E}$	Electric field (V/m)
$\vec{B}$	Magnetic flux density (T)
$\vec{H}$	Magnetic field intensity (A/m)
$\vec{J}$	Current density (A/m^2)
σ	Conductivity (S)
μ	Permeability (H/m)

and ∇ is vector differential operator. In Cartesian coordinate system, it is defined as:

$$\nabla \equiv \vec{a}_x \frac{\partial()}{\partial x} + \vec{a}_y \frac{\partial()}{\partial y} + \vec{a}_z \frac{\partial()}{\partial z} \tag{3.6}$$

$\vec{a}_x, \vec{a}_y, \vec{a}_z$ are unit vector along their respective axes.

Equation (3.5) refers to magnetic properties of the material. Magnetic flux density and magnetic field intensity can be expressed as functions of each other by the following relationships:

$$\vec{B} = \mu \vec{H} \qquad \Rightarrow \qquad \vec{B} = \mu_0 \mu_r \vec{H} \tag{3.7}$$

or

$$\vec{H} = \nu \vec{B} \qquad \Rightarrow \qquad \vec{H} = \nu_0 \nu_r \vec{B} \tag{3.8}$$

here

μ_0	Vacuum permeability = $4\pi \times 10^{-7}$ H/m
μ_r	Relative permeability
$\nu_0 = 1/\mu_0$	Vacuum reluctivity = $1/(4\pi \times 10^{-7})$ m/H
ν_r	Relative reluctivity

In the presence of permanent magnets, (3.7) and (3.8) becomes

$$\vec{B} = \mu_0 \mu_r \vec{H} + \vec{B_r} \tag{3.9}$$

$$\vec{H} = \nu_0 \nu_r \vec{B} - \vec{H_c} \tag{3.10}$$

whereas

$\vec{B_r}$	Remanent magnet flux density of permanent magnets
$\vec{H_c}$	Coercive magnetic filed of permanent magnets

FEM meshing divides the machine geometry into small elements. Flux 2D (a software tool based on the FEM) is used for all simulations and analysis discussed in this thesis. It uses the magnetic vector potential ($\vec{A}$) for solution of the electromagnetic fields. Equation (3.1) implies presence of electric scalar potential (V) and it is related with $\vec{A}$ by (3.11).

$$\vec{E} = -\frac{\partial \vec{A}}{\partial t} - \nabla V \tag{3.11}$$

Combining (3.3), (3.4), (3.10) and (3.11) results in the following equation:

$$\nabla \times \left(\nu_0 [\nu_r] \nabla \times \vec{A} - \vec{H}_c \right) + [\sigma] \left(\frac{\partial \vec{A}}{\partial t} + \nabla V \right) = 0 \qquad (3.12)$$

where

$[\nu_r]$	Tensor of the relative reluctivity of the medium
$\vec{A}$	Magnetic vector potential (Wb/m)
$[\sigma]$	Tensor of the conductivity of the medium
V	Electric scalar potential

Equation (3.12) is solved by FEM (Flux 2D) in transient magnetic application [2]. Dirichlet boundary condition are applied around the surface of stator in the FEM solution procedure i.e. magnetic vector potential ($\vec{A}$) is fixed at zero. Fig. 3.1 shows a quarter of the geometry of a typical 4 pole IPMSM for reference. Here, for the stator outer diameter, mathematical expression of boundary conditions is $\vec{A}_{MN} = 0$. The subscript 'MN' represents all the nodes lying on the contour line MN. This is a valid consideration because the back iron thickness of the machine is wide enough to keep all the magnetic flux inside the stator core. Furthermore, it is not necessary to model the whole machine for FEM analysis. Instead, a part of machine can be used for FEM which has to be symmetric and repetitive in the full machine geometry. Cyclic boundary conditions are used for even number of poles and anticyclic boundary condition are used when odd number of poles are modeled. During machine rotation of the one pole geometry of Fig. 3.1, the lines LM and LN will always be positioned at any instant of time at an angle θ_1 and θ_2 respectively. Its anticyclic boundary conditions will be $\vec{A}_{LM} = -\vec{A}_{LN}$ and $\frac{\vec{A}_{LM}}{\partial\theta_1} = \frac{\vec{A}_{LN}}{\partial\theta_2}$, where $\vec{A}_{LM}$ and $\vec{A}_{LN}$ are the magnetic vector potential at the nodes of the respective lines.

3.2.2.2 FEM design iterations

The characteristics of high power density electrical machine are non-linear due to deep magnetic saturation. Therefore, it is very hard to obtain a close form solution for an opti-

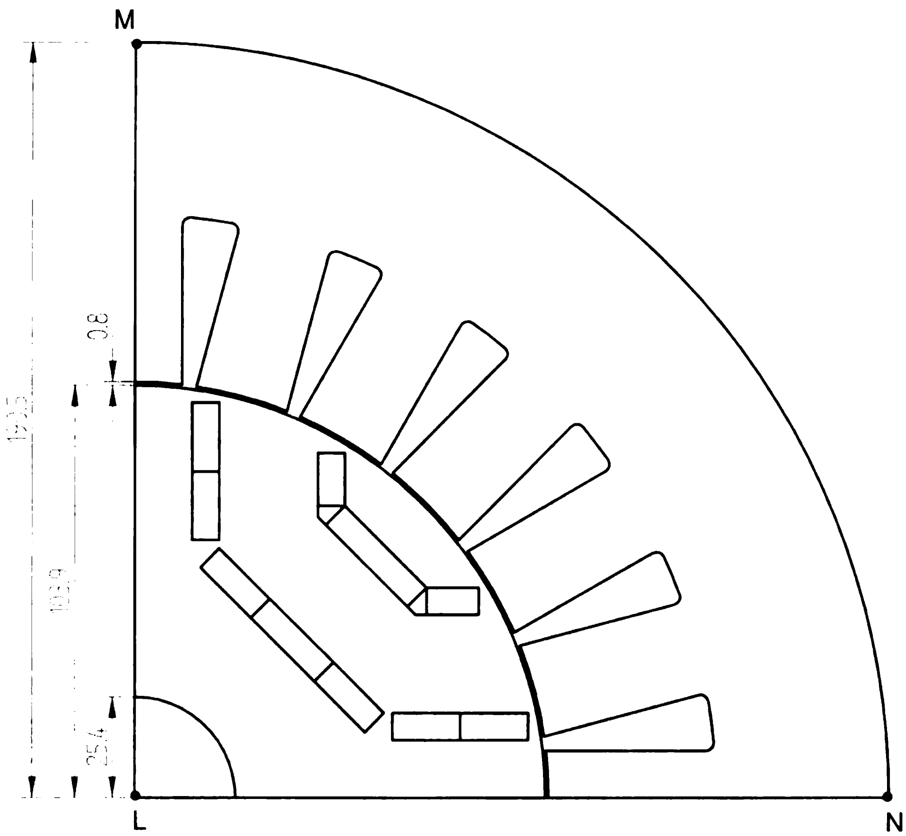

Figure 3.1: Quarter geometry of a 4 pole 105 kW IPMSM

mized design of the machine geometry. The shape of magnets and rotor is more complex and their small variation has significant effect on the machine parameters. Many iterations are usually required to obtain the final machine design and FEM is utilized widely for the iterative design process [3], [4]. In the electrical machine design, the use of FEM always refers to the solution of electromagnetic system of equations in time domain using finite element methods with the applicable boundary conditions, and the same is applicable in this document too.

In the FEM design procedure of electrical machines utilized in this document, machine geometry and the electric circuit of the winding configuration are defined in the FEM software application. Material properties are described and they are assigned to the respective faces of the geometry. Different meshing size is also identified depending the variable concentration of the magnetic flux density. The magnet material, magnetization direction and parameters of the electrical circuit components are defined as well. Time steps of time dependent quantities is also mentioned in transient magnetic solution. The problem is run for a specified time and finally, the results such as voltage, current, inductance, torque, losses etc. are obtained by post processing.

During every iteration, one or more machine design parameters are varied and its effect is noted on the desired output parameter. Parametrization (multiple variation steps) for certain design parameters is also used in some FEM simulations.

Refereing to Fig. 3.1, following are the major concerns of the machine geometry variation and their effect on the design of efficient high power density IPMSM:

(a) Magnet angles and thickness of the bridges (lamination area between the rotor edges and magnets) affects the pulsation in back emf. Wider bridges reduce flux linkage magnets to stator, however, they do not cause much iron losses due to uni-directional deep saturation.

(b) Air gap flux density produced by two magnets layers rotor is closer to the sinusoidal form as compared to the single layer rotor magnets provided inner layer has more flux density than the outer layer.

(c) Deep saturation of the iron core at no load increases the iron losses significantly at lighter loads. Therefore, heavy saturation of the stator teeth and iron is not desirable. If required, air pockets can be added in the magnet layers to reduce magnetic saturation in the iron core.

(d) The thickness of the magnets affects the field weakening range directly. For a given flux linkage and maximum current of machine, thicker magnets reduce the direct axis inductance L_d and hence the field weakening range. On the other hand, thinner magnets can increase the field weakening range but their minimum thickness is restricted by demagnetization limits of the magnets. Decreased no load saturation level reduces flux linkages of magnets and therefore increases the field weakening range.

Once the machine geometry, windings configurations and saturation level of a machine are set for a specific application using FEM iterations, the FEM simulation are performed to extract the machine model. Parametric FEM simulations are setup for stator current (0 to maximum) and its angle (0 to π for motoring and 0 to -π for generating mode of operation). Voltage in each phase was extracted for all combinations of parameters and cross saturated model was used to obtain the machine parameters.

3.3 Cross Saturated Model and Efficient Machine Operation

Cross saturated machine model of a PMSM takes into account the magnetic saturation effect of one axis on the other in dq axes machine model, and it is used to calculate the machine inductances for different load current from the FEM simulated data. Using the same cross saturated model and calculated inductances, torque-speed envelope of the machine was computed for efficient machine operation.

The efficient operating modes of PMSMs [5, 6] are:

(a). Maximum Torque/Ampere (MTPA) mode : Speed up to the corner speed.

(b). Constant power mode : Speed above the corner speed.

The cross saturated model of a PMSM discussed here is applied to the machine geometry given in Fig. 3.1. The key design parameters of this machine are tabulated in Table 3.1.

Equations (3.13) - (3.14) represent the machine model of 3-phase IPMSM in the stator frame of reference [7].

$$v_q = R_s i_q + \omega\lambda_d + \frac{d\lambda_q}{dt} \quad (3.13)$$

$$v_d = R_s i_d - \omega\lambda_q + \frac{d\lambda_d}{dt} \quad (3.14)$$

The flux linkages in both axes are given by (3.15)-(3.16):

$$\lambda_q = \lambda_{q(pm)} + L_q i_q + M_{qd} i_d \quad (3.15)$$

$$\lambda_d = \lambda_{d(pm)} + L_d i_d + M_{dq} i_q \quad (3.16)$$

Table 3.1: Key parameters of 4 pole 105 kW IPMSM

Machine parameter	**Value**
Rated power	105 kW
Rated torque	781.4 Nm
Rated current	140 A
Maximum line voltage	480 V
Corner (base) speed	1285 RPM
Maximum speed	6000 RPM (4.7 pu)
$\lambda_{d(pm)}$	1.03 Wb
Stator phase resistance	0.17 Ω
Air gap	0.8 mm
Rotor diameter	207.8 mm
Stator diameter	381 mm
Stack length	240 mm
Stator slots	24
Winding type	double layer (Lap)
Slots/pole/phase	2
Number of turns	11 per coil
Magnet grade	NdFeB N35SH
Stator and rotor core	M-19 G24 silicon steel

The output torque of the machine is given by (3.17).

$$T = \frac{3}{2}\frac{P}{2}\{\lambda_{d(pm)}i_q - \lambda_{q(pm)}i_d + (L_d - L_q)i_q i_d - M_{qd}i_d^2 + M_{dq}i_q^2\} \qquad (3.17)$$

Equations (3.15)–(3.17) model the cross saturation of the IPMSM, in which the current of one axis affects the flux linkages of the other through saturation. This coupling depends on the machine geometry and the saturation level. The model indicates that the permanent magnets affect the flux linkages in both d and q axes. Here, L_d and L_q are self inductances, and M_{qd} and M_{dq} are quasi- mutual inductances [8]. It must be noted that $M_{qd} \neq M_{dq}$, since these parameters do not represent the actual mutual inductances.

The conventional dq model of IPMSM that assumes that current and flux linkages in d and q axes are independent of each other can be obtained by setting $\lambda_{q(pm)}$, M_{dq} and M_{qd} equal to zero in (3.15)–(3.17).

The torque speed curve was calculated by the inversion of (3.13)–(3.17) in 'steady state'. The torque was computed by maximum torque per ampere up to corner speed for rated current. At this current the current angle δ was varied between 90°–180° and equations (3.13), (3.14) and (3.17) were solved. The value δ_0, corresponding to maximum torque was determined. Above corner speed, when both the current and voltage $v_s = \sqrt{v_d^2 + v_q^2}$ are at their maximum values, the current angle was increased in steps, up to 180°, giving i_d, i_q. From these values and v_s, (3.13) and (3.14) were solved for ω and corresponding T was calculated from (3.17). This allowed the determination of the pairs of ω and T, for torque speed envelope of the machine as shown in Fig. 3.2.

Although the machine model with cross saturation is relatively complex, it provides more accurate results than the conventional dq model. Fig. 3.3 [8] depicts the torque calculated for both models at rated current for angle $90^\circ - 180^\circ$.

Fig. 3.3 shows that the torque calculated using the cross saturated dq model agrees well with that of the torque obtained from the FEM, while the torque calculated by the simple

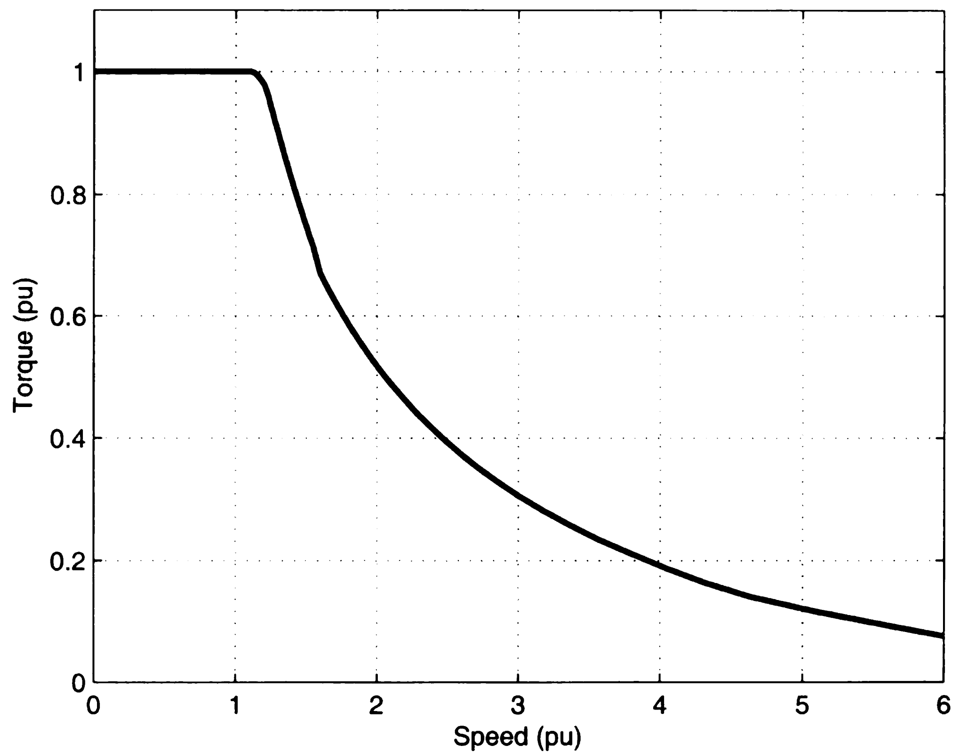

Figure 3.2: Operating range of the IPMSM calculated using cross saturated dq model.

dq model has an error of about 8%. Current angle for maximum torque was 136.5° using cross saturated dq model and 132° when calculated from the simple dq model.

3.4 Calculation of Machine Losses

This section describes the calculation of electrical losses of IPMSM and they consist of copper, iron and magnet losses. Copper losses are calculated analytically. Iron and magnet losses are computed by the FEM.

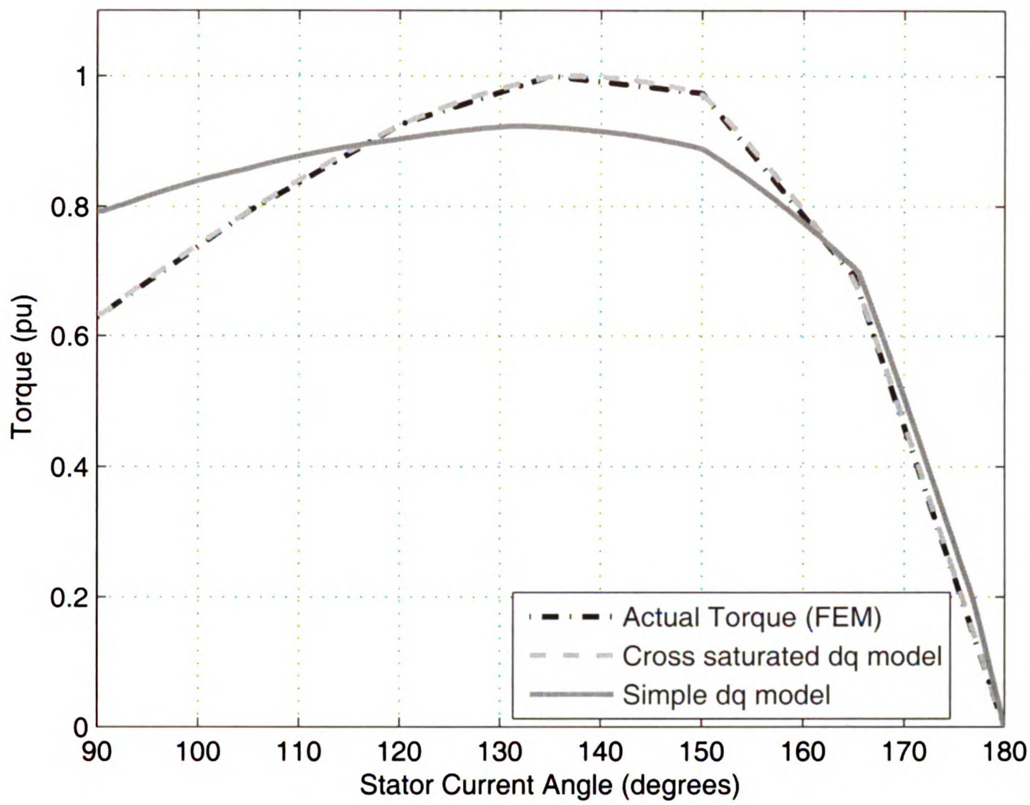

Figure 3.3: Comparison of developed torque for machine models with and without cross saturation.

3.4.1 End windings and copper losses

End windings may be a significant portion of the windings conductors, which do not contribute towards torque/EMF of the machine. Long end turn windings cause more winding resistance and therefore losses. Each side of the winding conductor is placed in a stator slot. For distributed windings, the end windings length of a conductor in the coil can be approximated by average length of the arc and semicircle of the winding slots. Fig. 3.4 shows the equivalent configuration of placement of two conductors in stator slots to calculate the end winding length. where

R = Average distance from coil center in its slot to the center of rotor (m)

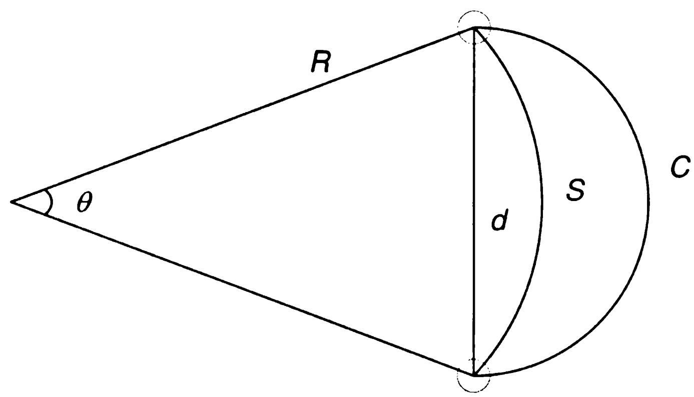

Figure 3.4: End winding representation of the distributed winding

θ = Angle (rad) between two sides of coil with origin as rotor center (rad)

S = $R\theta$ = Average arc length of each coil on the stator slot (m)

d = Direct distance between two coil centers, which have arc length S (m)

C = $\pi d/2$ = Half circumference of circle having the coil centers on its boundary (m)

E = Coil extended length from stator stack before end turning (m)

Coil extended length is part of coil conductors that remains straight at the end of stack length before bending. Its length varies 1 cm to 7 cm depending upon the size of winding conductors and number of turns in a coil. In a practical machine windings of 30 turns/coils of AWG 9 or equivalent conductors, extended length of 2.5 cm is reasonable. Then

End turn length of each coil = $l_{end} = 2E + \frac{1}{2}(S + C)$

Length of each coil = $l_c = 2N_c(l_{end} + l_{stack})$

The resistance of coil is:

$$R_c = \frac{l_c}{\sigma A_c} \tag{3.18}$$

where

σ Conductivity of coil material (S/m)

A_c Cross sectional area of coil conductor (m^2)

N_c Number of turns in the coil

Phase resistance (R_{ph}) was calculated from coil resistance (3.18) and series/parallel connection of the coils in the winding. Copper losses of the machine are:

$$P_c = 3I_{ph}^2 R_{ph} \tag{3.19}$$

The change in the resistance of a conductor with temperature is characterized by its linear increase with temperature and is given by (3.20).

$$R = R_0(1 + \alpha(T - T_0)) \tag{3.20}$$

where

R = Resistance at required temperature T, (Ω)

R_0 = Known resistance at temperature T_0, (Ω)

α = Thermal coefficient of conductor ($^{\circ}C^{-1}$)

T = Temperature at which conductor resistance to be calculated ($^{\circ}C$)

T_0 = Known temperature at which, resistance of conductor is known ($^{\circ}C$)

Efficiency analysis of machines may be desired at elevated temperature. The copper losses are temperature dependent, and are computed accordingly at the machine's operating temperature using (3.20).

3.4.2 Iron losses

Machine rotation and alternating current cause the continuous change in the magnetic flux in the stator and rotor laminations. Iron losses develop in the magnetizing material due to flux variation and induction of eddy currents. FEM are widely used in the machine design for iron losses calculation and provide more accurate results than those obtained by the analytical methods. However, the coefficients of iron losses are required in post processing of FEM simulations. This section describes the calculation procedure of iron losses coefficients from the losses data provided by the manufacturer of the laminations.

In FEM transient magnetic application, iron losses per unit volume for each element of iron core at one time instant 'P_l' and over one cycle of electrical frequency 'W_l' are given by (3.21) and (3.22) respectively [2].

$$P_l = k_h B_m^2 k_f f + \pi^2 \frac{\sigma d^2}{6} B_m^2 f^2 k_f + 8.67 k_e B_m^{1.5} f^{1.5} k_f \tag{3.21}$$

$$W_l = \frac{1}{T}\int_0^T P_l \, dt = k_h B_m^2 f k_f + \frac{1}{T}\int_0^T \left[\sigma \frac{d^2}{6}\left(\frac{dB(t)}{dt}\right)^2 + k_e \left(\frac{dB(t)}{dt}\right)^{1.5}\right] k_f dt \tag{3.22}$$

where

k_h = Coefficient of hysteresis losses ($W/T^2 s^{-1} m^3$)

k_e = Coefficient of excess losses ($W/(T s^{-1})^{3/2} m^3$)

σ = Conductivity of laminations $(\Omega m)^{-1}$

d = Thickness of laminations (m)

k_f = Fill factor of laminations (0–1)

f = Frequency of stator current (Hz)

B_m = Maximum flux density (T)

The three components of losses in (3.21) and (3.22), are hysteresis, eddy current and excess losses. Here, f is known for the stator and it is zero for the rotor because it rotates at synchronous speed. B was calculated by FEM solution, σ and d were readily available from the manufacturer's information of laminations, and k_f was calculated from lamination thickness and stack length of the machine using (3.23).

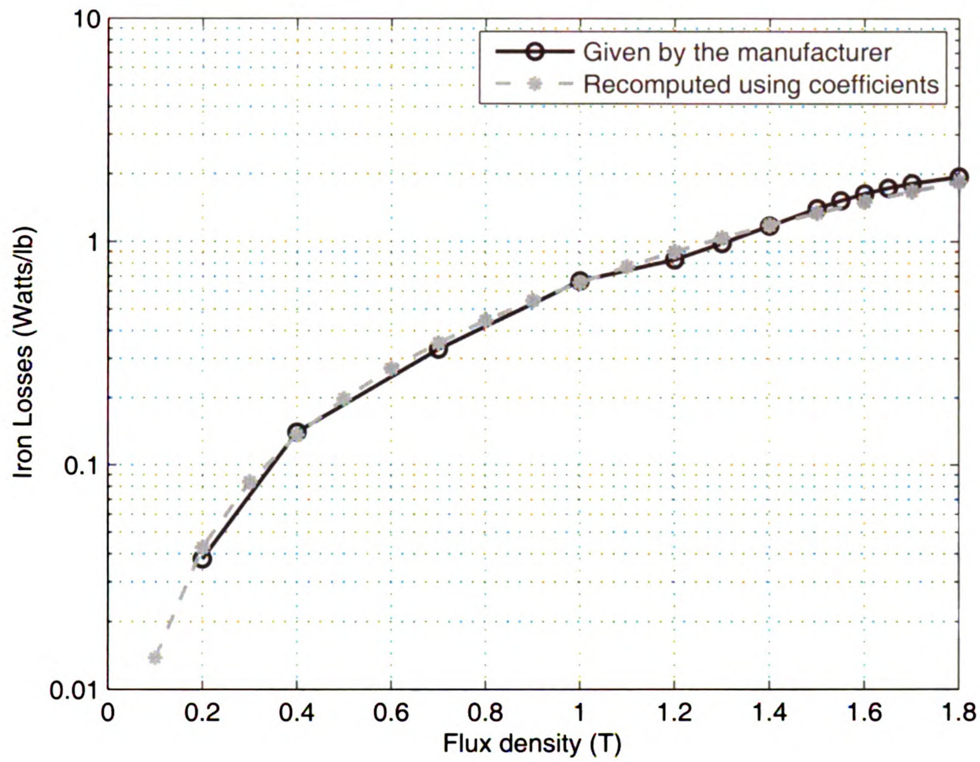

Figure 3.5: Iron loss; provided by manufacturer and computed using iron losses coefficients

$$k_f = \frac{No.\ of\ laminations\ \times\ Lamination\ thicness}{Stack\ length\ of\ stator/rotor} \tag{3.23}$$

Generally, losses information is available in iron losses/unit weight (W/Kg or W/lb) versus flux density at a fixed frequency. The iron losses coefficients (K_h and K_e) were computed from the loss data of the laminations steel at two points on the losses curve provided by the manufacturer. Since the loss curve is higher order polynomial, fine tuning of K_h and K_e is required in order to closely match the given losses. Fig. 3.5 shows the original losses curve and as it is re-computed using the calculated coefficients.

Once the coefficients (K_h and K_e) are known, iron losses of the machine are calculated by FEM post processing for the FEM simulated test.

3.4.3 Magnet losses

The losses in the permanent magnet develop due to induced eddy currents and they were calculated using FEM. The magnets were defined as solid conductor with their electrical conductivity in the electrical circuit of the FEM simulations. A resistor is connected across each solid conductor to simulate the effect of closed eddy currents in the magnets. Fig. 3.6 shows the electric circuit of one pole of IPMSM shown in Fig. 3.1 In the FEM post processing, 'active power' appearing in the magnets represents the magnets losses.

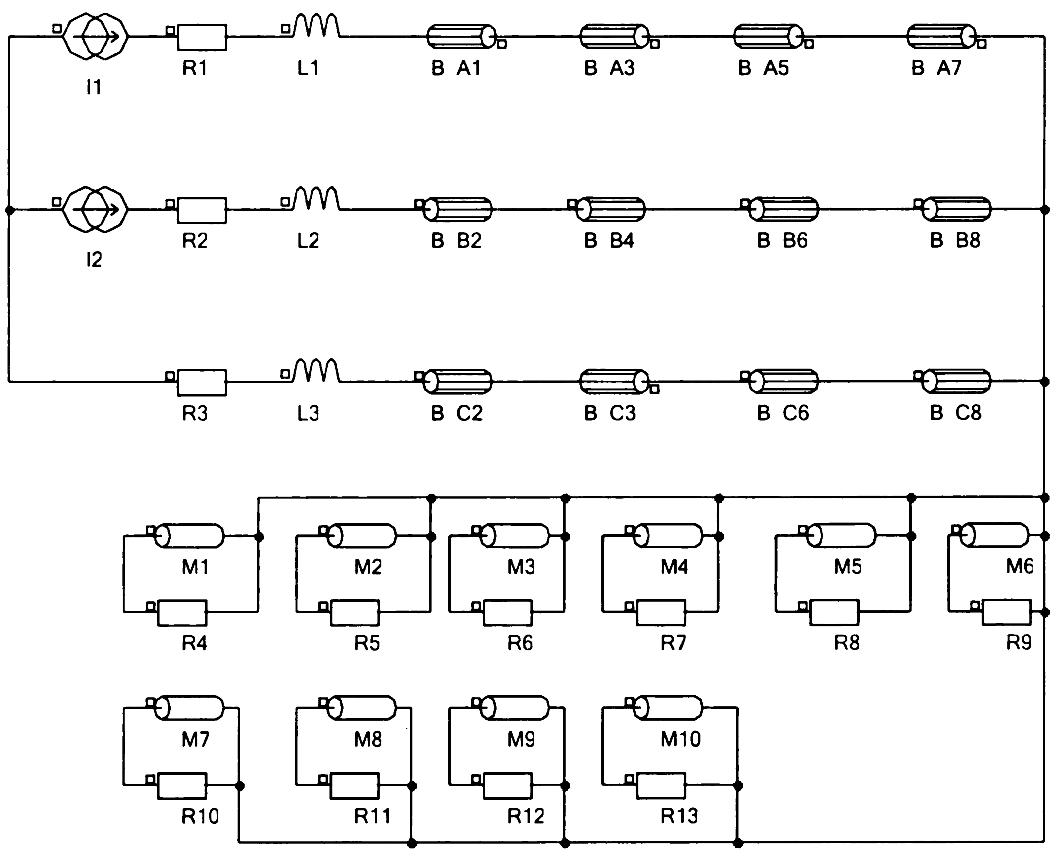

Figure 3.6: FEM equivalent lumped electric circuit of one pole of an IPMSM

Chapter 4

Design and Evaluation of Traction Machine for Hybrid Vehicles Based upon a Given Driving Cycle

4.1 Introduction

Permanent Magnet Synchronous Machines (PMSMs) are widely used as traction machines in the Hybrid and Electrical Vehicles (HEVs) due to their high power density, wide field weakening range and high efficiency. Designing an electrical machine to match its application is vital for efficient operation of an HEV. An optimized machine is usually the outcome of many design iterations. Efficiency maps are generated for every design iteration to evaluate the performance of the machine and vehicle.

The conventional design approach of a PMSM machine is generally based upon the maximization of machine efficiency at its maximum output power near corner speed and in the field weakening region. PMSMs can also be designed with high efficiency contours positioned at any desired place within the torque speed curve of the machine operation. In a practical application, HEVs follow a driving cycle that is a set of data points representing speed versus time of the vehicle as shown in Fig 4.1 for Federal Test Procedure (FTP) driving cycle of an urban bus. Torque speed requirements of a traction machine are calculated using vehicle parameters and the driving cycle. Machine designed for continuous maximum power or speed in a driving cycle is an overkill for an HEV application, because driving conditions do not demand for it.

Average (overall) Driving Cycle Efficiency (ADCE) of a traction machine is the ratio of its output to input energy for a driving cycle of the vehicle. ADCE of traction machine is more important parameter than its maximum efficiency at one operating point. A traction machine having less efficiency at one operating point can have more ADCE than the other machine and vice versa.

A traction drive of an HEV consists of electrical machine, inverter and their cooling

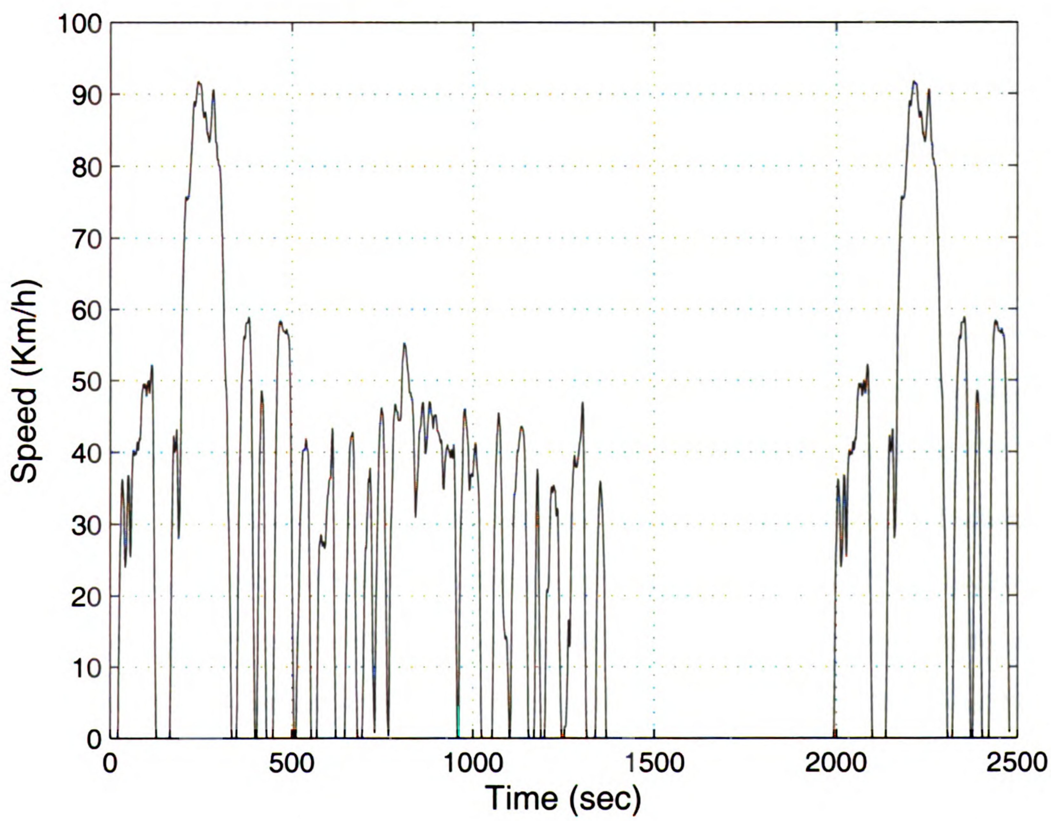

Figure 4.1: FTP driving cycle; speed vs time

system. Most of the traction machines and inverters employ closed liquid (water/oil) cooling, and utilize significant additional energy. Therefore, it makes more sense to include the efficiency of the inverter and cooling system with that of the machine in the calculation of ADCE for evaluation of the traction drive designed for a specific application.

In this chapter, a design evaluation procedure for electrical machines for HEVs is presented by calculating its ADCE. The method is applied two different machine designs. Section 4.2 presents the literature review and design evaluation approach is given in sectio 4.3. Calculation of torque speed requirements and energy density for a specific bus and a driving cycle is described in section 4.4.

4.2 Literature Review

Design and efficiency analysis of the HEVs has been presented by several researchers based upon different aspects. Williamson *et al.* have analyzed overall drive train efficiency based upon efficiency maps and driving cycles, and proposed supervisory control for efficient vehicle operation [9]. Rahman *et al.* have proposed high ADCE or 'energy efficiency' of EV and HEV propulsion system using a traction machine design such that frequent operating points of the driving cycle lie under constant power region, and machine has maximum efficiency there [10]. It is possible but not necessary that frequent operating points and maximum energy density area of a driving cycle lie at the same place.

Schofield *et al.* compared the designs (in terms of machine volume) of PM brushless DC and PMAC machines, and presented their thermal analysis for an EV application in [11, 12]. Two machine designs were proposed in [11] for a specific gear ratio: one for continuous operation at maximum speed, and another for a specific driving cycle. It was shown that the traction machine operating continuously at maximum speed of the vehicle requires larger volume and runs at higher temperature than the machine designed and operated for a driving cycle. In fact, the machine will never operate in continuous mode during its life cycle for HEV application.

The size optimization of power components (battery and ultra capacitor) is discussed based upon driving cycle for a fuel cell HEV in [13], where traction motor is sized for maximum vehicle power demand. Similarly, a method of optimizing the size of engine, traction drive and batteries is presented for different urban driving cycles [14]. Gao *et al.* presented efficiency analysis of a series hybrid bus based upon the different topologies of supervisory control [15].

4.3 Machine Design and Evaluation Approach

High ADCE of a HEV requires efficient design of traction drive for a specific driving cycle. Often, volume and temperature limits are also set as design constraints for the traction machines for HEVs. Electrical machines discussed here are designed taking into consideration the space and operational constraints on a bus of the Mass Transportation Authority (MTA) in Flint, Michigan.

In this chapter, a new approach is proposed to maximize the ADCE of the traction drive. It encompasses the design, thermal analysis and evaluation of an interior PMSM. The design was tuned in terms of geometry, windings and magnet materials as mentioned in section 3.2.2.2. The design objective was to place contours of maximum efficiency around the high energy density area of the FTP driving cycle of Fig. 4.1 for the series hybrid bus. The designed IPMSM based upon the proposed method was compared with a design that was obtained by not following this approach. Performance of both machines was evaluated for ADCE for the following identical design parameters:

1. Coverage of more than 99% torque speed points of the driving cycle requirements.
2. Machine volume and size of cooling jacket.
3. Maximum hot spot temperature.
4. Rated voltage and current of the inverter and dc link voltage.

The traction drive consists of traction machine, inverter and cooling system. The effect of electrical machine on the ADCE is more dominant than that of the inverter and cooling system due to its relatively wide efficiency range. Therefore, the inverter and cooling system are the same for the both machines discussed here. However, their energy consumption will be different, and it is included in the design evaluation of the both machines. In order to include the effect of variable dc link voltage on machine losses, a PWM model of inverter can be explored further.

4.4 Driving Cycle and Energy Density

A driving cycle of a vehicle is represented by its road speed versus time. Driving cycles are generated by different countries and organizations to assess the performance of vehicles in various ways such as fuel consumption, polluting emissions and acceleration time of the vehicle. An FTP driving cycle shown in Fig. 4.1 is used here as design input. Design specification of traction machine requires driving cycle information expressed in terms of torque versus speed points. The following parameters of a bus of the MTA Flint are used to calculate the torque-speed requirements for the design of traction machines.

1. Bus weight including passengers = m_{bus} =16,500 Kg
2. Front area of bus = A_f = 9.47 m^2
3. Tire radius = R_{tyre} =0.45 m
4. Machine shaft to wheel axle gear ratio = G_r = 8.24

The torque and speed of the traction machine can be calculated as:

$$T_m = \frac{F_{bus} \times R_{tyre}}{G_r} \tag{4.1}$$

where T_m is required torque of the motor and F_{bus} is traction force of the bus to travel at the desired speed of the driving cycle.

$$F_{bus} = F_{rolling} + F_{ascend} + F_{aerodynamic} + F_{accelration} \tag{4.2}$$

where the components forces are:

$$F_{rolling} = m_{bus} \times g \times \cos(\arctan(grade)) \tag{4.3}$$

$$F_{ascend} = m_{bus} \times g \times \sin(\arctan(grade)) \tag{4.4}$$

$$F_{aerodynamic} = 0.5 \times air\ density \times A_f \times drag\ coefficient \times bus\ speed^2 \tag{4.5}$$

$$F_{acceleration} = m_{bus} \times \frac{(driving\ cycle\ speed - bus\ speed)}{time\ step} \tag{4.6}$$

The rotational speed of the motor is:

$$Motor\ speed\ (rad/sec) = \frac{(driving\ cycle\ speed + bus\ speed)}{2} \times \frac{G_r}{R_{tyre}} \tag{4.7}$$

Fig. 4.2 represents the operating points of FTP driving cycle in terms of torque and speed requirements for one traction drive, which is calculated using a commercial software Advisor [16]. Two identical traction machines running at same speed and connected through a summation gear box, will drive the bus each sharing half of the torque required by the bus. In order to achieve the required performance of the FTP driving cycle by the vehicle, the torque speed envelope of the each traction machine should cover most of the the operation points.

Each operating point of the driving cycle is shown by a "*" in Fig. 4.2, and it represents the operation of the traction drive for one second. The density of these points represents the operational time density of the traction machine in its torque-speed envelope. However, the power at each operational point varies. Thus, the energy density of the driving cycle is

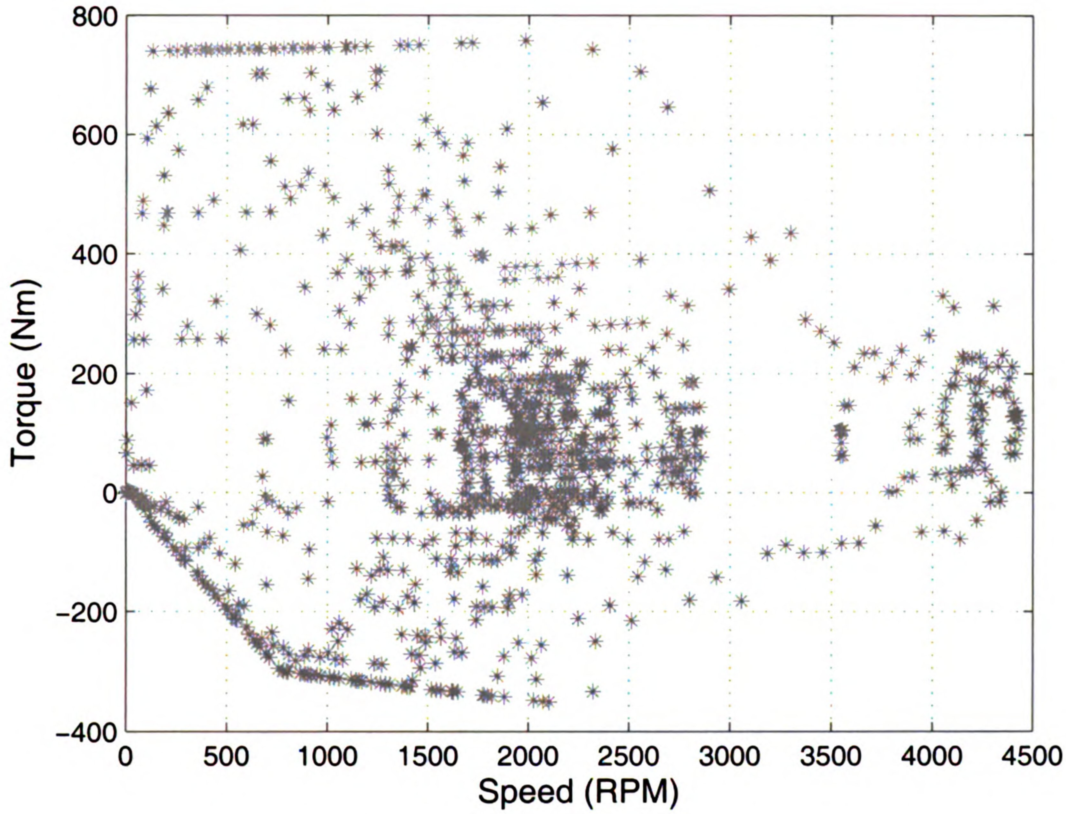

Figure 4.2: Torque speed command points of an FTP driving cycle at the machine shaft

different from its operational time density. A mesh on the torque speed map was generated for Fig. 4.2, and the energy required to drive the bus was calculated for each mesh unit. Fig. 4.3 shows the contours of equal energy superimposed on the torque speed points of FTP driving cycle to drive the bus. In order to maximize ADCE, the efficiency map of a traction machine should have contours of high efficiency close to the region of high energy density of Fig. 4.3.

4.5 Machine Design

Two different machines were designed and analyzed for the application of proposed approach as shown in Fig. 4.4 and their key parameters are given Table 4.1. Both machines

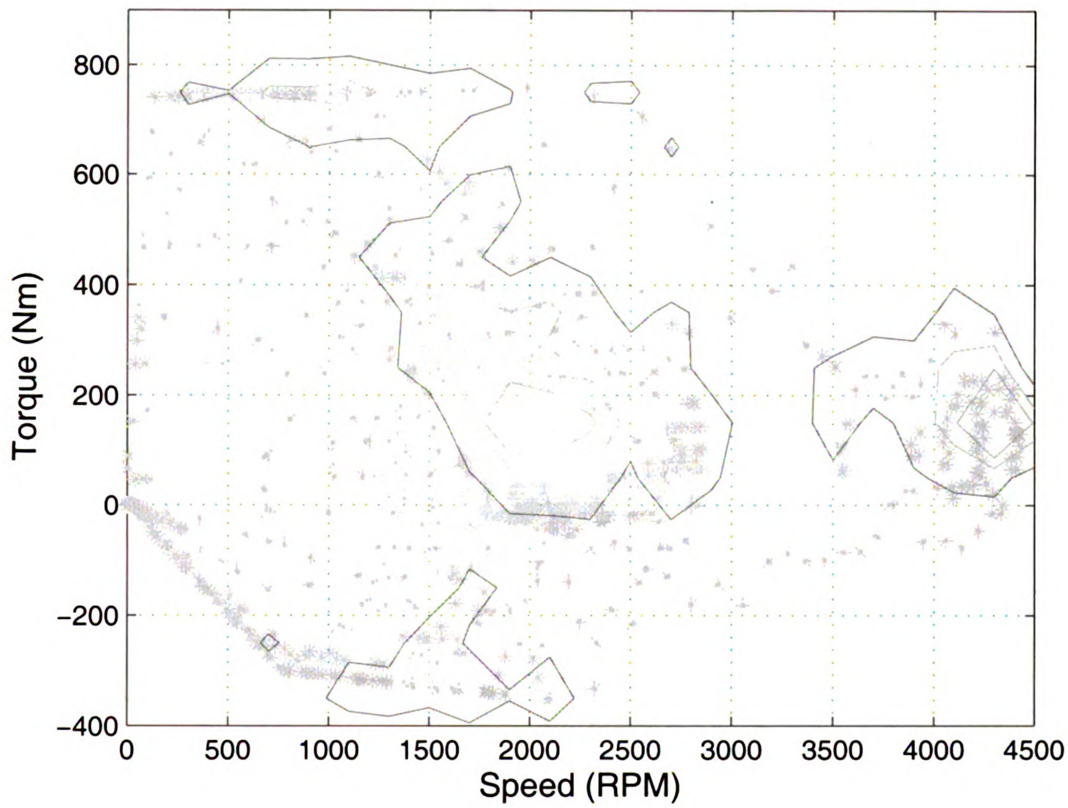

Figure 4.3: Torque speed points of an FTP driving cycle and the energy density contours

were targeted to cover the 99% of the operating points of the driving cycles. Stator of both machines is same and rotors are different. Design iterations by FEM were carried to minimize machine losses. Torque speed curve of both machines were calculated from post processing of the FEM simulation data in Matlab using cross saturated machine model for efficient machine operation as discussed in section 3.3, Both machines have the same maximum voltage, however, their maximum current is different as shown in Table 4.1. Maximum torque per ampere operating strategy was used up to corner speed, and voltage and current limits were used for higher speed [17]. The torque speed curves of both machines in motoring mode, superimposed on the operating points of the driving cycle are given in Fig 4.5.

Analysis shows that input current of machine M1 is more than that of the machine M2

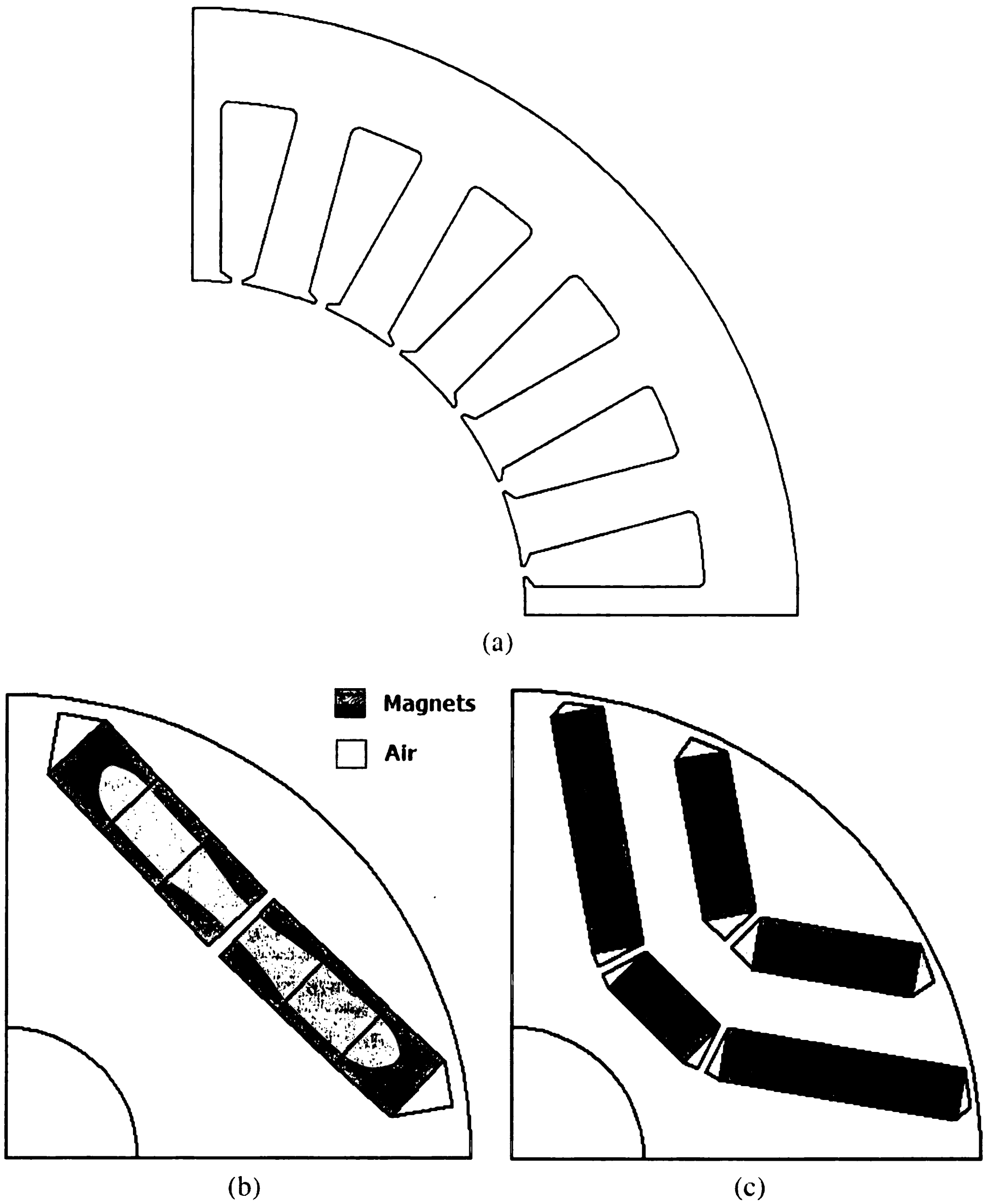

Figure 4.4: Quarter geometry of two traction machines designed for FTP driving cycle: (a) Stator; (b) Rotor of machine M1 ; (c) Rotor of machine M2 .

for same maximum output torque. Similarly, field weakening range of both machines is also different. However, both machines were capable to cover the 99% of the operating points of the driving cycle. Machines are further compared for their efficiency map as well as ADCE of the traction drive in the next two sections.

4.6 Losses and Efficiency Map Calculation

To generate the efficiency map, power losses were computed under the torque speed curve of the both machines. Both axes of the torque speed curve were divided into small steps and the area under this curve was meshed. The machine current and its angle was calculated on the mesh intersection points for efficient machine operation using cross saturated machine

Table 4.1: Key parameters used for two IPMSMs designed for an FTP driving cycle

Machine parameter	**Value**
Rated power	140 kW
Rated torque	760 Nm
Maximum line voltage	480 V
Rated current M1	198 A
Rated current M2	180 A
Corner (base) speed	1760 RPM
Maximum speed M1	7000 RPM (4.00 pu)
Maximum speed M2	5000 RPM (2.84 pu)
Air gap	1.0 mm
Rotor diameter	90.0 mm
Stator diameter	165.1 mm
Stack length	200 mm
Stator slots	24
Winding type	double layer (Lap)
Slots/pole/phase	2
Number of turns	6.5 per coil
Magnet grade	NdFeB N35SH
Stator and rotor core	M29 G15 C5 silicon steel

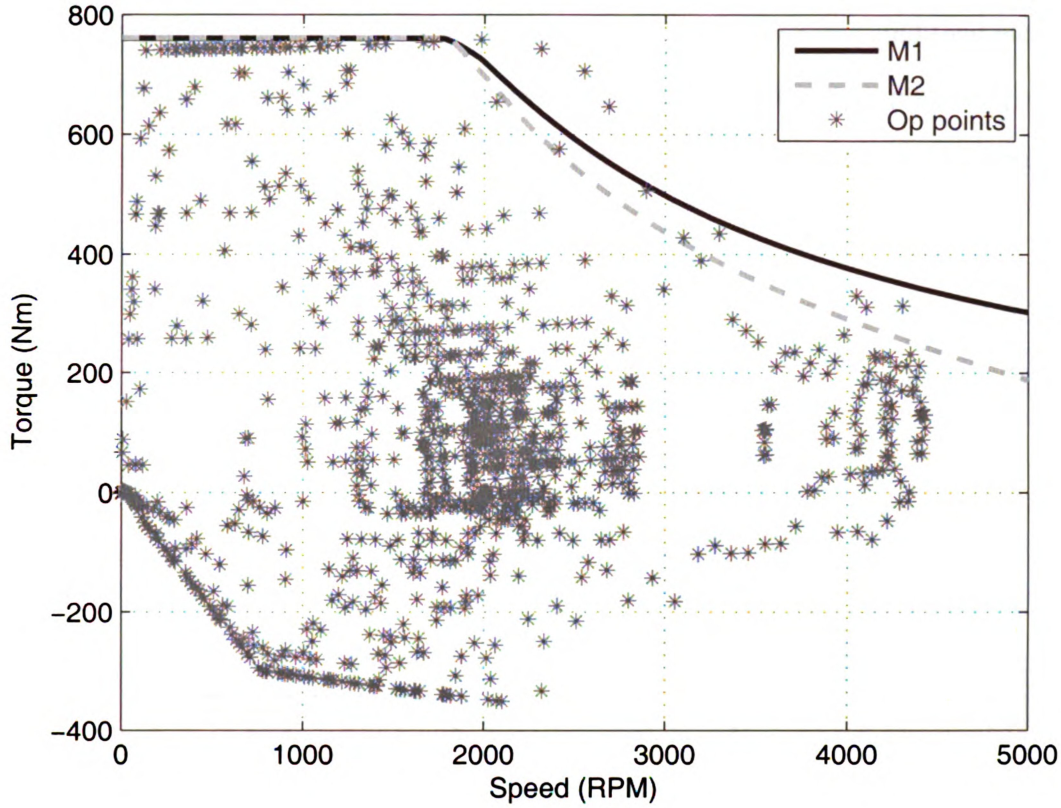

Figure 4.5: Torque speed curves of two IPMSMs designed for FTP driving cycle

model as discussed in section 3.3. FEM simulations were used to calculate iron and magnet losses for each mesh point for the computed current.

4.6.1 Machine losses

Machine losses were computed using the calculated current and respective FEM simulations on these mesh points of the operating region of the machines. Copper losses of the machines were calculated analytically from conductor gauge, length and current passing through them as discussed in section 3.4.1. Iron losses were calculated from the post processing data of the FEM simulations of each mesh point. Iron losses coefficients required by the FEM were calculated from the loss data of the iron laminations as mentioned in section 3.4.2. Similarly, magnet losses were calculated from FEM as outlined in section 3.4.3. Copper, iron and magnet losses were summed up at each mesh point to find total electrical losses of the machine. Machine efficiency was calculated from output power (P_0) and losses from (4.8), and efficiency map of the both machines were generated and are given in Fig. 4.6 and 4.7.

$$Efficiency = \frac{P_0}{P_0 + losses} \tag{4.8}$$

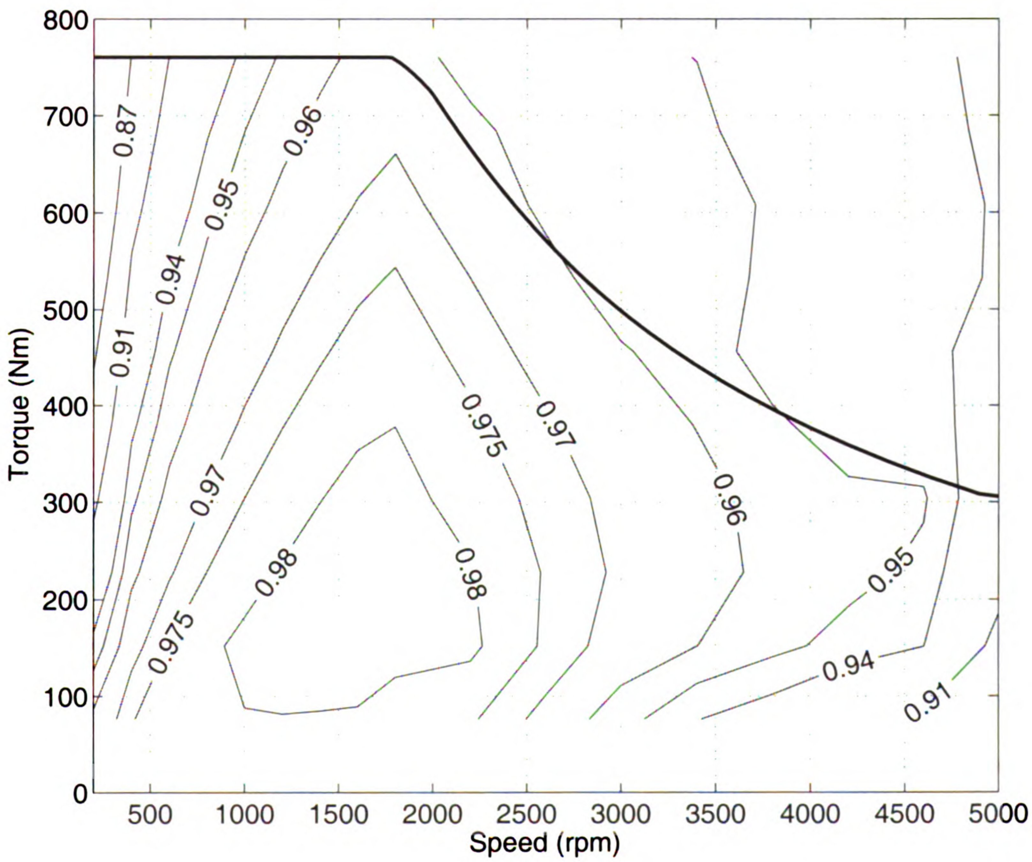

Figure 4.6: Efficiency map of machine M1

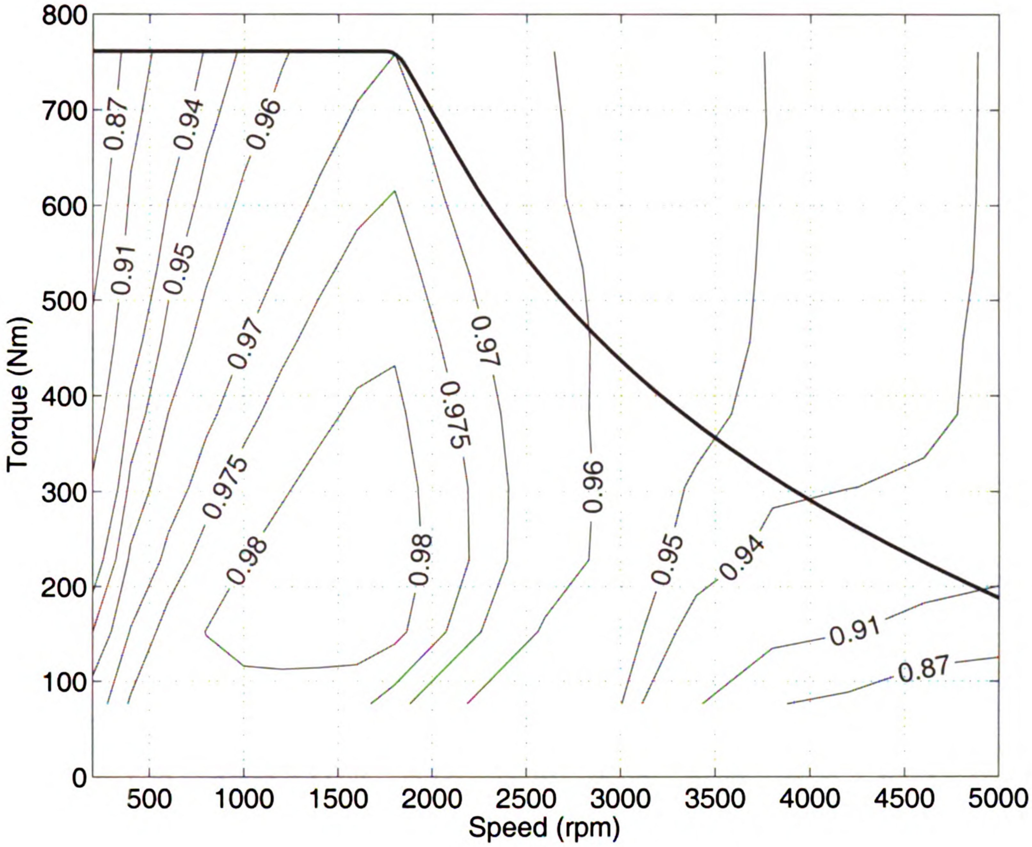

Figure 4.7: Efficiency map of machine M2

4.6.2 Inverter losses

Inverter losses were computed for every mesh point using an online software SemiSel (Semikron Semiconductor Selection) [18]. This software provides interactive calculation of power dissipation and temperatures for inverters and power semiconductors. The input parameters such as voltage, current, power factor, switching frequency were provided as input for each mesh point to the software, the corresponding losses of the inverter were obtained as output. Combining the inverter losses with machine losses at all mesh points of the operating region, the efficiency map of the each motor including its inverter was calculated, and is given in Fig. 4.8 and 4.9.

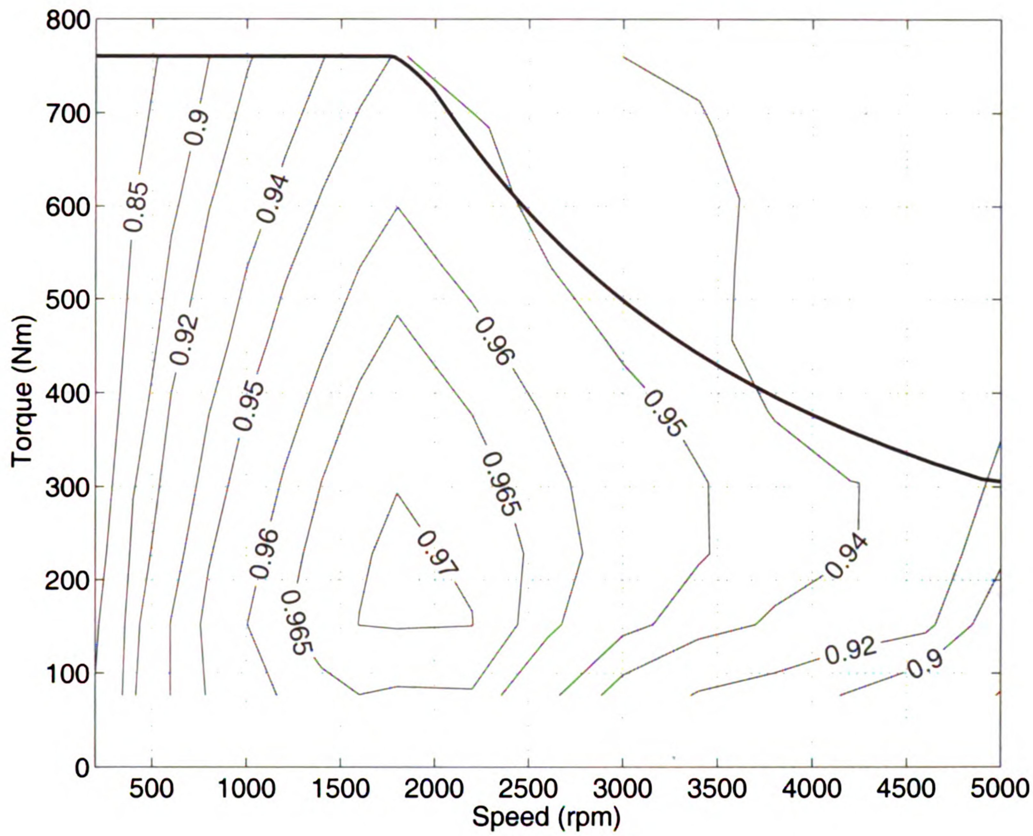

Figure 4.8: Efficiency map of machine M1 including inverter

4.6.3 Cooling power

Owing to the high power density, both machines were designed to be cooled by stator water jacket. Similarly, inverters are also water cooled. To keep the same maximum operating temperature of each drive (machine and inverter), energy required for the cooling effort for each drive was estimated from the total losses of each machine and inverter at corner of its toque speed curve. The power required by the cooling pumps was considered as losses for the traction drive because it does not contribute to the useful output energy. Based upon the power rating and flow rate of the commercially available water circulating pumps, it was estimated that 5% power of the total machine and inverter losses (at corner speed) will be required by the cooling pump that will circulate the water in the motor and inverter. This

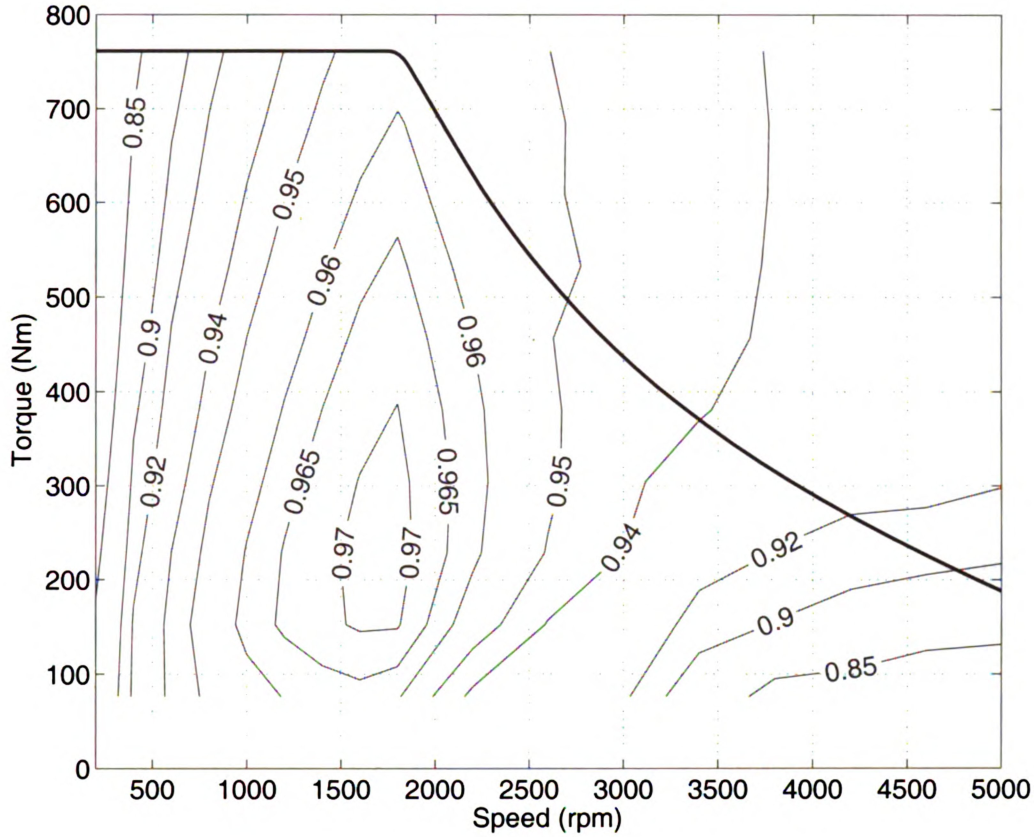

Figure 4.9: Efficiency map of machine M2 including inverter

assumption is used here due to unavailability of the results by transient thermal analysis of the machine and inverter, which can provide the accurate energy required for cooling effort and it is beyond the scope of this work. Although, the machine and inverter losses vary in time during the driving cycle, the cooling pumps usually keep running even during stopover time of the bus. Therefore, the continuous power consumption of 5% of the total machine and inverter losses for the whole time of the driving cycle was reasonable. The calculation for the required cooling energy and its inclusion in the ADCE is given in Table 4.2.

4.7 Calculation of ADCE

The ADCE of the traction drive was computed by calculating the total input and output energy of the traction machine during the complete driving cycle. The electrical machine operates in motoring mode during accelerating and cruising of the bus, and in generating mode during braking. Therefore, input and output power and energy for each case was worked out as per followings:

$$\text{Motoring mode output power} = Torque \times Speed \tag{4.9}$$

$$\text{Motoring mode input power} = Output\ \ power + Losses \tag{4.10}$$

$$\text{Generating mode input power} = Torque \times Speed \tag{4.11}$$

$$\text{Generating mode output power} = Intput\ \ power - Losses \tag{4.12}$$

$$\text{Input Power at } k^{th} \text{ operating point} = P_{i,k} = \frac{P_{o,k}}{\eta_k} \tag{4.13}$$

where $P_{o,k}$ and η_k are the output power and efficiency of the traction drive at the k^{th} operating point respectively. The losses in (4.10) and (4.12) are the sum of the machine and inverter losses and input power of the cooling pump. The ADCE of the driving cycle is the ratio of output to input energy of the traction drive and was calculated by (4.14).

$$\eta_{ave} = \text{ADCE} = \frac{E_o}{E_i} = \frac{\sum_{k=1}^{n} P_{o,k} \cdot t_k}{\sum_{k=1}^{n} P_{i,k} \cdot t_k} \tag{4.14}$$

where $P_{i,k}$ is the input of the traction drive at k^{th} operating point, and E_o, E_i are output and input energies of the traction for the whole driving cycle. n is the number of operating points of the driving cycle and t_k is the corresponding time of the each operating point. t_k is 1 sec for all operating points of FTP driving cycle discussed here . ADCE was calculated using Matlab program. Machine and inverter losses at at every operating point of the driv-

Table 4.2: Calculation of ADCE of two IPMSMs designed for FTP driving cycle

	Machine Parameter	Machine M1	Machine M2
At corner of torque speed curve	Speed (RPM)	1760	1760
	Torque (Nm)	760	760
	Rated current (A)	198	180
	Stator phase resistance (Ω)	0.04	0.04
	Copper losses (W) = a	4704.5	3888.0
	Iron losses (W) = b	535.5	590.0
	Magnet losses (W) = c	17.5	97.0
	Inverter losses (W) = d	2103.0	1858.5
	Total losses ($a + b + c + d$) (W) = e	7360.5	6433.5
	Cooling power ($0.05 \times e$) (W)	368.0	321.7
For driving cycle	Output Energy (kWh)	14.86	14.76
	Machine & Inverter losses energy (kWh)	0.84	1.01
	Energy required for cooling effort (kWh)	0.25	0.22
	Total input energy (kWh)	15.95	15.99
	Average driving cycle efficiency (ADCE) (%)	93.2	92.3

ing cycle were calculated by linear interpolation of the respective efficiency map. Table 4.2 shows the results for both machines under consideration.

4.8 Discussion of Results

Both machines fulfill the driving cycle requirements as shown in Fig. 4.5. Machine M2 has double layer of magnets and needs less stator current for maximum required torque and has less losses on its torque speed envelope boundary. Thus, it needs less cooling effort i.e. a cooling pump of less power to keep the maximum hot spot temperature less than a fixed value. On the other hand, Machine M1 has single layer of magnets and requires more stator current for maximum required torque and thus needs more cooling effort. It looked as M2 would be more suitable design for this application than M1 but this is not the case. When the efficiency map of each of them was generated and ADCE was calculated, it came out that ADCE of M1 and M2 is 93.2% and 92.3% respectively as shown in Table 4.2. It was due to the fact that high energy density contours of M1 were closer to the high energy density of the driving cycle than that of the M2.

Since machine design is an iterative process, many iterations are required to reach the final design. The use of geometric parameterizations in FEM simulations and analysis leads to a design very close to the "optimized design" as M1 was obtained for a specific application.

4.9 Conclusions

An approach based upon the ADCE of a traction drive is presented for the design of an electrical machine for an urban HEV bus. It has been emphasized that the design of the traction drive should have maximum ADCE instead of maximizing its efficiency at one operating point. Since the inverter losses and power required for the machine and inverter cooling are the significant portions of the energy used, they are included in the calculation of ADCE to optimize the machine design. The applicability of this approach was demonstrated by two machine designs. It was shown that design (M1), even though requires more current than design (M2) for the same output torque, has more ADCE and is more suitable design for the specific bus and driving cycle application.

Chapter 5

Overload Considerations for Design and Operation of IPMSMs

5.1 Introduction

Although IPMSMs and their cooling are designed to match the rated power, power demands other than rated may arise. To achieve more power than the original machine design allows, one may keep the same machine dimensions and basic electromagnetic design, but increase the cooling. Overloading without overheating could happen either by increased cooling or only for short period of time without additional cooling. Increase in cooling may be achieved by one or more of the following: changing the coolant type, reducing the inlet coolant temperature and increasing its flow rate. Modifications of the cooling system can compensate for the increase in machine losses in the windings, magnets, or iron. Increasing the allowed stator current affects the machine performance in other ways as well. These include demagnetization of the magnets and hence shrinking of the speed range to avoid this. The effects of overloading and consideration for the design and operation of the IPMSMs are discussed quantitatively in this chapter.

To account for higher stator current with higher temperatures, the effects on efficiency, torque and speed range by changing the magnet material from the more commonly used NdFeB to SmCo are also studied and discussed.

In this chapter, the literature review is given in section 5.2. The adopted analysis approach is outlined in section 5.3. The baseline machine and the cross saturated dq model are presented in section 5.4. The operating range of this machine is discussed in detail in section 5.5. Three alterative designs are presented in section 5.6. Operating limits and efficiency are discussed and compared in section 5.7. The use of SmCo magnets as alternative to NdFeB ones is studied in section 5.8, and finally section 5.9 presents results.

5.2 Literature Review

Overloading of electrical machines increases their temperature and increased cooling is required for continuous machine operation. Due to high power density, IPMSMs are usually designed with a cooling system of forced air, water or oil. Different cooling techniques have been used to keep the machine temperature within limits defined by the magnets and insulation properties [19].

Beyond output power, higher stator current causes changes in the operating range of an IPMSM. The characteristics affected are not only the produced torque, but also the losses in the windings, the magnets and the iron, and hence efficiency. Looking at the machine operation from another viewpoint, it is necessary to change the operating mode with increased current in order to avoid permanent damage to the magnets [20, 21]. This means changes in the angle of the current space vector as well. The limit of the negative d-axis current component to avoid demagnetization of the magnets varies nonlinearly with the magnitude of the stator current and its angle, due to magnetic cross saturation in the d and q axes. Earlier work on overloading of PM machines was presented by Demerdash, Nyamusa and Nehl in [22]. They compared the overload performance of two PM brushless DC machines using different magnet materials. In their work, the effect of demagnetization of the magnets on the machine parameters was addressed in order to analyze the machine performance with partially demagnetized magnets.

Finite Elements Method (FEM) is a powerful and economical tool to design and characterize the performance of electrical machines [23], [24], [25]. Based upon a 2-D FEM analysis, [26] presents the impact of temperature and various grades of NdFeB magnets on the performance of an IPM machine. In [27], the FEM is also employed to evaluate the effect of slot opening on the machine performance for concentrated winding interior and surface PM machines.

5.3 Analysis Approach

Overloading effects are studied for a baseline machine using FEM, as well as for machines with the same stator but modified rotor design. A cross-saturated model is developed using Matlab and shown to be more accurate than the classic one. FEM analysis provided the parameters for the machine model. The operating range for efficient operation was calculated by this model and the demagnetization limit of the magnets was determined by FEM. FEM was also used to tune up the machine geometry [28] for the baseline machine design optimization.

The relationship between increased stator current and machine operating characteristics is explored assuming fixed maximum voltage, stator design, and for the first part, magnet material. It is also assumed that adequate cooling can be provided to keep the windings and the magnets within the appropriate temperature limits, hence, cooling itself is not a topic of this study.

After many design iterations, three viable designs were selected for comparison; they differ in air gap, magnet thickness and bridge width, but have the same stator geometry. Extensive FEM simulations were used to study each design. Standard Matlab programs were used to process the FEM data for the calculation of machine parameters and operating regions under different stator currents.

An alternative to increased cooling with higher current is to use magnets that are more robust with respect to higher temperatures. The use of SmCo magnets was studied here for the same stator geometry, as an alternative to NdFeB, and conclusions were reached regarding losses, efficiency and speed range.

5.4 Baseline Machine Design and Modeling

A 3-phase, 105 kW, 4-pole IPMSM was designed as the baseline machine using FEM iterations. The designed machine was aimed to drive a high power series hybrid bus with

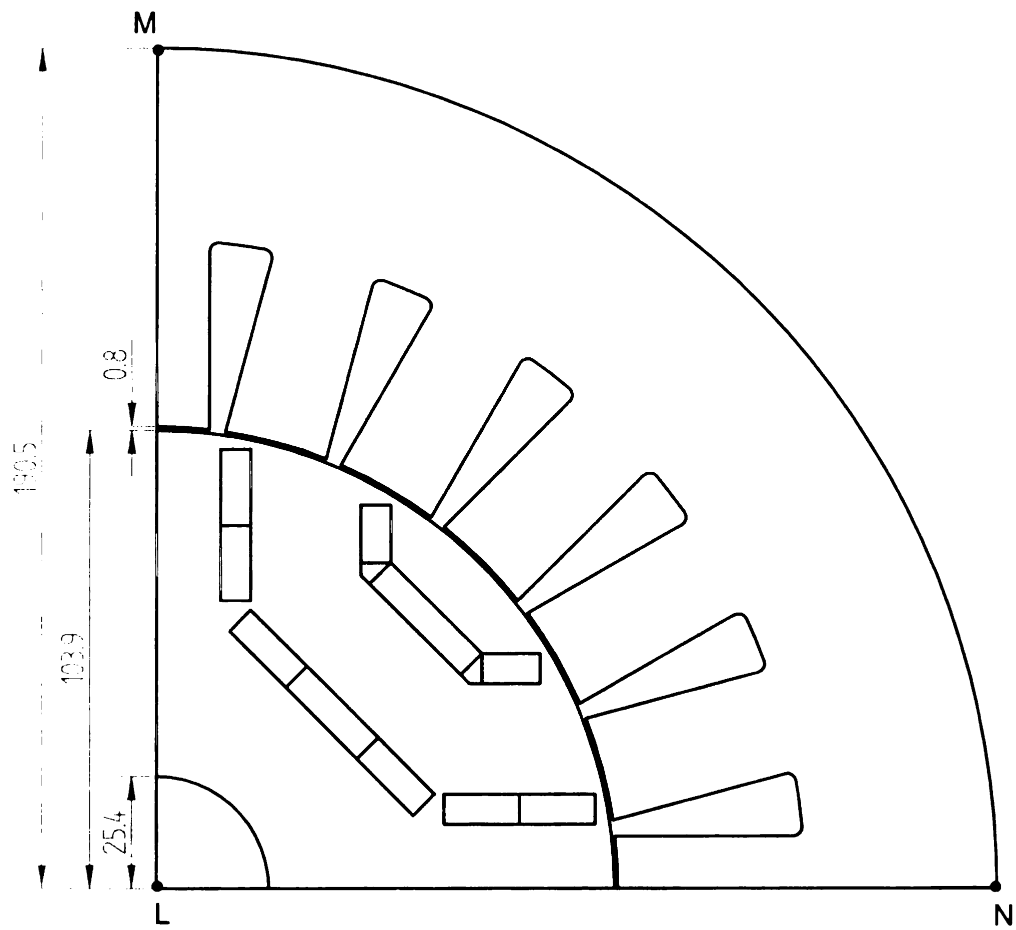

Figure 5.1: Quarter geometry of a 105 kW rated power baseline IPMSM

restricted volume. It is water cooled and has double layer permanent magnet rotor. The machine geometry and its key design parameters are given Fig. 3.1 and Table 3.1 respectively. The same are copied in this chapter in Fig. 5.1 and Table 5.1 for convenience. The cross saturated model of the IPMSM was used to calculate the machine parameters and torque speed envelope of the machine for efficient machine operation as discussed in 3.3.

Although the machine model with cross saturation is relatively complex, it provides more accurate results than the conventional dq model as already mentioned in section 3.3.

Table 5.1: Key parameters of a baseline 4 pole 105 kW IPMSM

Machine parameter	Value
Rated power	105 kW
Rated torque	781.4 Nm
Rated current	140 A
Maximum line voltage	480 V
Corner (base) speed	1285 RPM
Maximum speed	6000 RPM (4.7 pu)
d-axis permanent magnet flux	1.03 Wb
Stator phase resistance	0.17 Ω
Air gap	0.8 mm
Rotor diameter	207.8 mm
Stator diameter	381 mm
Stack length	240 mm
Stator slots	24
Winding type	double layer (Lap)
Slots/pole/phase	2
Number of turns	11 per coil
Magnet grade	NdFeB N35SH
Stator and rotor core	M-19 G24 silicon steel

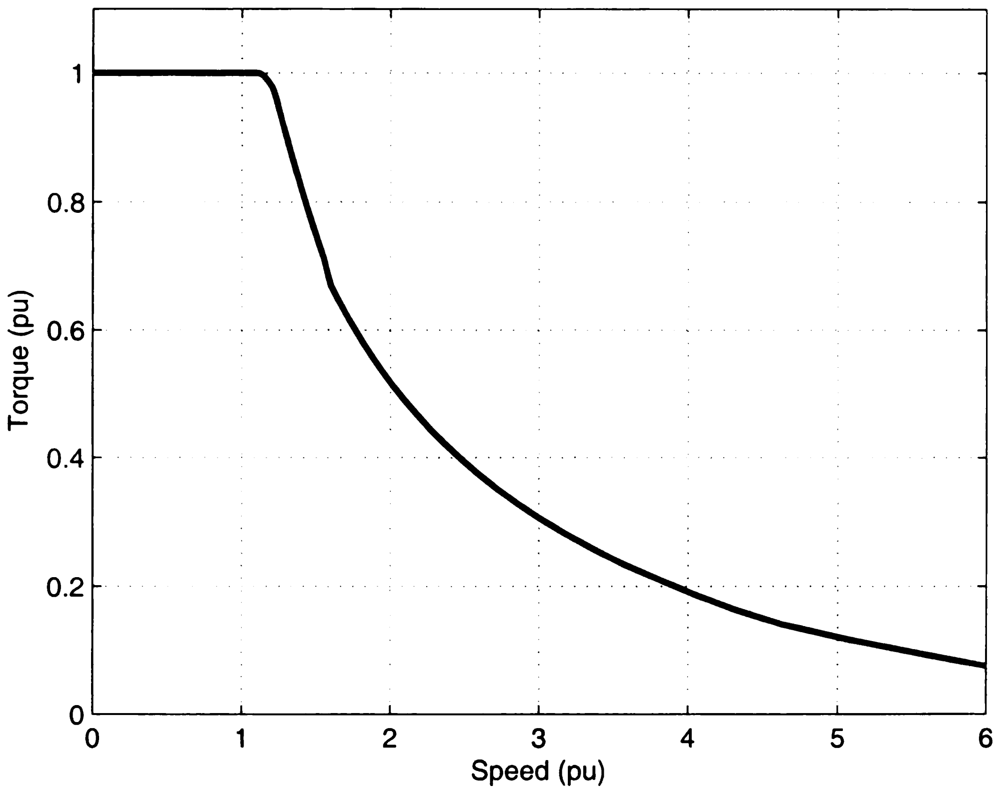

Figure 5.2: Operating range of the baseline machine calculated using cross saturated dq model

Fig.5.2 shows the torque-speed envelope of the baseline machine calculated using the cross saturated dq model, for efficient machine operation.

5.4.1 Demagnetization of NdFeB magnets

To avoid demagnetization of the magnets in IPMSMs, the current in the negative d-axis should be limited. Fig. 5.3 shows the demagnetization curves of NdFeB grade N35SH permanent magnets at different temperatures [29]. It can be seen that 0.5 T is the safe lower limit of magnetic flux density, which is just above the demagnetization knee at 150°C. Therefore, the lower limit of the flux density in the permanent magnets has been set at 0.5 T for the analysis presented here.

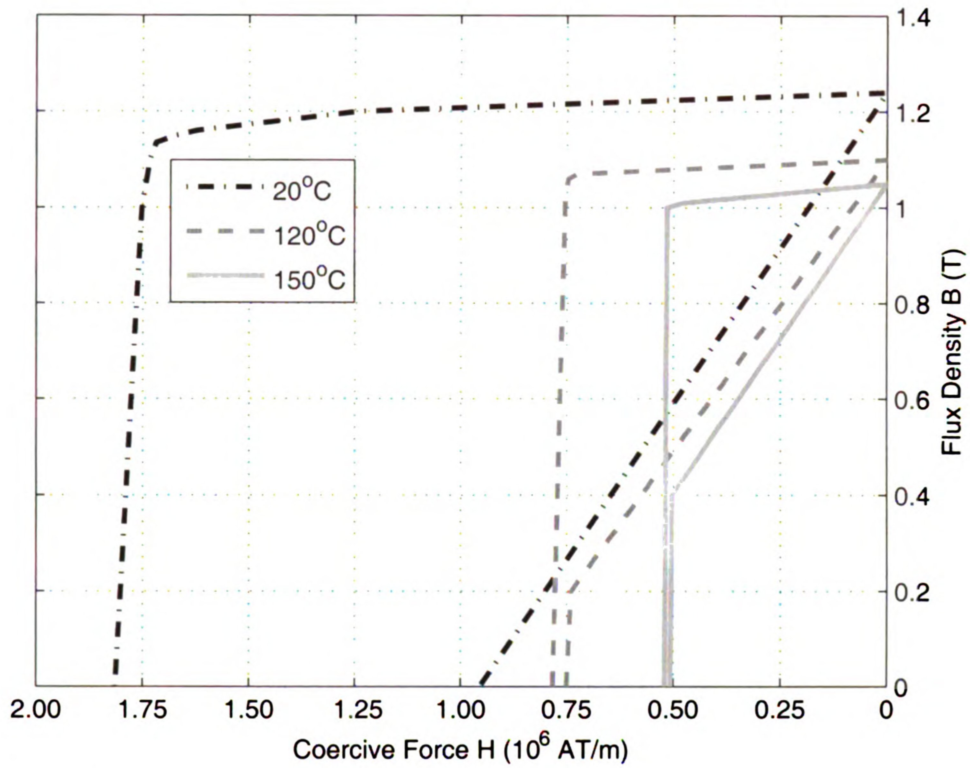

Figure 5.3: Demagnetization curves of NdFeB grade N35SH permanent magnets

When cross saturation in not taken into account, the calculated negative d-axis current corresponding to the demagnetization limit of the permanent magnets remains constant for all stator currents. On the other hand, when cross saturation is considered, this calculated current varies with the q axis current. This topic is discussed further in the next section.

5.5 Baseline Machine Operation

In order to analyze the machine operation, it is assumed that maximum line voltage of the machine is 480 V rms and sufficient cooling is available to keep the machine temperature less than 150°C.

5.5.1 Operation below rated current

Fig. 5.4 shows the the operating curves of the baseline machine at and below rated current. FEM analysis was carried out for different values of the stator current, and its angle was varied from 90° to 180°. At rated current, the maximum speed of the machine in the constant power mode is about 4.4 times the corner speed. Fig. 5.5 shows the flux density when rated current was applied along the negative d-axis. The flux density in the magnets remained above the knee of the demagnetization curve. Therefore, the machine can operate safely up to rated current for all current angles with maximum operating temperature of $150^{\circ}C$. The corner speed and torque of the machine varies with changing stator current as it is shown in Fig. 5.4.

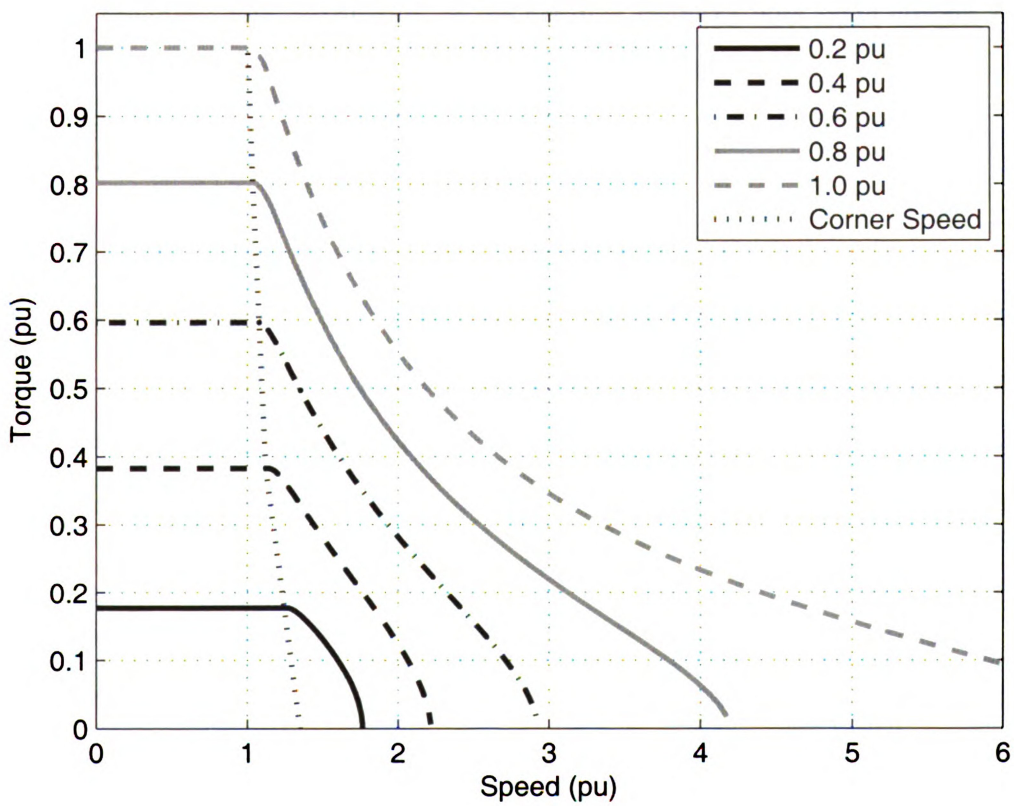

Figure 5.4: Operating curves of the baseline machine up to rated current

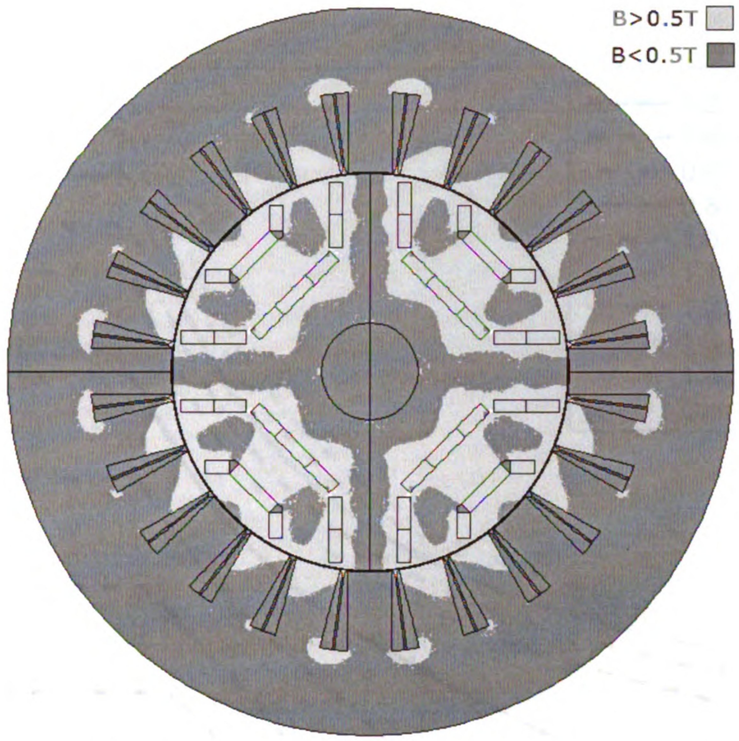

Figure 5.5: Magnetic flux distribution of the baseline machine with rated current along negative d-axis

5.5.2 Operation above rated current

Fig. 5.6 shows the operating curves of the baseline machine for different current levels, including higher than rated. They are calculated from the cross saturated dq model but without considering the demagnetization limit of the magnets. From Fig. 5.6, it appears that the machine can operate with stator current of 1.4 pu in MTPA mode of operation and it can develop 1.37 pu torque. It also appears that the machine with 1.4 pu current has a wider field weakening range than with the rated current.

When the demagnetization limit of the magnets is considered, it is recognized that the operation discussed above is not possible. The machine can still operate safely above its demagnetization limit for maximum current of 1.1 pu with current angle up to 180°. Safe operation at current higher than 1.1 pu requires a decrease in the current angle for an increase in the current magnitude. Fig. 5.7 shows the flux density distribution with stator

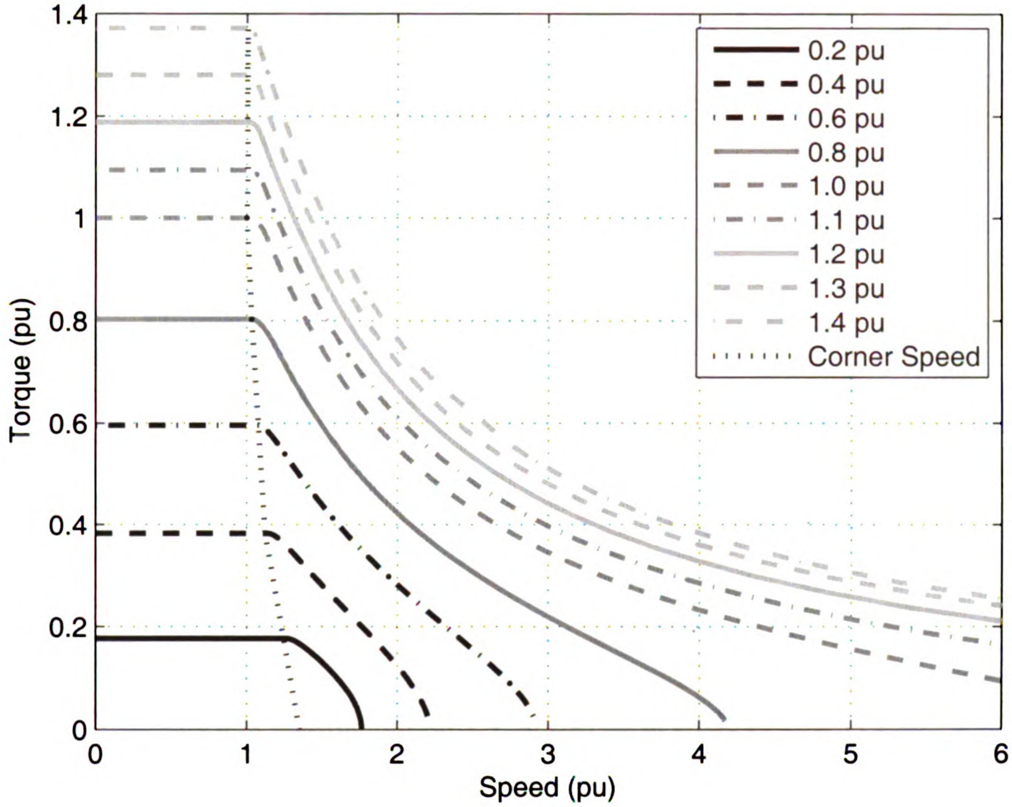

Figure 5.6: Operating curves of the baseline machine without considering demagnetization limit

current of 1.4 pu applied at angle of 135° ($I_d = -0.99$ pu). There the flux density is less than 0.5 T in some portion of the magnets, causing their demagnetization. This of course is not an acceptable machine operation.

Table 5.2 shows the stator current and the corresponding limit of the current angle for both safe and unsafe operating regions when demagnetization is taken into account. Fig. 5.8 summarizes these results in pictorial view, and shows the operating region of the machine. We make the following observations and conclusions from Table 5.2 and Fig. 5.8:

1. Operation up to 1.1 pu current is possible in any region of operation. At this current, the machine provides maximum torque of 1.09 pu below the corner speed and 1.09

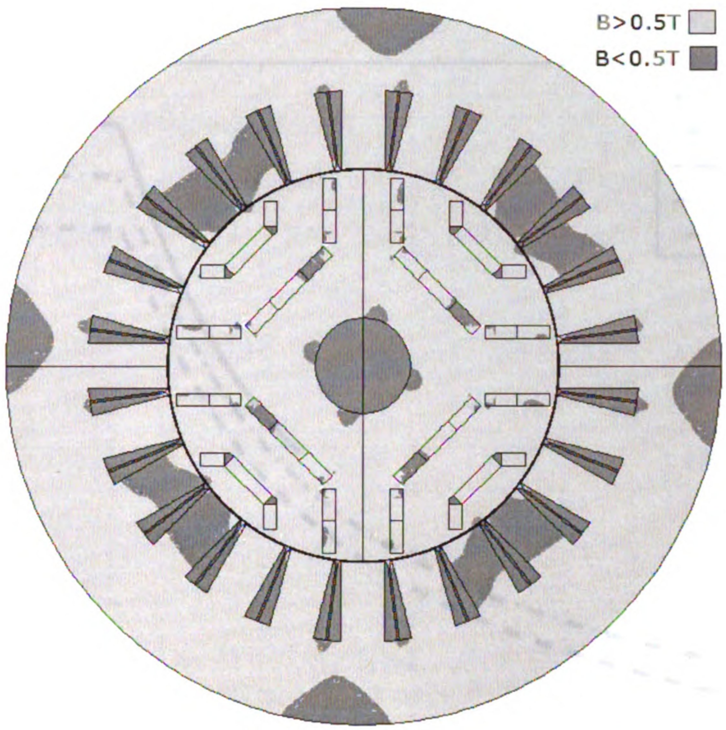

Figure 5.7: Magnetic flux distribution for 1.4 pu current at angle of 135° ($I_d = -0.99$ pu)

pu power in the whole field weakening range.

2. For 1.2 pu stator current, the machine can operate below the corner speed in MTPA mode and produce 1.19 pu torque. However, its maximum speed is limited to 2.25 pu in the constant power region. This is due to the limit on the current angle of 170° in order to operate the machine without demagnetizing the magnets.

3. The operational range of the machine is further limited for higher currents. At 1.3 pu current, the angle for MTPA mode is 143°, while the angle limit is 130° to avoid demagnetization. This means that the machine cannot be driven in MTPA mode of operation. Furthermore, the machine cannot operate in constant power mode as well, because the current angle cannot be increased more than its limit of 130°.

4. Similarly, torque and speed limits are reduced further for 1.4 pu current, as shown in the Table 5.2. Moreover, the machine can't operate at any angle for more than 1.4 pu

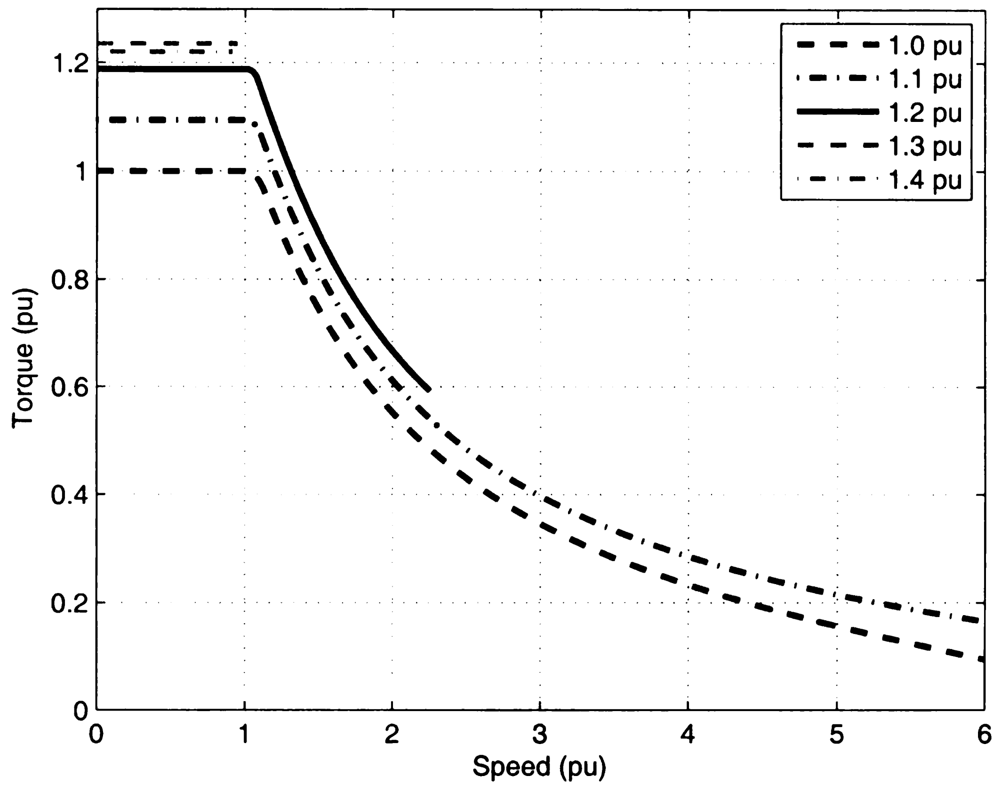

Figure 5.8: Operating curves of baseline machine for rated and higher current considering demagnetization limit of magnets

stator current and this is the upper current limit of the machine.

5. Due to cross saturation, the upper limit of the negative d-axis current is reduced (from 1.18 pu to 0.7 pu) for respective increase in the stator current (from 1.2 pu to 1.4 pu) for safe machine operation.

Table 5.2: Machine operation for MPTA mode and demagnetization limit

Stator current (pu)	**Without considering demagnetization**			**To avoid demagnetization**		
	Max current angle	I_d (pu)	Max Torque (pu)	Max current angle	I_d (pu)	Max torque (pu)
1.0 (rated)	136.5°	-0.73	1.0	180° *	-1.0	1.0
1.1	139.5°	-0.84	1.09	180° *	-1.1	1.09
1.2	141.0°	-0.93	1.19	170° *	-1.18	1.19
1.3	143.0°	-1.04	1.28	130°	-0.84	1.23
1.4	145.5°	-1.15	1.37	120°	-0.70	1.22

* Angle higher than required for MTPA operation without considering demagnetization. It shows that machine operation is safe up to corner speed under MTPA for the corresponding stator current.

5.6 Machine Design Variants for Operation Above Rated Current

In this section, the machine is redesigned in order to achieve the best operational characteristics with increased cooling. In this exercise the total machine volume, magnet grade, iron core and outer dimensions are kept constant. In the analysis of the machine operation, the stator current is increased to take advantage of the better cooling, while the magnets are not demagnetized.

Keeping the stator unchanged, three possible variations of the rotor are selected:

- Increased air gap.
- Thicker magnets.
- Increased bridge width.

Fig. 5.9 shows the geometry of rotor and air gap for the baseline machine and three

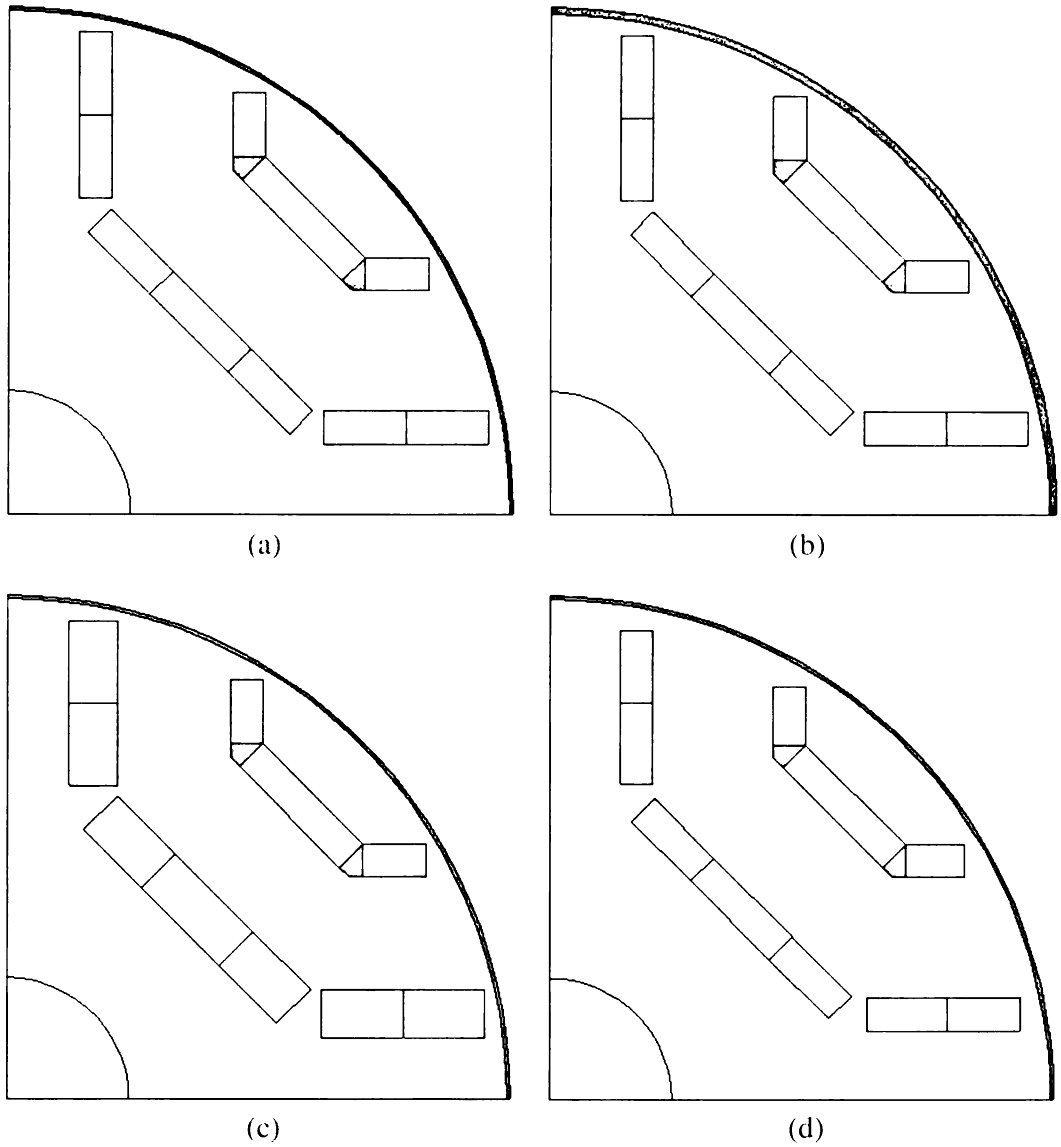

Figure 5.9: Comparison of different designs: (a) baseline machine; (b) increased air gap; (c) thicker magnets; (d) increased bridge width.

design variants. In each design, the light and dark gray shades represent the magnets and air respectively. FEM and Matlab programs are used for each case to find the machine parameters, operating range, demagnetization limit, and corresponding magnitude and angle of the stator current.

In the remaining part of this chapter, rated conditions (1 pu), refers to those of the baseline design. The design modifications for each option are discussed with respect to the baseline machine. Maximum current for each design refers to maximum stator overload current that can be used in the full speed range without demagnetization of the magnets. Maximum speed of machine is the speed, when its torque is reduced to 0.2 pu in the constant power region.

5.6.1 Increased air gap

The air gap of machine was increased to twice than that of the baseline machine. This was done by adding 0.8 mm depth from the stator teeth to the air gap, however, the slot opening of the stator and rotor remained unchanged. Fig. 5.9b shows the resulting rotor geometry.

This design provides less torque at rated current but allows higher maximum stator current (1.2 pu) than that of the baseline machine. Fig. 5.10 shows the operating range of this machine for rated current and higher than that. The torque is reduced to 0.93 pu for rated current. The maximum torque in MTPA mode is 1.12 pu and the maximum power in the whole field weakening region is 1.14 pu. They can be achieved at maximum stator current of 1.2 pu. The maximum speed during field weakening at rated and maximum current is almost the same as that of the baseline design.

5.6.2 Thicker magnets

In this design variation, the thickness of the internal layer of magnets was increased to 1.5 times that of the baseline machine, while the thickness of the outer layer remained unchanged. Fig. 5.9c shows the geometry of this machine. This was opted because it is the internal layer which demagnetizes first due to high current in the negative d-axis.

The operating ranges of the thicker magnet machine for rated and higher stator current are shown in Fig. 5.11. It provides the same torque (1.0 pu) as that of the baseline machine at rated current but allows much higher current (1.4 pu) producing maximum torque of

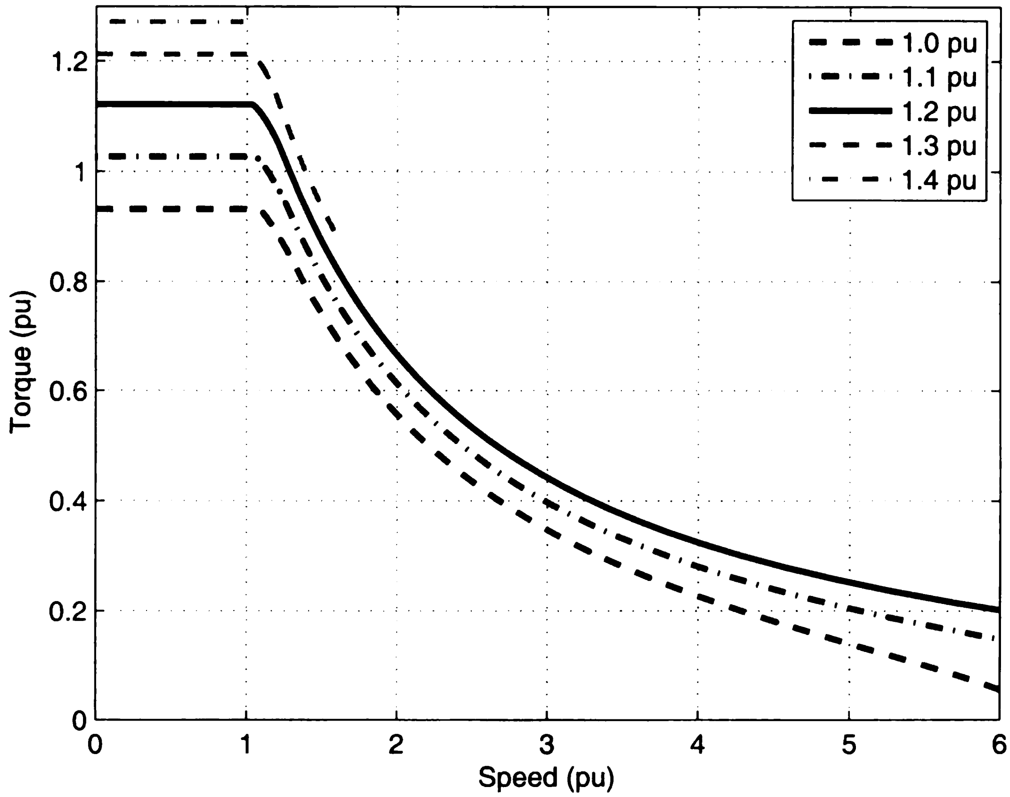

Figure 5.10: Operating curves of the machine having increased air gap

1.38 pu. The maximum speed at the rated and maximum current is 3.7 pu and 6.2 pu respectively.

5.6.3 Increased width of bridges

The bridge width (the minimum distance between any magnet and the rotor surface or between two magnets in the rotor core) has been increased to twice than that of the baseline machine. The magnet width and the air gap remained unchanged. Fig. 5.9d shows the geometry of the machine with increased bridge width.

Like the increased air gap design, this design provides less torque at rated current but allows higher maximum stator current (1.2 pu) than that of the baseline machine. Fig. 5.12

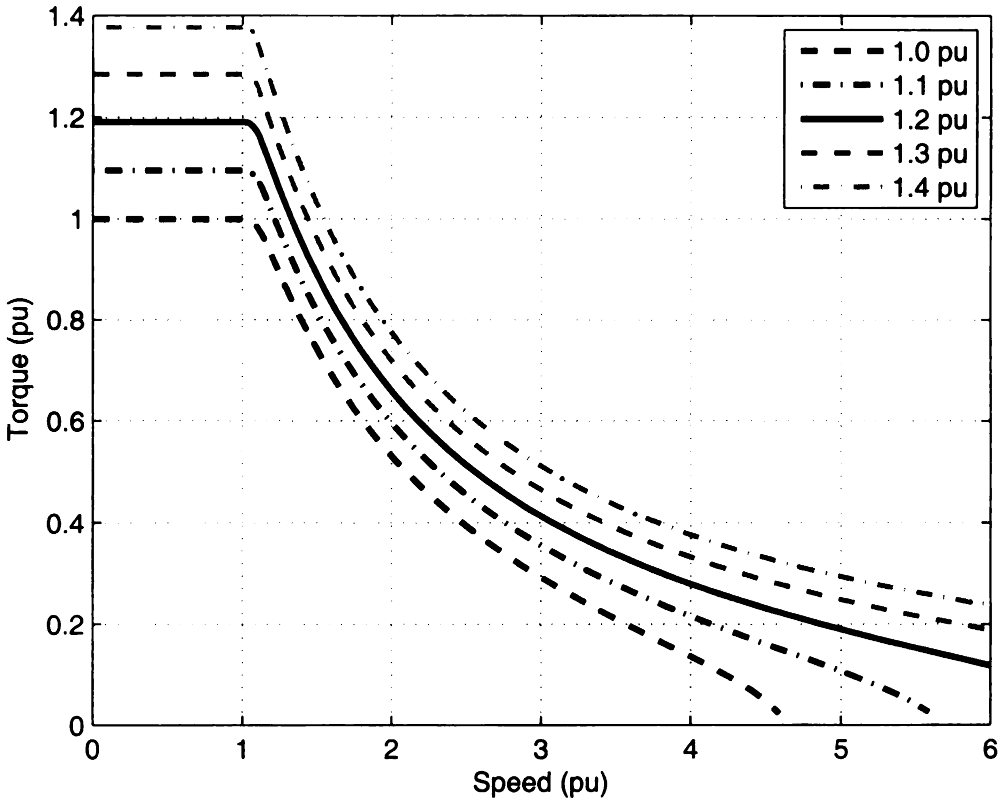

Figure 5.11: Operating curves of the machine having thicker magnets

shows the operating range of the machine for rated current and higher. It was observed that torque is decreased to 0.94 pu for the rated current. Maximum current is 1.2 pu, which can produce 1.21 pu of torque and 1.25 pu of power in the field weakening range. In this design, maximum speed with field weakening, both at rated and overload conditions, is almost the same, about 5.2 pu.

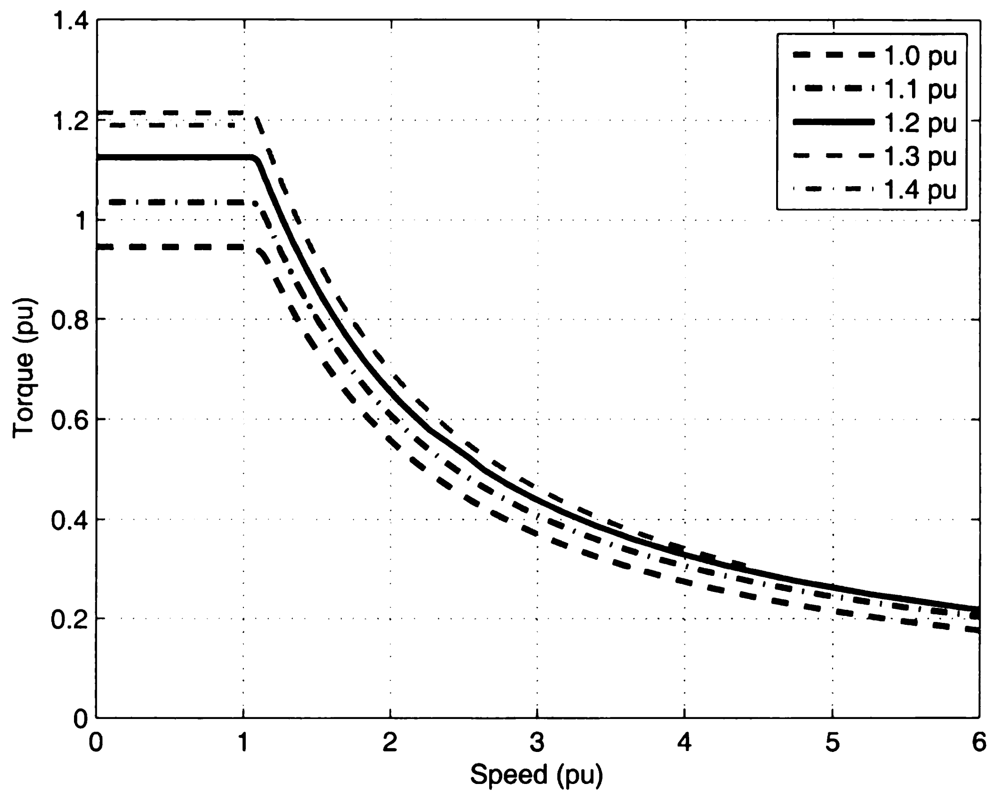

Figure 5.12: Operating curves of the machine having wider rotor bridges

5.7 Comparison of Machine Design Variants

5.7.1 Operating regions

Table 5.3 compares three designs in terms of torque, power and maximum speed at rated and maximum current. Thicker magnet design allows higher maximum current and develops more torque and power than other designs. Although, at the rated current, its maximum speed (3.7 pu) is less than that of the baseline machine (4.4 pu). But, at maximum current, its maximum speed is more than that of the baseline machine. This shows that torque speed envelope of the baseline machine is the subset of the thicker magnet machine. Therefore, thicker magnet design is the best choice for the machine operation at higher currents without changing its size. The additional losses will have to be compensated for by the increased

Table 5.3: Comparison of machine design variations

Design Parameter	Machine Design Variants			
	Baseline Machine	Increased Airgap	Thicker Magnets	Wide Bridges
Max torque at rated current (pu)	1.0	0.93	1.0	0.94
Max current (pu)	1.1	1.2	1.4	1.2
Max torque at max current (pu)	1.09	1.12	1.38	1.21
Max power in constant power region (pu)	1.1	1.14	1.39	1.25
Max speed at rated current (pu)	4.4	4.4	3.7	5.2
Max speed at max current (pu)	5.1	5.1	6.2	5.2

cooling.

Since the permeability of NdFeB permanent magnets is almost the same as that of air, one can consider the effect of adding a layer of air equal to the increased thickness of magnets to increase reluctance torque. Fig. 5.13 shows the geometry of this machine, which has an air layer of thickness equal to the half of the magnet thickness, along the internal magnet layer. Fig. 5.14 shows the operating range of this machine under different current conditions, taking demagnetization into account. This design is not acceptable, because the machine cannot operate in MTPA mode even at its rated current. It can operate in full speed range up to 50% of the rated current (0.5 pu) due to demagnetization limit of the magnets. Furthermore, the maximum speed of this machine is much less than that of the

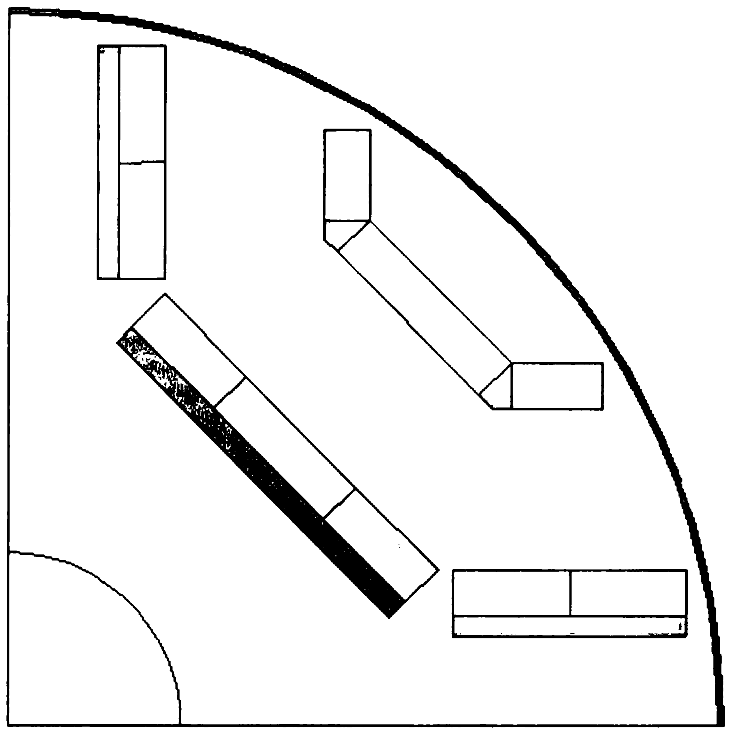

Figure 5.13: Geometry of the machine having air with internal magnet layer

baseline machine, because it can not operate in field weakening for current above 0.5 pu. Comparing this design to one with thicker magnets, its operating range is too small. This is caused by less flux in the magnetic circuit due to increased reluctance, and demagnetization starts with less stator current.

5.7.2 Efficiency

The baseline machine was an optimized design for efficient operation in the specific region of operation. Although increased cooling of the machine with thicker magnets allows for wider operation range, one can expect it to also cause performance degradation. These effects are discussed in this section.

The four machine design variants were compared for efficiency at the rated torque and speed. It can be seen from figures 5.8, 5.10, 5.11 and 5.12 that the corner speed of all designs is almost 1 pu at rated current. However, the developed torque is different, summa-

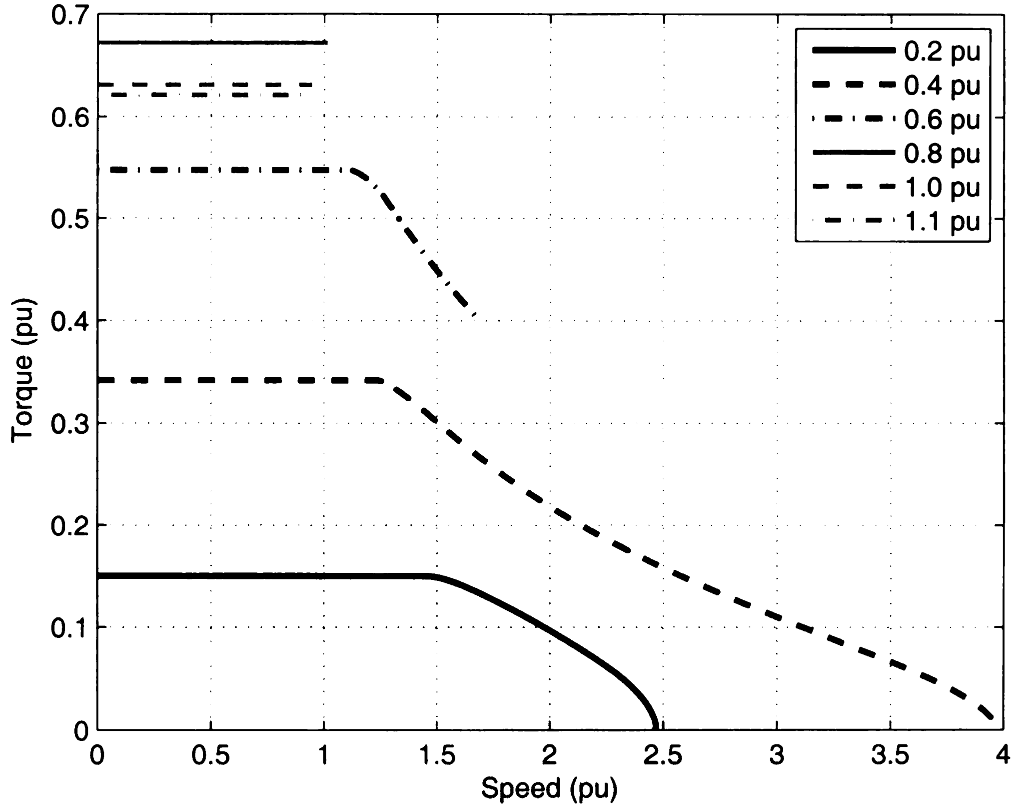

Figure 5.14: Operating curves of the machine having air with internal magnet layer

rized in Table 5.3. Rated current produces less than 1.0 pu torque for two designs (increased air gap and wide bridges), i.e. they require more than the rated current to produce rated torque. Higher current increases losses, reducing the efficiency of machine. Consequently, the design with thicker magnets has efficiency equal to that of the baseline machine at rated torque and speed.

The efficiency of the baseline and the thicker magnets designs is further compared for full speed range under efficient machine operation. Copper losses are calculated from the winding resistance and they are the same for a fixed stator current for all designs discussed in this chapter. Iron and magnet losses are computed from FEM analysis of the two designs. Following observations are made from this analysis:

1. The baseline and thicker magnet designs have the same efficiency at lower speeds, however at higher speed the efficiency of the thicker magnet design is less than that of the baseline machine. Fig. 5.15 shows comparison of efficiency vs speed of both designs at rated current. The thicker magnet design has less d-axis inductance and more flux of permanent magnets for the same stator current, resulting in reduction of the field weakening range compared to the baseline design. Consequently, at a fixed speed and current in the field weakening operation, the thicker magnets design provides less torque. This causes a sharp reduction in the efficiency for the thicker magnets design at higher speeds.

2. The efficiency of the thicker magnets design at its maximum current (1.4 pu) is less

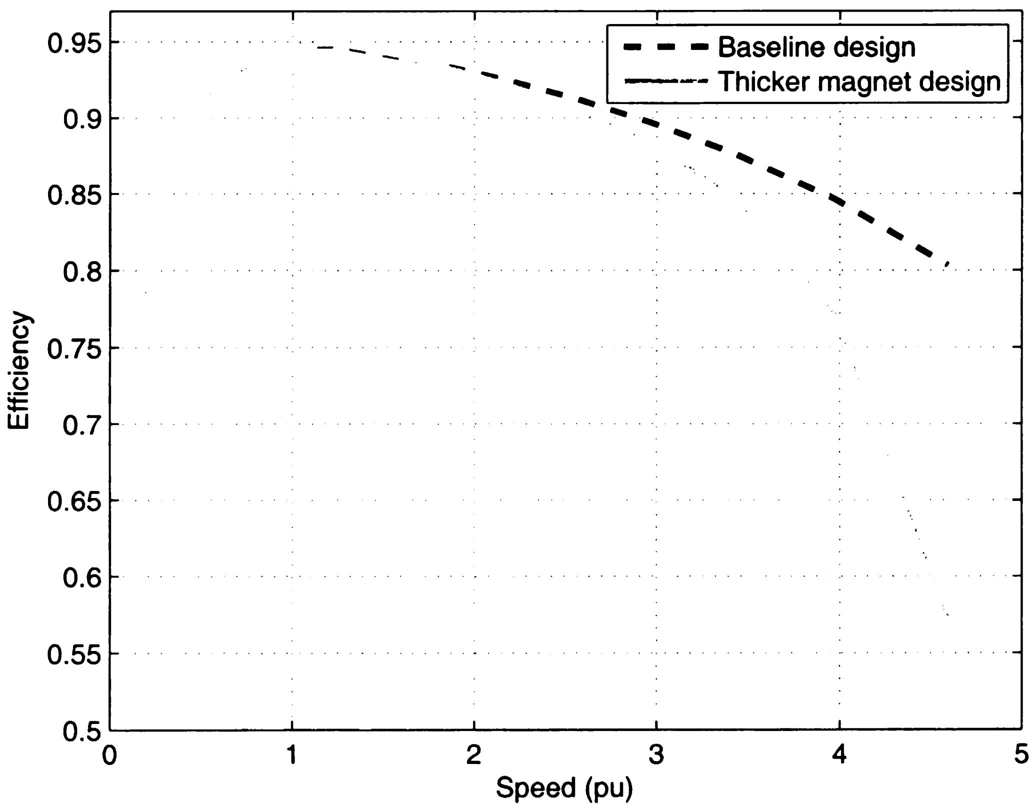

Figure 5.15: Efficiency vs speed comparison at rated current

than the efficiency of the baseline design at its maximum current (1.1 pu) for the whole speed range and Fig. 5.16 shows this result. Comparing these two designs at rated speed, the increase in the iron and copper losses of the thicker magnet design is 5% and 62% respectively; on the other hand the increase in its output power is only by 26%.

The thicker magnets design provides wider torque speed operating range with increased cooling, but at the cost of reduction in the efficiency for higher speeds at rated current.

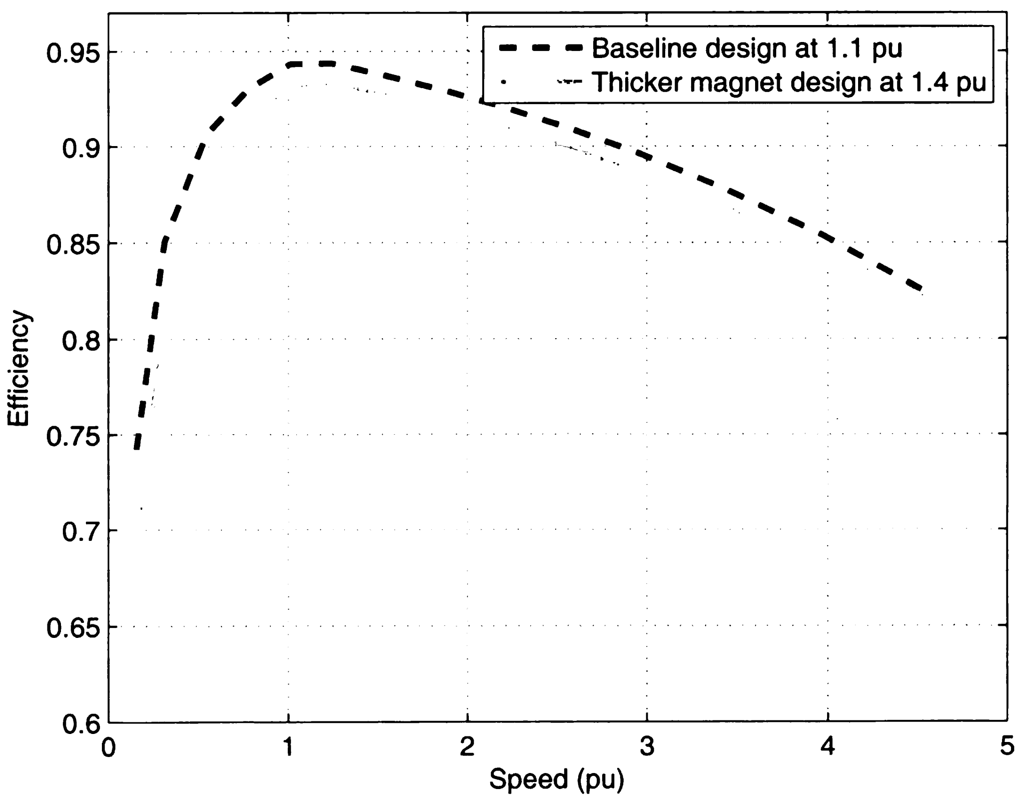

Figure 5.16: Efficiency vs speed comparison at maximum current

5.8 NdFeB vs SmCo magnets for overload operation

The machines discussed in this chapter so far used NdFeB magnets. However, SmCo magnets are an alternate option for the design of high power density machines intended for high temperature operation [30]. The differences in the machine operating range and its efficiency are investigated here for NdFeB (grade N35SH) and SmCo (grade 2:17) magnets [31]. SmCo magnets have lower B_r but higher operating temperature than NdFeB magnets, as shown in Table 5.4. Unlike NdFeB magnets presented in Fig. 5.3, the demagnetization curves of SmCo magnets do not exhibit a knee, and therefore they don't get demagnetized at low flux density.

SmCo magnets for the same magnetic circuit generally produces lower flux density. To perform the analysis in this section, of the rotor geometries analyzed for NdFeB magnets, the one with the thinner magnets was selected, i.e. the baseline machine design discussed in section 5.4. The design with thicker magnet was considered previously to avoid demagnetization of the NdFeB magnets, which is not a concern here, while it did not produce appreciatively higher magnet flux, which would have been desired with SmCo magnets. All geometrical parameters of the design remain unchanged.

The FEM analysis was used to study the performance of both machines. We compare the current, torque and efficiency under three different load conditions at the corner speed. The results are summarized in Table 5.5 and the following observations are made:

1. In order to achieve the same (rated) torque, the SmCo machine requires more current

Table 5.4: Magnetic characteristics of NdFeB and SmCo magnets

Material	$B_r(T)$	$H_c(kA/m)$	$BH(kJ/m^3)$	μ_{rec}	$Max\ T\ (^\circ C)$
NdFeB	0.7–1.41	310-1500	35-385	1.05-1.25	80-200
SmCo	0.55-1.15	360-820	56-246	1.02-1.1	300-550

Table 5.5: Comparison of baseline machine operation using NdFeB and SmCo magnets

Comparison at corner speed	**Machine parameter**	**NdFeB machine**	**SmCo machine**
Rated torque	Current (pu)	1.0	1.1
	Efficiency (%)	94.7	93.5
Rated current	Maximum torque (pu)	1.0	0.91
	Efficiency (%)	94.7	94.1
1.3 pu current	Maximum torque (pu)	1.23	1.18
	Efficiency (%)	93.3	92.9
	Operation beyond corner speed	No	Yes
Maximum operating temperature		150°C	300°C

(1.1 pu) and has lower efficiency than the NdFeB machine.

2. At rated current, the SmCo machine produces lower torque and efficiency than the NdFeB one. The difference in the efficiency of the two machines is less, due to equal copper losses, which are dominant at the rated current.

3. At 1.3 pu current, torque of both machines is comparable. Efficiency difference is also less. Reduced torque by NdFeB machine is due to the current angle constraint imposed by demagnetization limit of the magnets, and therefore MTPA operation could not be realized. The SmCo machine can operate beyond corner speed at overload condition, whereas NdFeB can't.

Within rated operation and at maximum temperature (150°C for N35SH), the NdFeB magnets machine is more efficient than that of SmCo. Efficiencies of NdFeB and SmCo machine are comparable under overload conditions. For high temperature, SmCo is the sole choice. Moreover, SmCo magnets provide full speed range for higher overload operation

Table 5.6: Summary of design and analysis of IPMSMs

Machine parameter	Baseline design	Thicker magnet NdFeB	SmCo magnets
Maximum current	1.1 pu	About 27% increase in current and torque	
Max torque at max current	1.09 pu		
Max speed at max current	5.1 pu	21% increase	31% decrease
Efficiency at rated current at corner speed	94.7%	Negligible change	
Efficiency at rated current at 3.5 $\times$ corner speed	87.3%	3.6 % decrease	6.7% decrease
Maximum Temperature	150°C	150°C	300°C

than the NdFeB magnets, irrespective of the machine temperature.

Table 5.6 summarizes the findings of this chapter.

5.9 Summary and Conclusions

The design and operation of an IPMSM has been explored for overload operation. The cross saturated dq model provides more accurate machine parameters than conventional dq model. NdFeB magnets are used to achieve high power density. Demagnetization of the magnets is taken into account in the analysis, which occurs for one of two reasons: high temperature and low flux density in the magnets, caused by large current along the negative d-axis.

Machine operation for higher than rated stator current can be achieved with increased cooling. Any specific design of IPMSM can operate safely up to power higher than rated, if such room is provided by the designer. For even heavier overloading the machine maximum speed has to be reduced and its torque-speed envelope shrinks. Analysis of an optimized baseline design of 105 kW IPMSM is presented for gradually increasing overload conditions. Demagnetization is shown to be the result not only of negative d-axis current, but also of the cross-saturation caused by the q-axis current component.

The IPMSM can be redesigned in more than one ways to increase the operation range under improved cooling. In the design variations studied here, the magnet grade, iron core and machine volume remained the same. Among three design modifications in the rotor geometry, thicker magnets design allowed more overload operation with full speed range but with reduced efficiency as compared to the baseline design.

As an alternate to increased machine cooling, the rotor geometry of the baseline machine but with SmCo magnets was also analyzed. The machine with SmCo magnets shows lower efficiency than the NdFeB machine at rated operation. However, SmCo allowes full speed range overload operation at higher temperature.

Chapter 6

Characteristics of Magnet Materials and Their Consideration in the Design of PMSMs

6.1 Introduction

Rare earth magnet materials are the basis of good performance of Permanent Magnet Synchronous Machines (PMSMs) [32]. NdFeB magnets are usually the first choice for the design of high power PMSMs due to their high energy. Special attention is required for the design of PMSMs for elevated temperature operation, which can happen due to severe weather and/or insufficient cooling. This requirement motivates for the consideration of different magnet materials for design of PMSMs.

The characteristic parameters of permanent magnets vary with temperature. They are remanent flux density, coercivity, and demagnetization flux density. The rate of change in these parameters with temperature is different for each magnet material. High power PMSMs for vehicle application can face temperatures outside the range of -35°C to 190°C, therefore, their operating temperature is an important design consideration. Due to temperature dependent characteristics of the magnets, a PM machine designed for a specific operating temperature shows different characteristics with temperature variation. Therefore, it is necessary to analyze the machine performance over its intended operating temperature range.

The operating temperature of PMSMs is limited by maximum temperature of the windings insulation and the magnets. High temperature winding insulation and SmCo or ferrite magnets are options for high temperature machine operation. The use of high temperature winding insulation does not affect the machine's operating characteristics. On the other hand, different magnet materials and machine temperature have significant impact on the machine performance, and this issue is explored in this chapter.

SmCo magnets are a substitute of NdFeB magnets for high power PM machines. The remanent flux density of NdFeB magnets reduces with increase in temperature at faster rate than that of the SmCo magnets, and it becomes comparable at high temperature. One of the objectives of this chapter is the design considerations of an IPMSM for wide temperature environment using NdFeB and SmCo magnets. Initially, An IPMSM was designed using NdFeB magnets for its optimum operation to meet torque speed requirements of an urban Federal Test Procedure (FTP) cycle for a series hybrid bus. Then, the machine was redesigned using SmCo magnets. Quantitative performance analysis of the both machines was carried out at two different temperatures for each design with NdFeB as well as SmCo magnets. Demagnetization of the magnets is taken into account considering flux and temperature variation during machine operation. Comparison of torque speed and efficiency is worked out for every design option.

Design of high power PMSMs using ferrite magnets is the second topic of discussion. Ferrite magnets can also work at higher temperature than that of the NdFeB. A machine design using ferrite magnets is intended for the same application of series hybrid bus for FTP driving cycle. Ferrite magnets have less remanent flux density and thus ferrite PMSMs have have less power density. Issues have initiated about the availability of rare earth magnet materials across the world [33]. In case of their non-availability, ferrites magnets could be the only choice for PM machines utilized in the emerging technology of HEVs and wind energy. This motivates the design of PMSMs without using rare earth magnets. A few variants of PMSMs using ferrite magnets are discussed including flux squeeze design [34]. Comparison of their torque speed characteristics leads to the selection of potential design for hybrid bus application.

FEM is used to determine machine parameters. Torque speed envelopes and efficiency are calculated by writing a program code in the Matlab. Cross saturated machine model [8] is employed to determine the machine operating range for maximum torque per ampere operation [6] below corner speed and operation under maximum current and voltage above corner speed. Copper losses are calculated analytically and iron losses are computed by the FEM. Magsoft's Flux2D is used as a FEM tool for design and analysis.

6.2 Literature Review

Different approaches are used by researchers and engineers for the design and performance analysis of electrical machines. In [35], thermal analysis of PMSMs and temperature rise for different rotor configurations shows that the magnets of surface PM machines are more vulnerable to get demagnetized than that of the interior PMSMs. Design and analysis of an IPMSM was presented for field weakening range using extensive FEM in [36]. Optimization of rotor saliency and machine efficiency is discussed for the design of an IPMSM in [37]. The issues of design and analysis of PMSMs for high temperature application and design for high power density machines without using rare earth magnets is not explored so far in the literature.

6.3 Properties of Permanent Magnets and Their Selection

Significant variations exists in the characteristics of the magnet materials used for electrical machine applications. Four types of permanent magnet materials are commonly utilized for PM machines. They are NdFeB (Neodymium Ferrous Boron), SmCo (Samarium Cobalt), AlNiCo (Aluminium Nickel Cobalt) and Ferrites. Fig. 6.1 shows typical demagnetization characteristics of each material type and Table 6.1 lists the range of their parameters.

NdFeB magnets have highest B_r and H_c but their maximum operating temperature is less than that of the SmCo magnets. SmCo have high operating temperature, a little less B_r than NdFeB but they have more conductivity than NdFeB. AlNiCo have minimum H_c but can work at high temperatures. Finally, ferrites have medium H_c, lowest B_r and relatively high operating temperature. Comparing the relative cost, SmCo are the most expensive

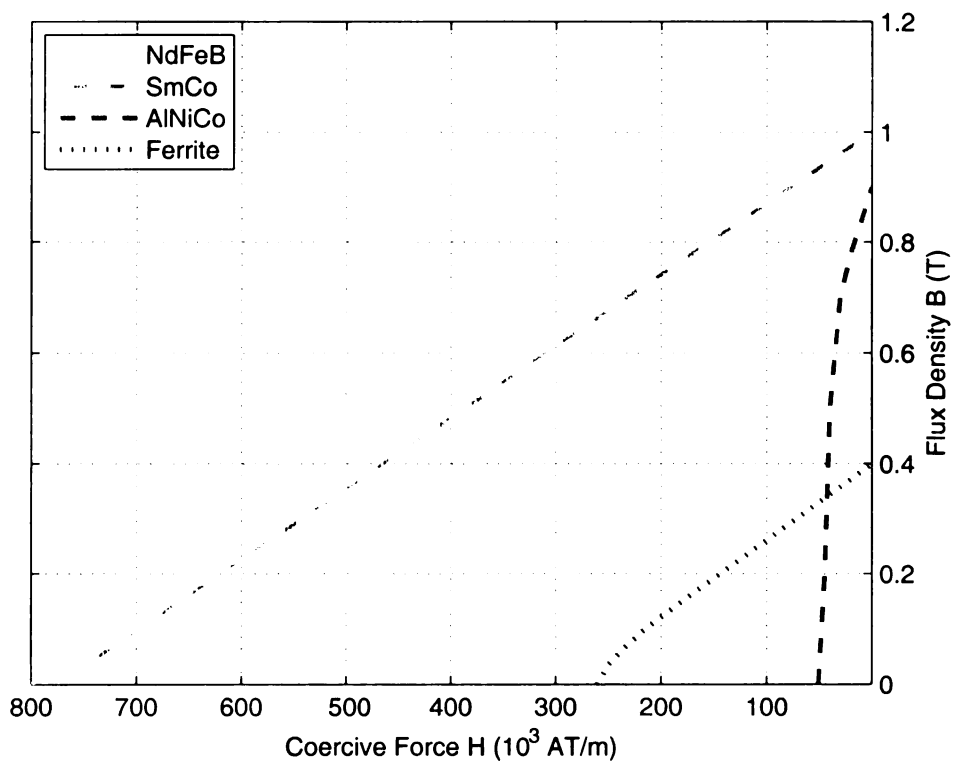

Figure 6.1: Demagnetization characteristics of magnet materials

Table 6.1: Characteristics of permanent magnet materials

Parameter	NdFeB	SmCo	AlNiCo	Ferrite
B_r (T)	0.7–1.41	0.55–1.15	0.7–1.35	0.22–0.42
H_c (kA/m)	310–1500	360–820	44–151	151–254
BH (kJ/m^3)	35–385	56–246	11.0–59.0	9.0–33.0
μ_{rec}	1.05-1.25	1.02-1.1	1.5–4	1.05–1.35
T_{opt} $(°C)$	100–200	200–550	200–500	100–250
α_{B_r} $(\%/°C)$	-0.11	-0.035	-0.02	-0.18
β_{H_c} $(\%/°C)$	-0.6	-0.3	-0.015	+0.4
σ $(\Omega^{-1}m^{-1})$	0.63×10^6	1.25×10^6	2×10^6	1×10^{-6}
Relative Cost	$$$	$$$$	$$	$

and ferrites are the cheapest. The range of operating temperature of the different magnets (given in Table 6.1) is also a key factor in deciding their usage in a specific application.

High power IPMSMs experience large stator currents and are often operated under field weakening. Apart from the field weakening beyond corner speed, a magnetic field opposing permanent magnets is also generated in Maximum Torque Per Ampere (MTPA) mode, below the corner speed [5], [6], [8], [38]. Therefore, the flux density in the permanent magnets is reduced by stator current in MTPA and constant power region of operation. High power density PMSMs have large stator ampere turns and therefore, permanent magnets are always vulnerable to get demagnetized. At the same time, high air gap flux density from permanent magnets is also demanded for high power density. NdFeB and SmCo magnets have relatively high B_r and H_c; they are more suitable for high power density PMSM. On the other hand, AlNiCo magnets are not feasible for such machines due to their low H_c.

6.4 Demagnetization of Permanent Magnets

A permanent magnet, while installed in a PMSM, can get demagnetized by either of the two reasons; temperature rise higher than its maximum operating temperature, or flux density reduction in the magnet less than that of the knee of the demagnetization curve. Insufficient cooling and increase in the iron and magnet losses cause the temperature escalation in the magnets. On the other hand, flux density in the magnets is reduced by stator current applied along the negative d-axis of the machine. Flux density reduction in the magnets has nonlinear relationship with current magnitude and angle due to cross saturation of the PMSMs [38].

Furthermore, the flux density corresponding to the knee of demagnetization curves is also temperature dependent as shown in Fig. 5.3, 6.2 and 6.3 for NdFeB, SmCo and Ferrite

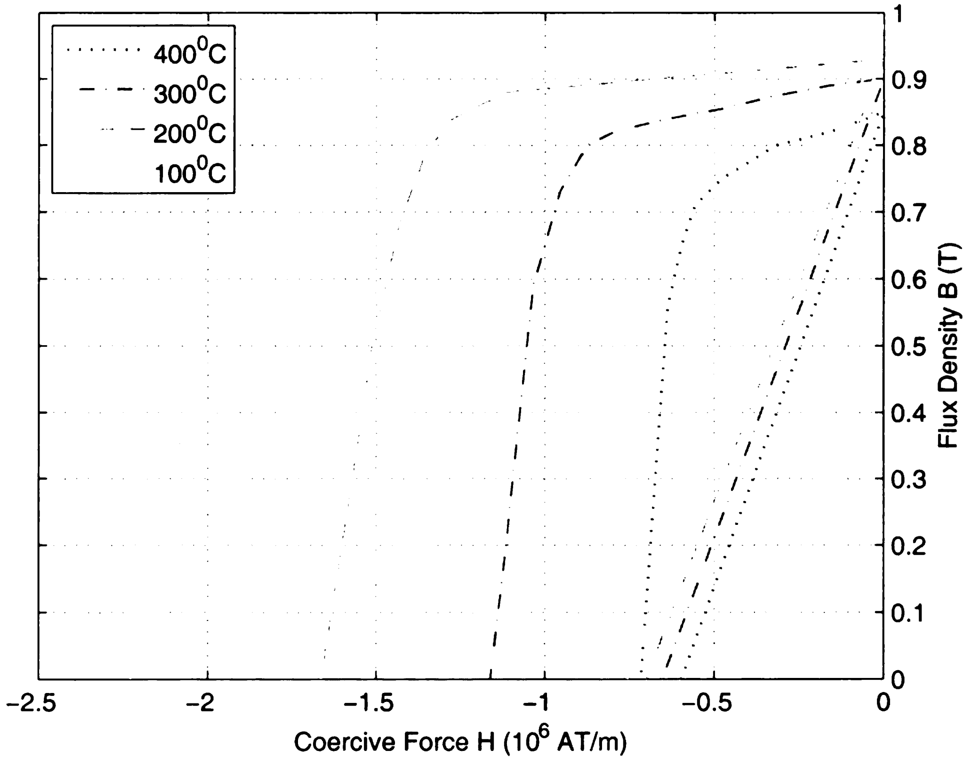

Figure 6.2: Demagnetization curves of SmCo grade 2:17 magnets

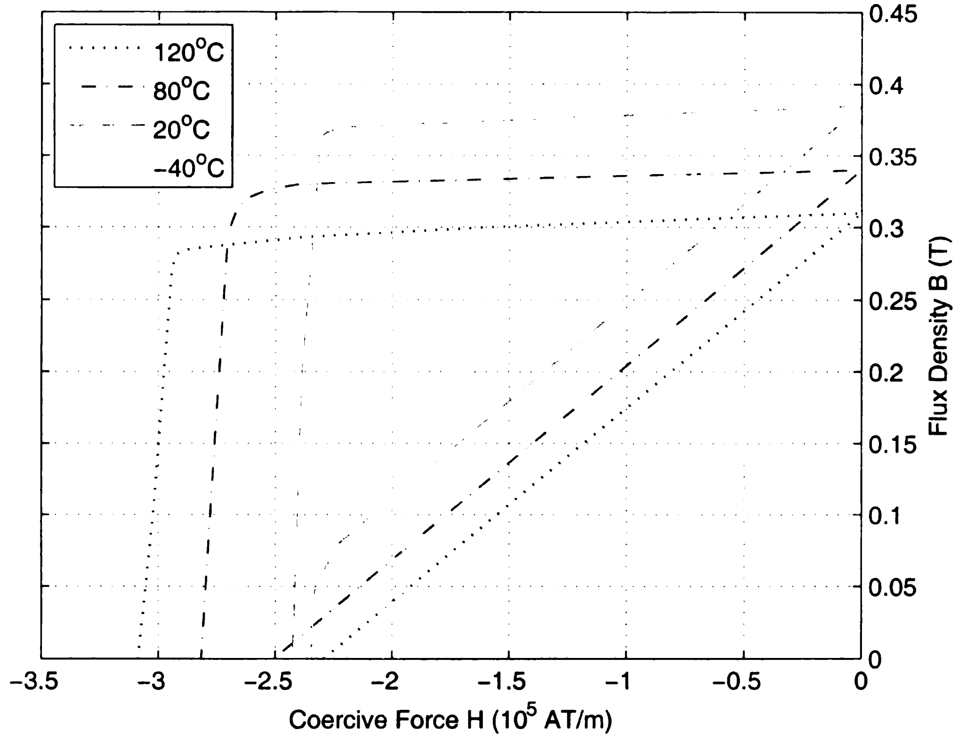

Figure 6.3: Demagnetization curves of Ferrite magnets

magnets respectively. For example, Fig. 5.3 shows that knee of the demagnetization curve of NdFeB grade N35SH lies at 0.2T and 0.4T for magnet temperatures of 120°C and 150°C respectively. The reduction in B_r and H_c with increase in temperature are due to negative thermal coefficients α_{Br} and β_{Hc} as mentioned in Table 6.1. Ferrite magnets have positive thermal β_{Hc}, that shows their demagnetization occurs with temperature drop. Therefore, before getting demagnetized, the minimum flux density in the magnets (knee point) varies with temperature and the negative d-axis current.

It is a safer practice to design a machine and its control for the worst case. It dictates that if the maximum current is applied along negative d-axis of the machine, the flux density in the magnets should not be reduced less than the knee of the respective demagnetization curve within the operating temperature range of the magnets. This criterion is used for all machine designs discussed here for the demagnetization limit of the magnets.

6.5 Effect of Magnet Materials and Temperature

The temperature of electrical machines increases much higher than the room temperature during their operation especially that of high power density machines. To achieve the required characteristics of the PM machines, it is necessary to take into account the effect of temperature variation that machines will be face during their operation. This consideration is explored here for design of two different machines using NdFeB and SmCo magnets, which are the potential candidates (based upon their high B_r and H_c) for high power density PM machines. The performance of both machines is evaluated at two different temperatures.

Magnet material and its grade is selected based upon the operating temperature and the required air gap flux density to match the torque speed requirements for FTP driving cycle shown in Fig 4.2. The maximum operating temperature of the machine depends upon the thermal design of the machine. It is assumed that thermal design of the machine ensures safe machine operation.

6.5.1 Machine designs

Based upon high B_r and H_c of the NdFeB magnets as discussed in section 6.3, they are the first choice in order to design high power density PM machines. NdFeB magnets have different grades within its family, which vary in B_r and maximum operating temperature as shown in Table 6.2.

The power requirements of traction motor for a series hybrid bus are based upon the FTP driving cycle as described earlier in section 4.4. The design is aimed to cover maximum possible torque speed points of Fig. 4.2. Fig. 6.4 and 6.5 show the geometry and torque speed envelope respectively of NdFeB machine designed to meet the driving cycle requirements of Fig. 4.2. The rated machine parameters are tabulated in Table 6.3. The torque speed envelope was calculated using the cross saturated model for efficient machine

Table 6.2: Grades of NdFeB magnets

Magnet grade	B_r **(T)**	**Maximum operating temperature** ($^\circ$**C**)
N	1.17-1.48	80
NM	1.17-1.45	100
NH	1.14-1.42	120
NSH	1.08-1.37	150
NUH	1.08-1.29	180
NEH	1.04-1.26	200

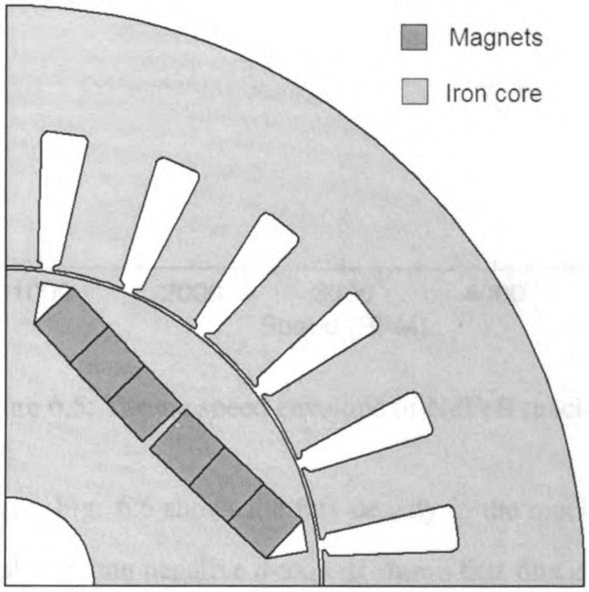

Figure 6.4: NdFeB machine geometry

operation as described in section 3.3. The line voltage is 480 V in all designs presented here. Furthermore, the parameters values of this NdFeB machine listed in Table 6.3 are used as base values for the other designs. Maximum speed refers to the speed when torque at rated current is 0.3 pu.

Since the NdFeB magnets experience a knee in their demagnetization curves, it is important to evaluate their possibility of demagnetization during their operation and it was calculated by FEM analysis. Flux density in the magnets was observed for varying current

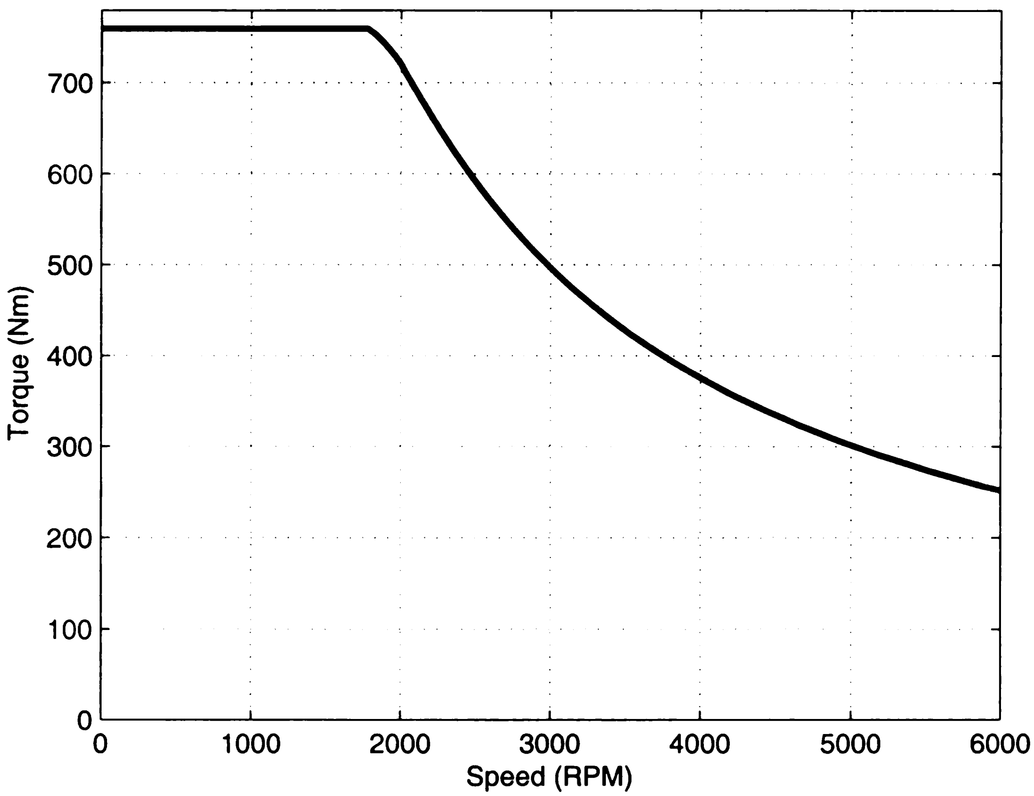

Figure 6.5: Torque speed envelope of NdFeB machine

magnitude and its angle. Fig. 6.6 shows the flux density in the machine, when maximum current (1.4 pu) is applied along negative d-axis. It shows that flux density in the magnets remains more than 0.45T. The knee of demagnetization curve of N35SH at 150°C is 0.4 T as shown in Fig. 6.4. Therefore, the safe machine operation is ensured for maximum current applied at any angle and to have sufficient machine cooling to keep the magnets temperature less than 150°C. FEM analysis shows that demagnetization of the magnets starts for current higher than 1.4 pu in negative d-axis.

In order to operate the machine at temperatures higher than 200°C, SmCo magnets replace the NdFeB magnets in the Fig. 6.4 as a first iteration. Since SmCo magnets have less flux density than that of the NdFeB, the SmCo magnets can not just replace the NdFeB magnets to have similar machine performance. Rotor of the NdFeB machine discussed was

Table 6.3: Key parameters of the machine designed with NdFeB magnets

Machine Parameter	Value	Machine Parameter	Value
Rated power	140 kW	Rated torque	760 Nm
Rated current	198 A	Line voltage	480 V
Corner (base) speed	1760 RPM	Stack length	200 mm
Maximum speed	7000 RPM (4.00 pu)	Air gap	1 mm
Maximum current	235 A	Stator diameter	330.2 mm
Winding type	double layer (Lap)	Stator slots	24
Coil pitch	150° Elect	Rotor diameter	180 mm
Magnet grade	NdFeB N35SH	Number of turns	6.5 per coil
Stator and rotor core	M15G29 silicon steel	Slots/pole/phase	2

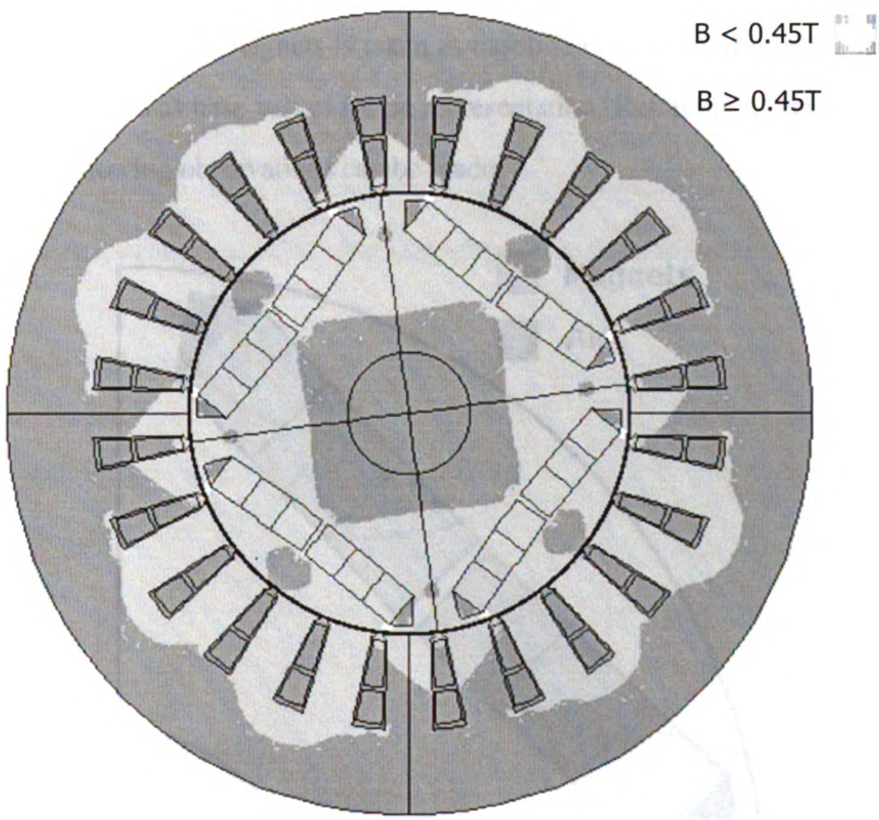

Figure 6.6: Flux density in NdFeB magnets with maximum current in negative d-axis

redesigned as rotor B shown in Fig. 6.8. Rotor of machine shown in Fig. 6.4 is named as rotor A for comparison purposes ans is shown in Fig. 6.7. Rotor B (Fig. 6.8) was designed to have more air gap flux density considering that the basic design criteria remains the same i.e. to meet the torque speed requirements of the hybrid bus for FTP driving cycle.

6.5.2 Design comparison and discussion of results

Two variants of IPMSM, whose rotors are shown in Fig. 6.7 and 6.8, are compared to study the effect of magnet materials and temperature variation on the machine performance. Both machines have same outer diameter, stack length and identical stators.

The machine performance results discussed here are in pu quantities. Machine designed with rotor A using NdFeB magnets is taken as baseline machine and its parameters given in Table 6.1 are taken as base values for pu representation. Refereing to Table 6.4 and Fig. 6.9 and 6.10, following observations can be made:

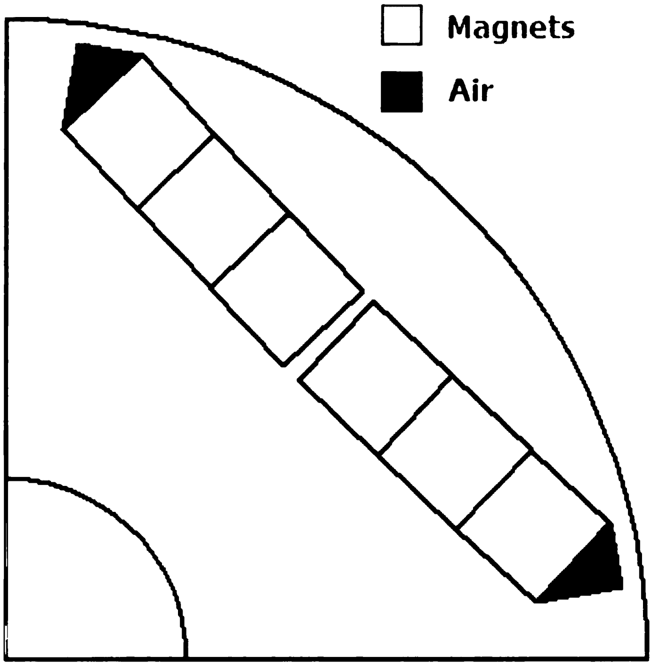

Figure 6.7: Rotor design A

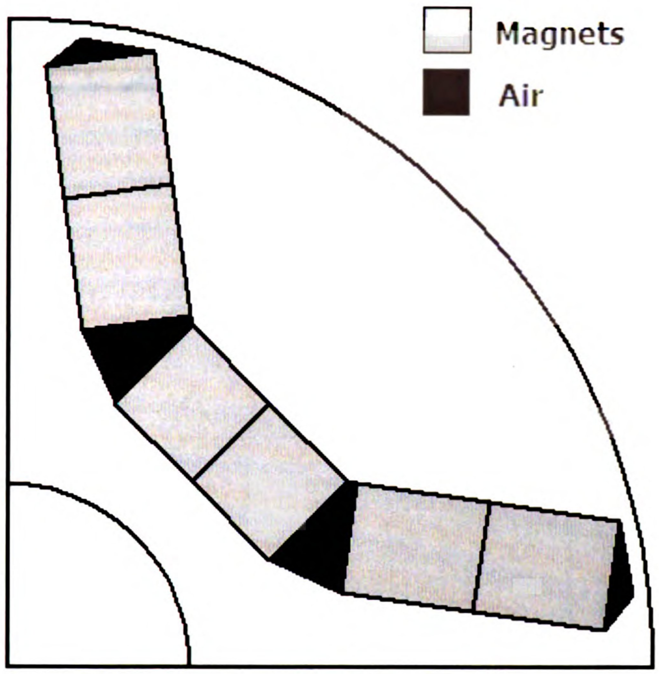

Figure 6.8: Rotor design B

Table 6.4: Comparison of machine design variations at different temperatures

Machine design variants and operating temperature			Current for demanded torque (up to corner speed)	Maximum speed in FW (pu)	% Efficiency at corner speed
Rotor A	NdFeB	50°C	1.0	3.69	96.3
		190°C	1.13	2.72	93.2
	SmCo	50°C	1.18	2.72	95.3
		190°C	1.35	2.42	92.7
Rotor B	NdFeB	50°C	0.95	3.07	96.6
		190°C	1.06	3.46	94.0
	SmCo	50°C	1.06	3.46	95.8
		190°C	1.10	3.09	93.6

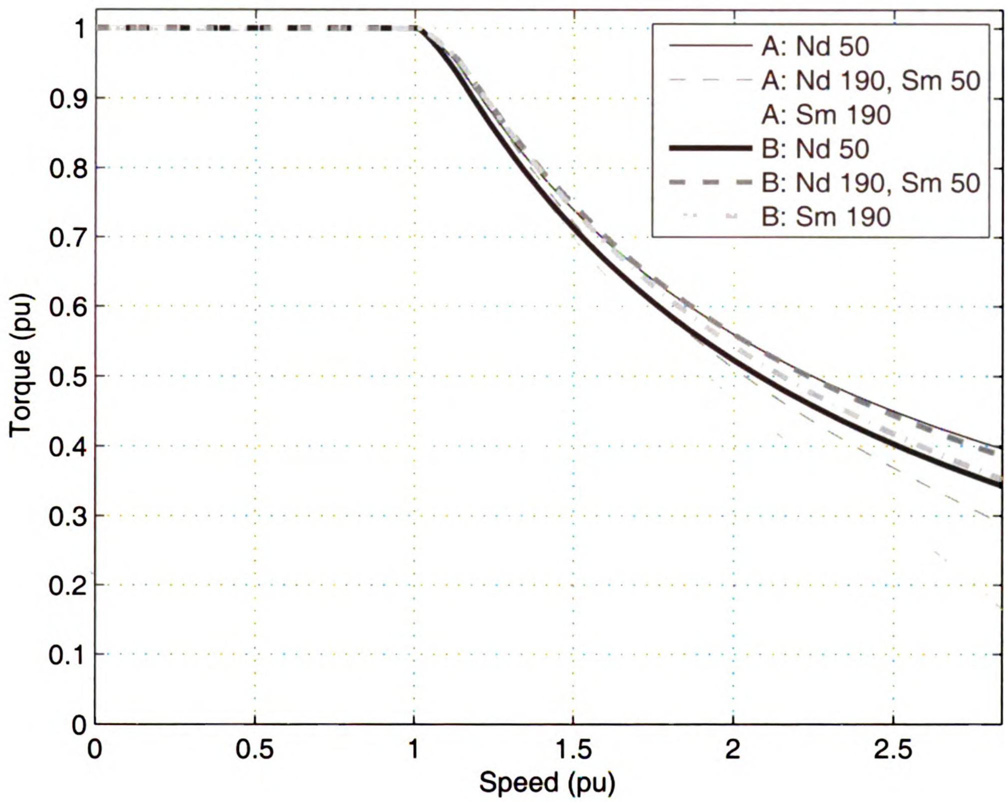

Figure 6.9: Operating range of four NdFeB and SmCo machine variants at two different temperatures

1. At low temperature (50°C), rotor design A with NdFeB magnets is the best choice. It has maximum speed (3.69 pu) in the field weakening among all other design options and provides efficiency of 96.3% at corner speed.

2. At high temperature (190°C), irrespective of the magnet materials, design A can not meet the torque speed requirements of the driving cycle due to its less field weakening range. Furthermore, its efficiency at corner speed is reduced (93.2% for NdFeB and 95.3% for SmCo magnets) due to higher current required to provide the base torque.

3. Design B is suitable for high temperature (190°C). NdFeB magnets provide wider field weakening and high efficiency than the SmCo magnets in this case too.

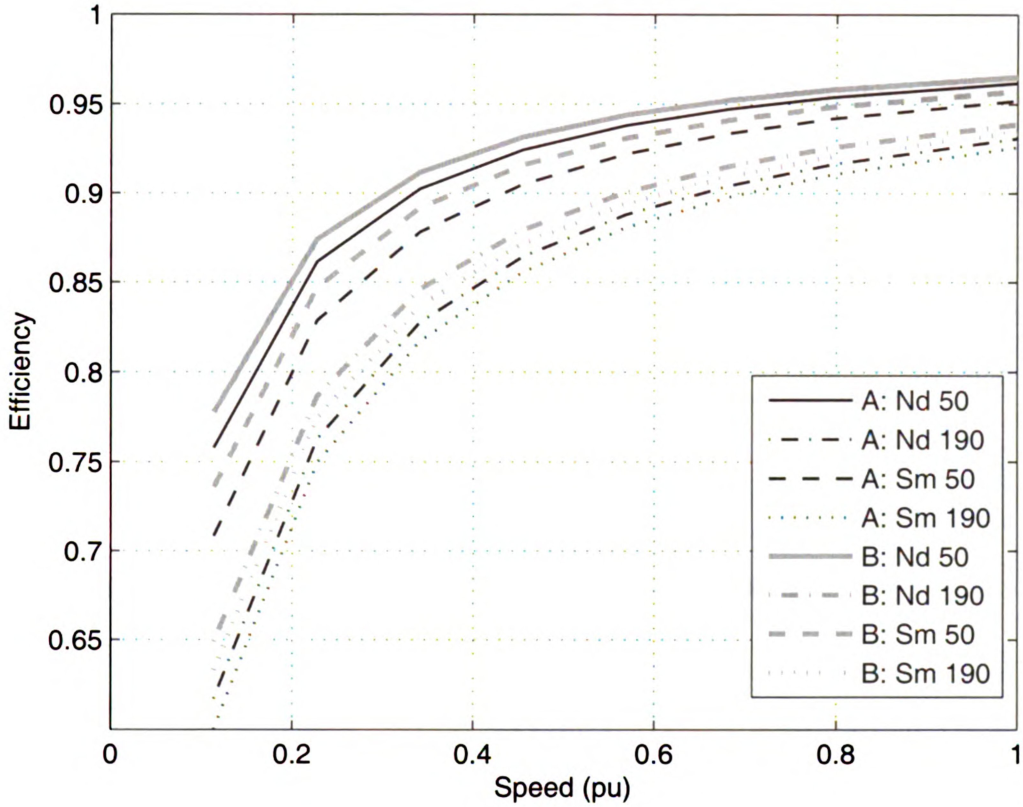

Figure 6.10: Efficiency of four NdFeB and SmCo machine variants at two different temperatures

4. Efficiency of machines as shown in Fig. 6.10 is compared up to the corner speed. Above the corner speed, higher is the current, lesser is the efficiency for same output torque of a machine because additional current contributes towards the machines losses.

5. For wide temperature range (50°C-190°C) of operation, both NdFeB and SmCo magnets used in rotor B have almost the same maximum speed in field weakening. However, NdFeB magnets exhibit higher efficiency than SmCo magnets over the whole temperature range.

6. NdFeB is the preferred magnet material to be used for wide temperature range up

to 200°C (the maximum possible temperature for NdFeB). However, the machine design should be optimized for high temperature. Rotor B is the optimized design for high temperature using NdFeB magnets, and for low temperature using SmCo magnets.

7. SmCo magnets is the only solution for temperature higher than 200°C. Furthermore, a machine designed with SmCo magnets for lower temperature can work over a wide range of temperature without much decrease in the field weakening range and efficiency as compared to the NdFeB magnets.

6.6 Machine Design Using Ferrite Magnets

6.6.1 Machine design variants

Ferrite magnets can work at temperature higher than 200°C. Moreover, the availability of rare earth magnet materials at reduced cost across the world is becoming an issue. Therefore, the possibility of using ferrite magnets is explored here for design of high power machines e.g. HEVs applications. Ferrites have low B_r than NdFeB and SmCo magnets as mentioned in Table 6.1. Therefore, a machine designed with ferrite magnets will provide less torque density than that of a machine using NdFeB/SmCo magnets for the same machine volume. To achieve the maximum possible power density without using rare earth magnets, various design options are explored including the flux squeeze (FS) design [39]. The operation of ferrite magnet machine is limited at lower end of temperatures (-20° to -40°) due to their demagnetization as shown in Fig. 6.3.

The feasible design variants were explored by varying numbers of turns, slots, poles, rotor diameter and the placement of the magnets. Outer diameter of stator, stack length and the speed range (required for FTP driving cycle) were kept same as that of the baseline machine. Flux Squeeze (FS) design as well IPM design were tried. Initially, the ferrite

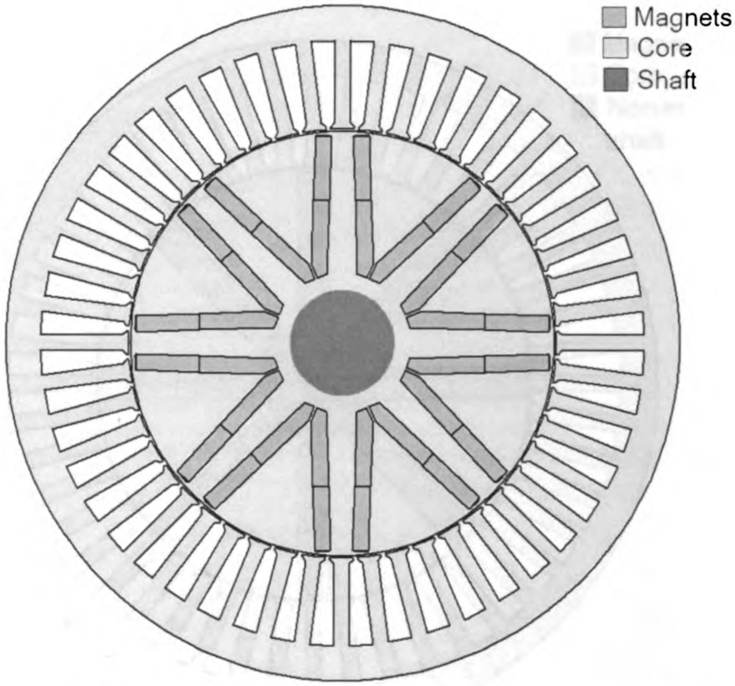

Figure 6.11: 8 pole IPM machine using ferrite magnets (Machine C)

magnets were inserted in the machine B, whose stator and rotor are shown in Fig. 6.4 and 6.8 respectively. Three more design were analyzed. Fig. 6.11 shows machine C, which is a 8 pole IPM. Similarly, machine D and E are 8 and 12 pole flux squeeze machines using ferrite magnets and are shown in Fig. 6.12 and 6.13 respectively. Flux squeeze design impart more air gap flux density but they don't provide the reluctance torque component that is available from IPM machines.

6.6.2 Discussion of results

Since the ferrite magnet machine have lesser torque density than that of the machine using rare earth magnets, the comparison is made for maximum available torque and efficiency at corner point of torque speed curves. Fig. 6.14 shows the torque speed ranges of four different ferrite magnet machines. Table 6.5 summariness the comparison of the results. We make the following observations:

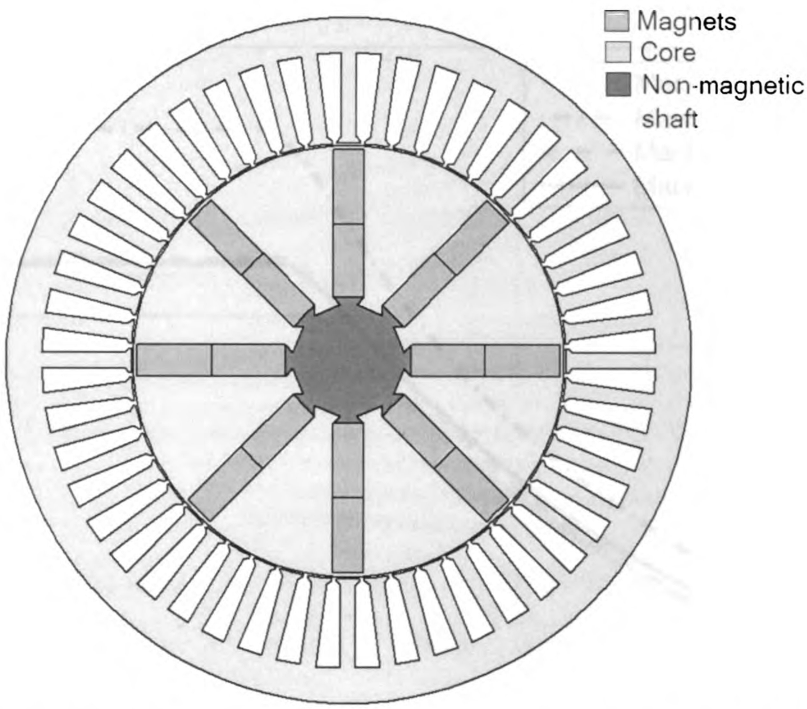

Figure 6.12: 8 pole flux squeeze machine using ferrite magnets (Machine D)

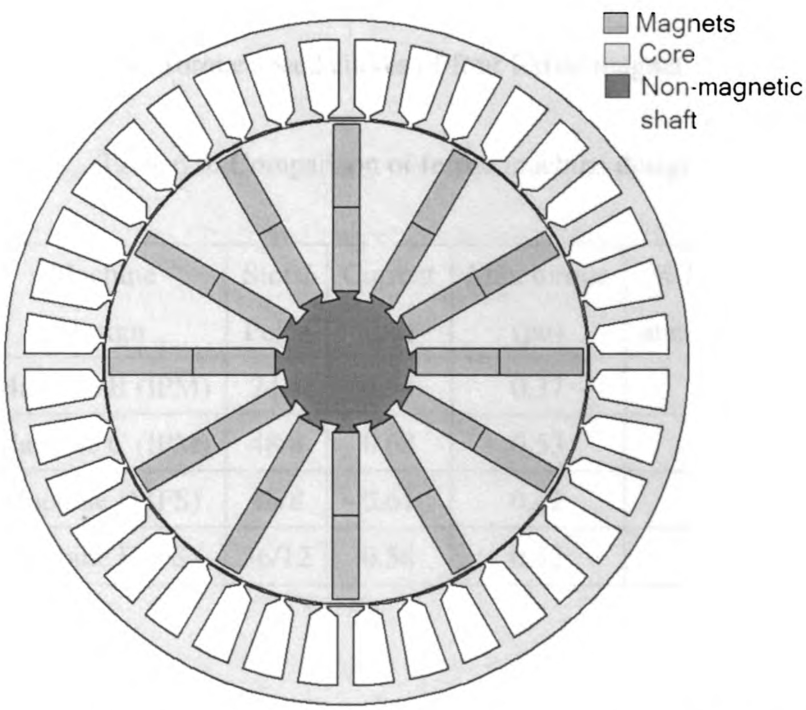

Figure 6.13: 12 pole flux squeeze machine using ferrite magnets (Machine E)

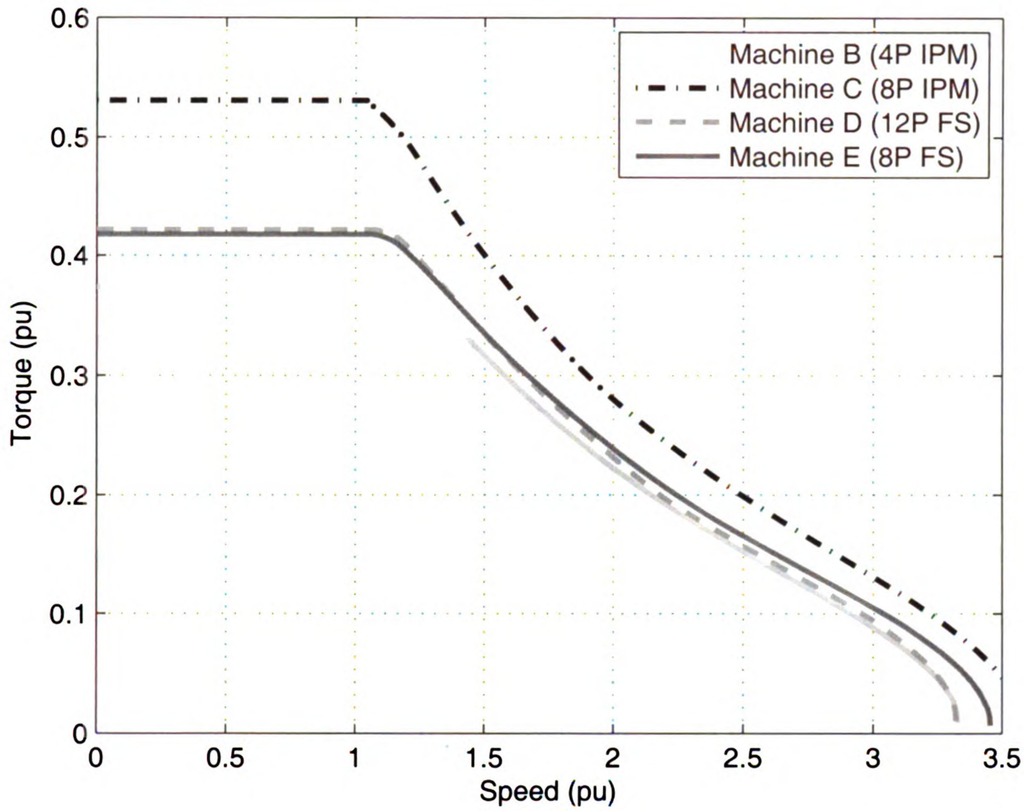

Figure 6.14: Torque speed curves of four ferrite magnet machines

Table 6.5: Comparison of ferrite machine designs

Machine Design	Slots/ Poles	Current (pu)	Max torque (pu)	% Efficiency at corner point
Machine B (IPM)	24/4	0.54	0.37	97.2
Machine C (IPM)	48/8	0.68	0.53	97.3
Machine D (FS)	48/8	0.61	0.42	97.1
Machine E (FS)	36/12	0.58	0.42	96.7

1. Replacing rare earth magnets by ferrite, we get only 37% of the baseline machine torque.

2. Number of poles are increased to get more air gap flux. This increases the power frequency of the stator current for the same shaft speed as that of baseline machine, thus increasing the iron losses of the machine.

3. Back emf of flux squeeze design is closer to square wave as compared to the IPM design, producing more harmonic iron losses.

4. The output power from 8 pole and 12 pole flux squeeze design is almost the same (42%), however, they differ in the efficiency due to different harmonics in the flux density. 12 pole machine has more contents of high frequency harmonics.

5. An 8 pole IPM machine is more suitable design for ferrite magnets because it can provide maximum power density (53% of the baseline machine power) among other design options and shows maximum efficiency as well.

6.7 Conclusions

Design and analysis of 140 kW IPMSM is presented for a series hybrid bus application for high temperature application using NdFeB and SmCo magnets. Reduced flux density of permanent magnets was taken into account with temperature increase. A 4-pole NdFeB baseline machine shows efficient and wide speed range operation. SmCo magnets are alternate of NdFeB for high temperature operation of the machine. However, the machine efficiency is reduced when NdFeB magnets are replaced by SmCo. An improvement in the torque and efficiency was achieved when machine rotor is redesigned for SmCo magnets but still machine efficiency remains less than that of the NdFeB machine. Beyond 200°, SmCo magnets are the only option for high power density machines.

The design of high power PMSMs is also explored without using rare earth magnets. In that case, ferrite magnets could be the only choice that can work for high temperature as well. IPM and flux squeeze designs were tried with increased number of poles. Among ferrite magnet designs, 8 pole IPM design provided the maximum power density, which is 53% of that of the baseline NdFeB machine.

Chapter 7

Iron and Magnet Losses and Torque Calculation using Magnetic Equivalent Circuit

7.1 Introduction

A faster and simpler approach for the calculation of iron and magnet losses and torque of an Interior Permanent Magnet Synchronous Machine (IPMSM) than Finite Element Methods (FEM) is presented here. It uses Magnetic Equivalent Circuit (MEC) based on lumped large elements and takes into account magnetic saturation and magnet eddy currents. The machine is represented by non-linear and constant reluctance elements and flux sources. Solution of the non-linear magnetic circuit is obtained by an iterative method. The results allow the calculation of losses and torque of the machine. Due to the approximations used in the formulation of the MEC, this method is less accurate but faster than non-linear transient magnetic FEM, and is more useful for the comparison of different machine designs during design optimization.

This approach for modeling of MEC starts with that in [40] and adds a number of improvements and adaptations. A simple 2-D MEC model of a radial flux IPMSM based on the limited and large iron core elements is used that works well for no load as well as for varying load conditions. The B-H curve of the iron core material was modeled using cubic splines. The iron core and air gap were divided into saturating and non-saturating elements respectively. The winding current and magnets were represented by mmf and flux source. Re-meshing of air gap elements with stator and rotor elements nodes was performed at every time step. Time dependent solution of the flux led to the calculation of iron and magnet losses and torque of the machine.

Reduced accuracy due to the use of large core elements is compensated for in ways that avoid increasing the element count and prolonging solution: data points of B-H curve are used instead of an approximated analytical function, considerations are developed that lead to a careful design of elements and element sizes, and a new type of element is proposed that has two possible axes of flux for areas where the direction of flux varies in the time domain.

An overview earlier work on this topic was presented in [41]. Further details were presented in [42]. Here, the MEC method is discussed in detail, including the considerations for the creation of elements, improvement in the iron losses algorithm, and torque calculation. Magsoft's Flux 2D, a commercial software package has been used as FEM tool. Solution of MEC and losses calculation is worked out using Matlab®. Although, the proposed method requires the geometrical dimensions of all elements of the MEC, however, most elements of the IPMSMs are symmetrical. The programming effort for each design iteration is primarily to enter the dimensions of only a few elements in the Matlab program. Each machine presented in this paper took about 10-15 minutes for this task.

The literature review of the various methods for calculation of machine losses and MEC is discussed in section 7.2. The overview of MEC approach for IPMSMs is presented in section 7.3. Considerations for the creation of elements are described in section 7.4. Development of mathematical model of MEC for a typical IPMSM and its solution is discussed in section 7.5. Calculation of the iron and magnet losses are explained next in section 7.6. Application of the MEC method to two different machines, calculation of torque, and comparison with FEM results are presented in section 7.7. Finally, conclusions in section 7.8, give a summary and discuss potential utilization of the proposed method.

7.2 Literature Review

Analytical methods presented by Mi *et al.* [43] and Roshen [44] cover stator iron losses for Permanent Magnet (PM) machines. Dlala [45] proposed a calculation method based on the modeling of the BH curve and the magnetic properties of the lamination material. Roshen presented an accurate method of core losses calculation for AC machines that addresses non- sinusoidal waveforms as well [46], [47]. The method is based upon a piece-wise linear modeling of the flux density in the time domain.

FEM is generally used to calculate iron losses with better accuracy. Computation of iron losses components for PMSMs was given by Yamazaki and Seto [48] with improvements proposed by Seo *et al.* [49] using variable iron loss coefficients. A dynamic loss model of the lamination material is presented by Belahcen and Arkkio in [50] to calculate the iron losses of electrical machines using FEM.

A widely used fast analytical machine design software tool (SPEED) includes a module that provides rapid sizing and calculates the performance characteristics of PM machines based upon linear characteristics of the material [34]. Calculation of the iron losses under magnetic saturation is handled by interfacing of SPEED with FEM [51].

MEC is also known as Reluctance Network Analysis (RNA), and its application for electrical machines were introduced by Ostović [40]. Improvements were made in MEC /RNA to estimate the performance of electromagnetic devices and electrical machines [52, 53, 54, 55, 56, 57, 58, 59, 60]. Performance analysis using MEC is receiving more attention, especially during the early design optimization. Its key advantages are the higher accuracy than the analytical and lumped parameter models and lower computational time than the FEM.

The majority of the work based on MEC addresses induction and switched reluctance machines and electromagnetic actuators [52, 53, 54, 55, 56, 57, 58, 59, 60]. Kim *et al.* [52] calculated the static characteristics of a linear brushless DC machine using MEC, neglecting the reluctance of the iron core. RNA based iron loss calculation of a switched reluctance motor in [53] utilized an analytical function to approximate the B-H curve of the iron core. Perho presented RNA based performance analysis of an induction machine using a BH curve approximated by a third order function [54]. MEC was also used to model a voltage fed induction machine [55] in the dq frame of reference for different operating conditions. Derbas *et al.* [60] compared mesh-based to node-based analysis of nonlinear magnetic circuits.

To improve the accuracy of the MEC/RNA and to capture the effects of saturation, leakage and fringing of the flux, refinement of the elements was used. The switched reluctance machine was studied in [56], and an electromagnetic actuator in [57]. 3-D MEC was introduced in [58], [59], and encouraging results were obtained for an induction machine. Increasing the number of elements and using 3-D networks for MEC provides better accuracy, and development of MEC in this direction may replace the need of FEM. However, MEC will loose its key advantage of faster calculation due to increased size of the system of equations [54].

A lumped parameter model for flux switching PM machine by Zhu et al. [61] was used to calculate back EMF, stator inductance and developed torque. A comparison between lumped parameters and FEM for the calculation of d and q axes inductances in PM machines was discussed in [62]. More detailed work was presented in [63] for the calculation of d and q axes inductances and torque for saturated IPMSM. Recent work on IPMSM by Zhu *et al.* [64] shows good match of fundamental air gap flux density compared with that of FEM for no load, neglecting the reluctance of stator and rotor iron, and using fixed sat-

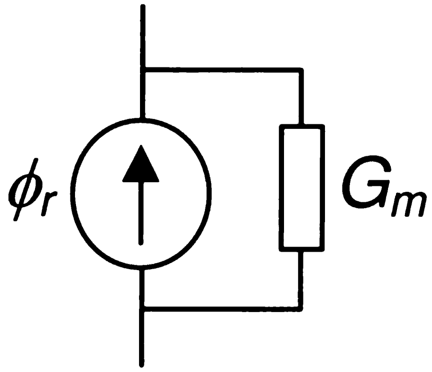

Figure 7.1: MEC circuit model of a permanent magnet

uration level in the bridges. Analysis at a varying load will need further refinement of the elements due to saturation of the iron core.

7.3 MEC Approach

The first task of MEC is to divide the machine geometry into enough elements to reflect all its electromagnetic properties. The number of elements should allow the solutions of the MEC with reasonable accuracy in time significantly lower than FEM.

An IPMSM is made of iron core, permanent magnets, air gap, and current carrying windings. Permanent magnet elements have constant permeance, since their relative permeability is almost equal to that of the air. Each permanent magnet is represented by a flux source and a parallel non-saturating reluctance, as shown in Fig. 7.1[40].

Flux of this source is $\phi_r = B_r A_m$ and its parallel permeance is $G_m = \dfrac{B_r A_m}{H_c l_m}$, where H_c and B_r are coercivity and remanent flux density of the permanent magnet. l_m is the length of the magnet in the direction of flux through it, and A_m is its area perpendicular to the flux direction.

Similarly, current carrying stator windings are modeled by time varying magnetomotive force (mmf). The mmf for each stator tooth is calculated from the winding configuration, number of turns and the stator current. With time varying current, the mmf of each stator tooth varies at each time step.

The iron core and air gap are divided into rectangular elements. The permeance of a uniform material is given by:

$$G = \frac{\mu_0 \mu_r A}{l} \tag{7.1}$$

where A, l are area and length of the elements, and μ_0, μ_r are the absolute and relative permeability.

In order to determine the length and area of each element, the expected flux direction and its variation are established first. One side of every element is along the axial direction and it is equal to the stack length of the machine. Other side of the area is the element width. The length of each element is taken along the flux direction.

Due to the magnetic saturation, μ_r varies widely and it is recalculated for all saturated elements at each iteration of every time step. The geometry of air gap elements and their interface with stator and rotor elements also varies at each time step due to machine rotation.

7.4 Formation of Elements

The machine geometry is divided into large elements so that the magnetic flux can be approximately uniform in each element at any instant. The geometry of elements, with the exception of those in the air gap, is invariable. Stator teeth and back iron elements are symmetric. Rotational symmetry is also used to minimize the number of elements.

7.4.1 Stator elements

The stator elements for one quarter of a 3 phase, 4 pole, 24 slot, 20 kW, IPMSM are shown in Fig. 7.2. Each tooth is taken as one element, and its length is equal to the depth of the

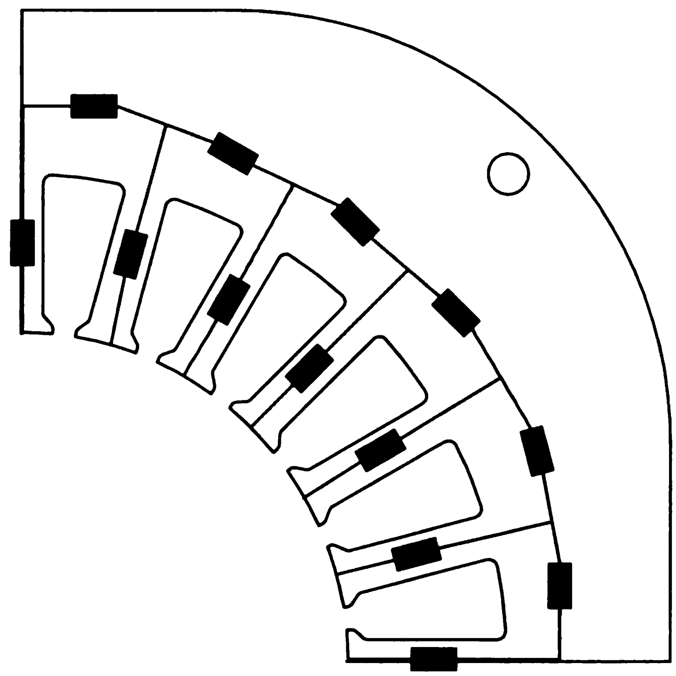

(a) Elements

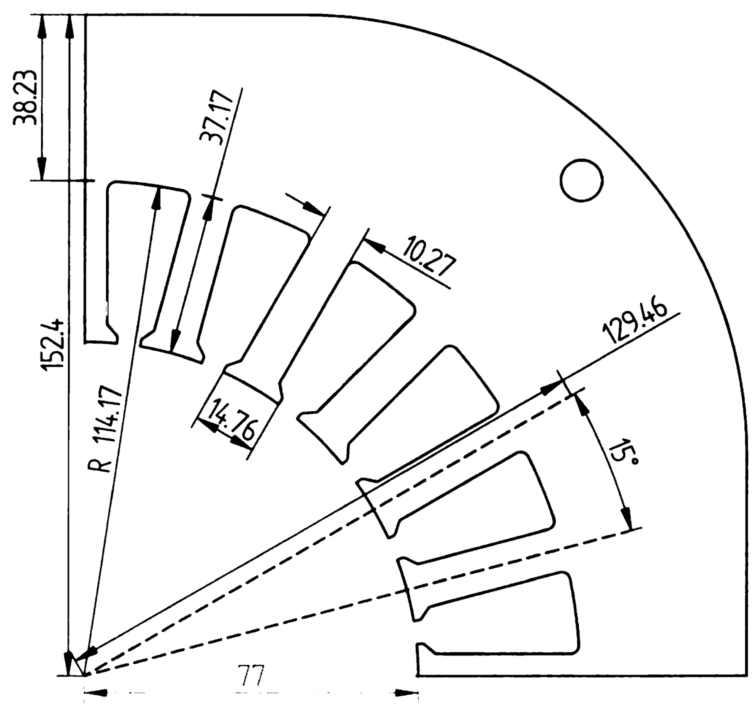

(b) Geometry

Figure 7.2: Large elements of quarter geometry of stator

slot. The flux direction in every stator tooth remains along its length, radial to the axis of rotation. Since the width of stator teeth is not uniform along its length, it is taken as the weighted average of the teeth segments.

A back iron element is created between every two adjacent teeth. The width of each element is the difference of the outer and the inner radius of the yoke. Its length is the weighted average of minimum and maximum arc distances in the yoke, which correspond to the inner and outer yoke radii.

7.4.2 Rotor elements

The flux paths in the rotor are more complex than in the stator. The flux direction in the rotor elements varies significantly with the magnitude and phase of the load current as shown in Fig. 7.3, and this is reflected in the type and geometry of elements of Fig. 7.5 and 7.4 discussed in this section.

7.4.2.1 Permanent magnets

Each magnet is represented by a linear permeance in parallel with a flux source as that of Fig. 7.1. Air pockets between the magnets are also represented by linear permeance. Half of each air pocket permeance is added to the permeance of the magnet on its each side. This results in one permeance parallel to each flux source as shown by G_{m1}, G_{m2}, G_{m3}, G_{m4} and G_{m5}.

7.4.2.2 Bridges

Bridges are the narrow flux paths of iron core between two magnets, and between a magnet and rotor edge. Deeply saturated bridges (outer layer rotor edge) are represented by an equivalent air permeance G_{br1}. Bridges near rotor edge of inner magnet layer are not fully saturated and are treated as saturating permeance G_{13}. Similarly, the permeance between

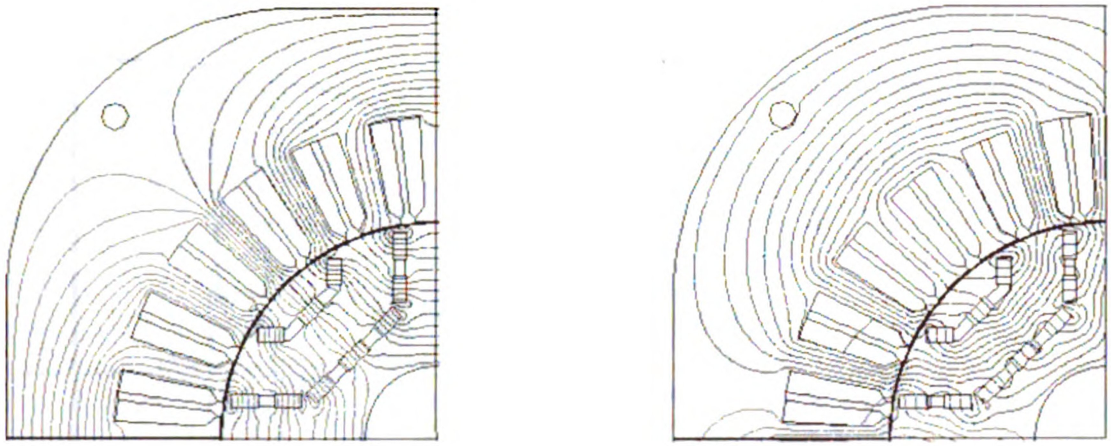

(a) No load (b) Full load

Figure 7.3: Flux lines of FEM representing the flux path in the rotor with load variation

the magnets are saturating too, and they are split into two G_{14}, each half is in parallel with the magnet on its side.

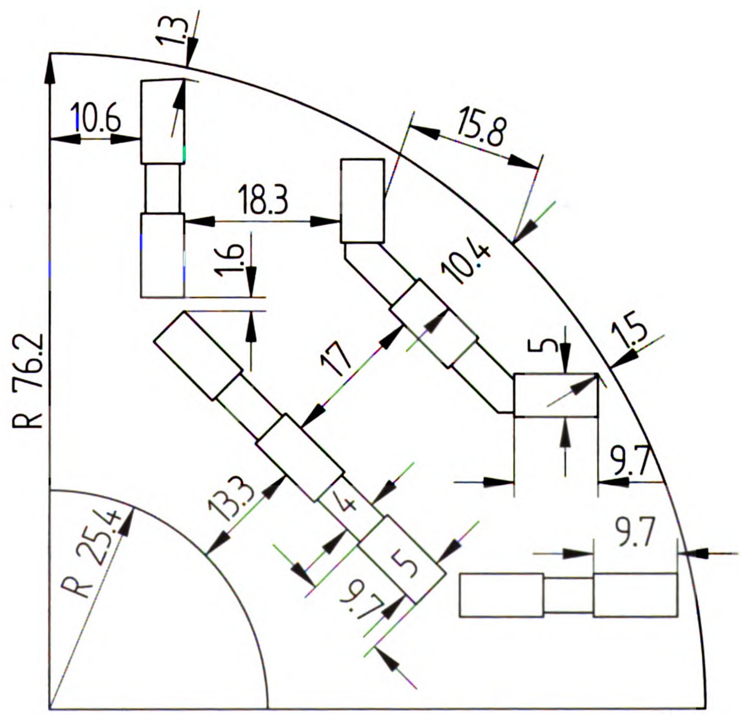

Figure 7.4: Geometry of quarter rotor

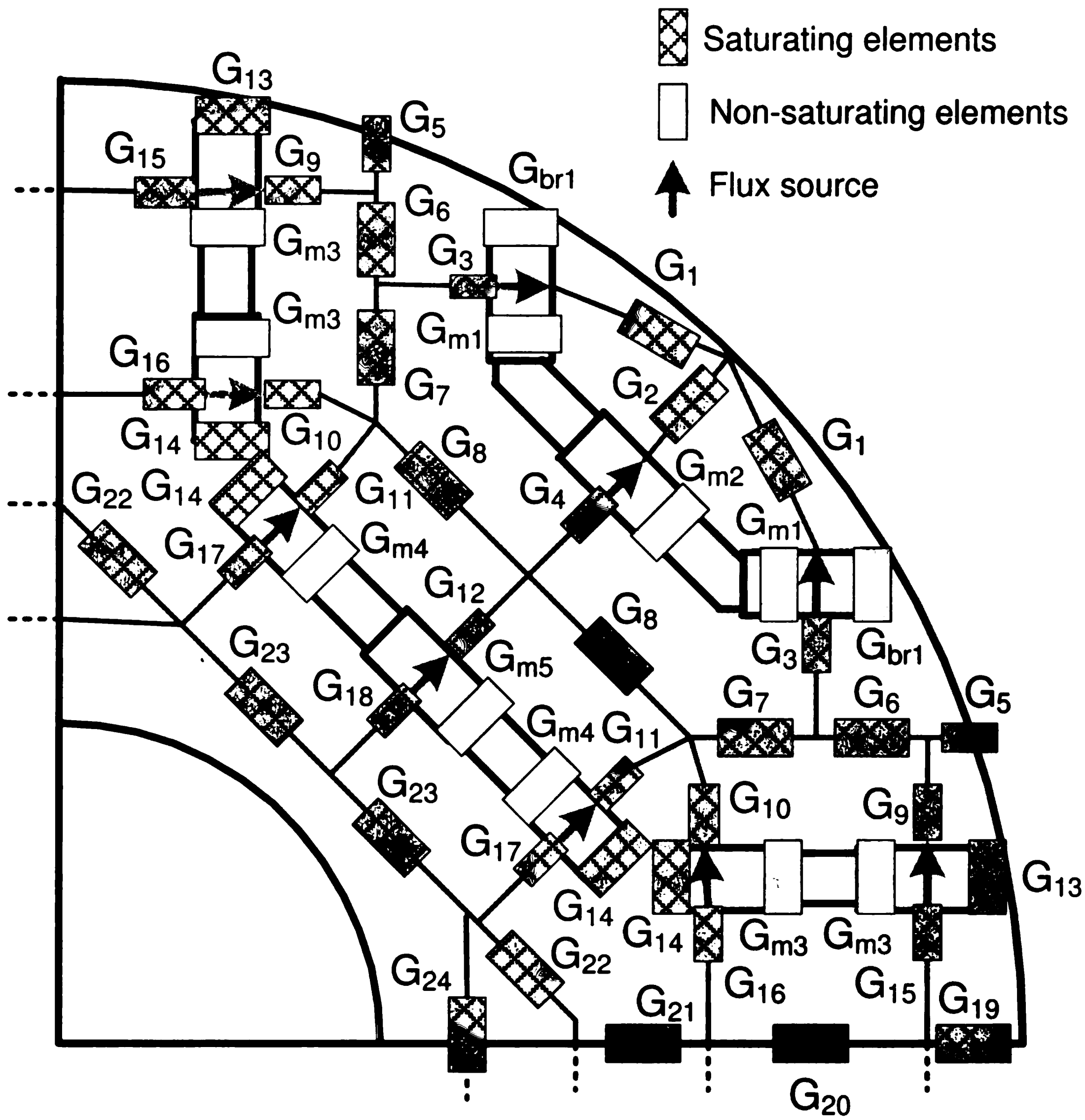

Figure 7.5: Elements of quarter rotor

7.4.2.3 Rotor iron between outer magnet layer and air gap

In this area of core, there is varying flux direction due to varying rotor position and load current, but much less than the other rotor elements. The flux direction in this part is modeled as perpendicular to the magnet thickness in G_1 and G_2 elements. The width of each of these elements is equal to one third of the total arc length of the rotor surface in front of the outer magnet layer. These three permeances have a common node on the rotor surface.

7.4.2.4 Rotor iron between magnet layers and around shaft

This part of rotor has flux direction that varies from the perpendicular to tangent to the magnet surface. To include this effect, the iron core of rotor is 'counted' twice in the formulation of elements. The first time it is assumed that the flux path is along one direction, i.e. perpendicular to the magnet thickness. Here the iron core is divided into elements G_3, G_4, G_9, G_{10}, G_{11}, G_{12}, G_{15}, G_{16}, G_{17} and G_{18}. The second time the flux path is modeled as tangential to the magnet thickness. This results in the formation of elements G_5, G_6, G_7, G_8, G_{19}, G_{20}, G_{21}, G_{22} and G_{23}. Applying this approach, the dimensions of all rotor elements are calculated and are listed in Table 7.1.

7.4.2.5 Air gap

Air gap between stator and rotor is modeled as rectangular linear elements. Each element length is equal to that of the air gap. Their width is the air gap arc of the overlapping angle of stator and rotor elements, and it varies at every time step due to machine rotation. Between non-overlapping stator teeth and rotor elements, the air gap permeance is zero.

7.5 MEC of IPMSM

The MEC model of one pole pair is shown in Fig. 7.6. The physical connection between the left and right ends of the magnetic circuit is modeled through common variables. To simplify the MEC, two permeance elements in series with each flux source are combined to one element. A linear leakage permeance exists between every two stator teeth due to stator slot opening. The mmf source of the stator teeth depends on the winding configuration, coil pitch, number of turns, and input current [40].

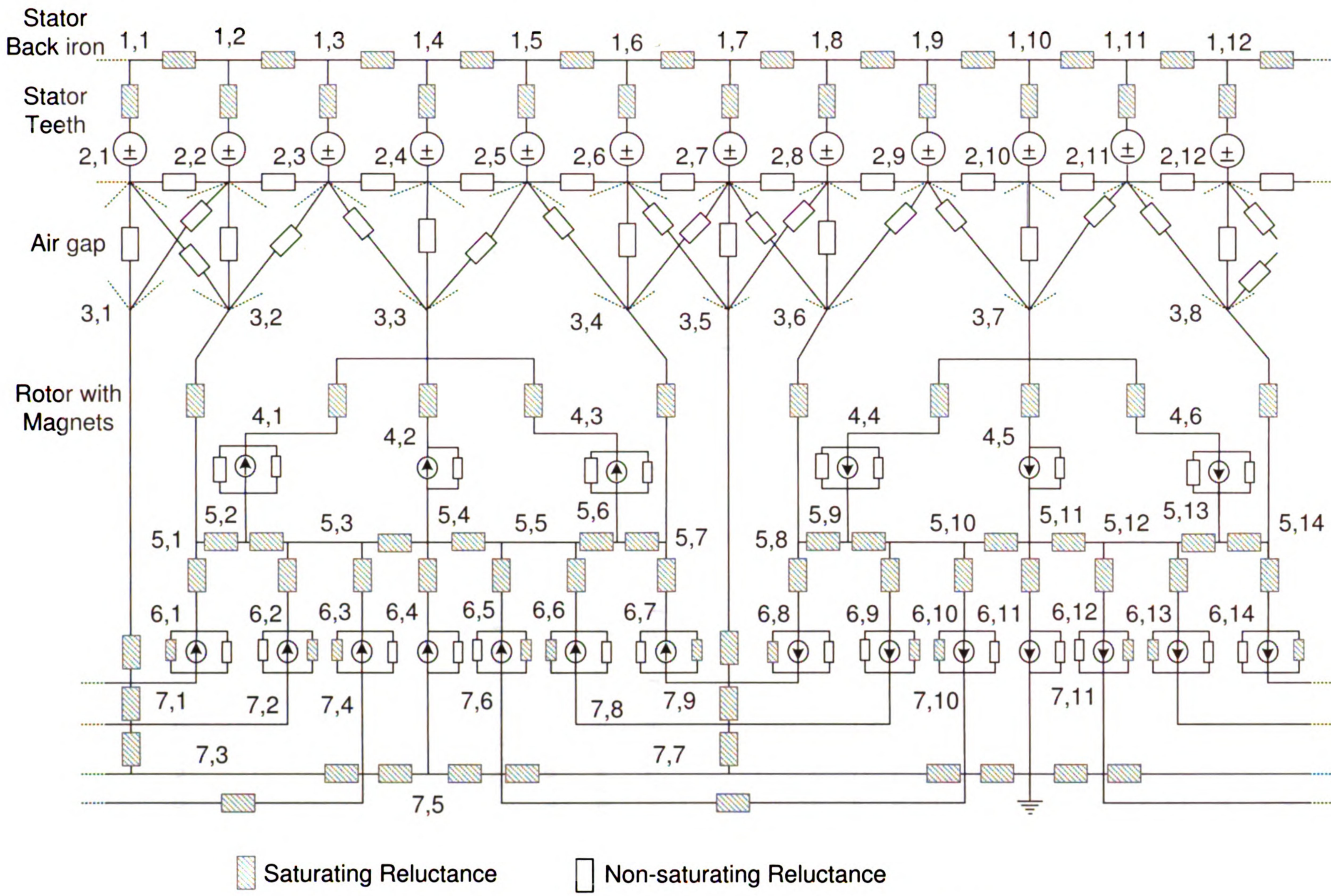

Figure 7.6: Magnetic equivalent circuit of a pole pair of an IPMSM

Table 7.1: Length and width of the rotor elements

Element #	Length (mm)	Width (mm)	Element #	Length (mm)	Width (mm)
G_3	9.15	16.26	G_{14}	4.00	1.00
G_4	8.52	27.15	G_{15}	10.63	12.60
G_5	4.02	18.79	G_{16}	10.63	12.60
G_6	9.19	18.29	G_{17}	13.32	13.24
G_7	9.03	18.29	G_{18}	13.32	16.78
G_8	18.15	17.04	G_{19}	8.07	21.25
G_9	9.15	12.60	G_{20}	15.50	21.25
G_{10}	9.15	12.60	G_{21}	9.96	21.25
G_{11}	8.52	13.24	G_{22}	13.53	13.32
G_{12}	8.52	16.78	G_{23}	16.78	13.32
G_{13}	5.00	2.05	G_{24}	6.10	5.63

7.5.1 Derivation of MEC

In order to calculate the flux through each reluctance of Fig. 7.6, the magnetic scalar potential at every node i, j is defined. Vector notation is used to write the system of equations containing the magnetic circuit variables and parameters. Followings are the vectors of unknown magnetic scalar potential of the nodes of different sections of Fig. 7.6.

$\vec{u_1}$ Stator back iron.

$\vec{u_2}$ Stator teeth.

$\vec{u_3}$ Rotor surface.

$\vec{u_4}$, $\vec{u_5}$, $\vec{u_6}$ and $\vec{u_7}$ Interior rotor.

Similarly, the following machine parameters are also used in the development of MEC.

$\vec{\mathcal{F}_{st}}$ Stator teeth mmf vector.

$\vec{\phi_{st}}$ Stator teeth flux vector.

$\mathcal{R}_{st}$ Stator teeth reluctances diagonal matrix.

The reluctance of an element in the circuit is represented by $\mathcal{R}_{xy}$, and $G_{xy} = 1/\mathcal{R}_{xy}$ denotes the corresponding permeance of the same element.

Taking one rotor node as reference, we write a set of equations for all nodes. For a stator back iron node 1 (u_{11}) of Fig. 7.6, G_{sy1} and G_{sy12} are the permeances of the element between nodes 1 and 2 and nodes 1 and 12 respectively, ϕ_{st1} is the flux in the stator tooth 1 from stator back iron towards the air gap. Then:

$$\left(u_{1,1} - u_{1,12}\right)\ G_{sy12} + \left(u_{1,1} - u_{1,2}\right)\ G_{sy1} = -\phi_{st1} \tag{7.2}$$

Similarly at node 2:

$$\left(u_{1,2} - u_{1,1}\right)\ G_{sy1} + \left(u_{1,2} - u_{1,3}\right)\ G_{sy2} = -\phi_{st2} \tag{7.3}$$

and at the last node of stator back iron:

$$\left(u_{1,12} - u_{1,11}\right)\ G_{sy11} + \left(u_{1,12} - u_{1,1}\right)\ G_{sy12} = -\phi_{st12} \tag{7.4}$$

In matrix form,

$$\mathbf{A}_{11}\vec{u_1} = -\vec{\phi_{st}} \tag{7.5}$$

Where

$$\mathbf{A}_{11} = \begin{bmatrix} G_{sy12} + G_{sy1} & -G_{sy1} & \cdots & -G_{sy12} \\ -G_{sy1} & G_{sy1} + G_{sy2} & \cdots & 0 \\ \vdots & \vdots & \ddots & \vdots \\ -G_{sy12} & 0 & \cdots & G_{sy11} + G_{sy12} \end{bmatrix}$$

For all nodes of the magnetic circuit of Fig. 7.6:

$$
\begin{aligned}
&\mathbf{A}_{11}\vec{u}_1 = -\vec{\phi}_{st} \\
&\mathbf{A}_{22}\vec{u}_2 + \mathbf{A}_{23}\vec{u}_3 = \vec{\phi}_{st} \\
&\mathbf{A}_{32}\vec{u}_2 + \mathbf{A}_{33}\vec{u}_3 + \mathbf{A}_{34}\vec{u}_4 + \mathbf{A}_{35}\vec{u}_5 + \mathbf{A}_{37}\vec{u}_7 = 0 \\
&\mathbf{A}_{43}\vec{u}_3 + \mathbf{A}_{44}\vec{u}_4 + \mathbf{A}_{45}\vec{u}_5 = \vec{\phi}_{m4} \\
&\mathbf{A}_{53}\vec{u}_3 + \mathbf{A}_{54}\vec{u}_4 + \mathbf{A}_{55}\vec{u}_5 + \mathbf{A}_{56}\vec{u}_6 = \vec{\phi}_{m5} \\
&\mathbf{A}_{65}\vec{u}_5 + \mathbf{A}_{66}\vec{u}_6 + \mathbf{A}_{67}\vec{u}_7 = \vec{\phi}_{m6} \\
&\mathbf{A}_{73}\vec{u}_3 + \mathbf{A}_{76}\vec{u}_6 + \mathbf{A}_{77}\vec{u}_7 = \vec{\phi}_{m7}
\end{aligned}
\tag{7.6}
$$

Here $\vec{\phi}_{m4}$, $\vec{\phi}_{m5}$, $\vec{\phi}_{m6}$ and $\vec{\phi}_{m7}$ are the vectors of flux sources of permanent magnets at the respective nodes.

In matrix form,

$$\mathbf{A}\vec{u} = \vec{\phi} \tag{7.7}$$

Where

$$
\mathbf{A} = \begin{bmatrix}
\mathbf{A}_{11} & 0 & 0 & 0 & 0 & 0 & 0 \\
0 & \mathbf{A}_{22} & \mathbf{A}_{23} & 0 & 0 & 0 & 0 \\
0 & \mathbf{A}_{32} & \mathbf{A}_{33} & \mathbf{A}_{34} & \mathbf{A}_{35} & 0 & \mathbf{A}_{37} \\
0 & 0 & \mathbf{A}_{43} & \mathbf{A}_{44} & \mathbf{A}_{45} & 0 & 0 \\
0 & 0 & \mathbf{A}_{53} & \mathbf{A}_{54} & \mathbf{A}_{55} & \mathbf{A}_{56} & 0 \\
0 & 0 & 0 & 0 & \mathbf{A}_{65} & \mathbf{A}_{66} & \mathbf{A}_{67} \\
0 & 0 & \mathbf{A}_{73} & 0 & 0 & \mathbf{A}_{76} & \mathbf{A}_{77}
\end{bmatrix}
$$

$$\vec{u} = [\ \vec{u}_1 \quad \vec{u}_2 \quad \vec{u}_3 \quad \vec{u}_4 \quad \vec{u}_5 \quad \vec{u}_6 \quad \vec{u}_7\ ]^T$$

$$\vec{\phi} = [\ -\vec{\phi}_{st} \quad \vec{\phi}_{st} \quad 0 \quad \vec{\phi}_{m4} \quad \vec{\phi}_{m5} \quad \vec{\phi}_{m6} \quad \vec{\phi}_{m7}\ ]^T$$

$\mathbf{A}_{ij}$ are the permeance matrices of the magnetic circuit.

Magnetic scalar potential of the stator back iron and stator teeth nodes is related to the teeth *mmf* by:

$$\vec{u_1} = \vec{u_2} + \vec{\mathcal{F}_{st}} + \mathcal{R}_{st}\vec{\phi_{st}} \tag{7.8}$$

In system (7.7), the unknown variables are the scalar magnetic potential of the nodes ($\vec{u_1}$, $\vec{u_2}$, $\vec{u_3}$, $\vec{u_4}$, $\vec{u_5}$, $\vec{u_6}$ and $\vec{u_7}$) and the flux through the stator teeth ($\vec{\phi_{st}}$). Using (7.8), we solve system (7.7) to eliminate $\vec{\phi_{st}}$ and $\vec{u_1}$. This leads to the following reduced system of equations for the magnetic equivalent circuit of the IPMSM:

$$\widehat{\mathbf{A}}\hat{\vec{u}} = \hat{\vec{\phi}} \tag{7.9}$$

where

$$\widehat{\mathbf{A}} = \begin{bmatrix} \mathbf{X}_1 & \mathbf{X}_2 & 0 & 0 & 0 & 0 \\ \mathbf{A}_{32} & \mathbf{A}_{33} & \mathbf{A}_{34} & \mathbf{A}_{35} & 0 & \mathbf{A}_{37} \\ 0 & \mathbf{A}_{43} & \mathbf{A}_{44} & \mathbf{A}_{45} & 0 & 0 \\ 0 & \mathbf{A}_{53} & \mathbf{A}_{54} & \mathbf{A}_{55} & \mathbf{A}_{56} & 0 \\ 0 & 0 & 0 & \mathbf{A}_{65} & \mathbf{A}_{66} & \mathbf{A}_{67} \\ 0 & \mathbf{A}_{73} & 0 & 0 & \mathbf{A}_{76} & \mathbf{A}_{77} \end{bmatrix}$$

and

$$\mathbf{X}_1 = \mathbf{A}_{11} + (\mathbf{I} + \mathbf{A}_{11}\mathcal{R}_{st})\mathbf{A}_{22}$$

$$\mathbf{X}_2 = (\mathbf{I} + \mathbf{A}_{11}\mathcal{R}_{st})\mathbf{A}_{23}$$

$$\hat{\vec{u}} = [\ \vec{u_2}\ \ \vec{u_3}\ \ \vec{u_4}\ \ \vec{u_5}\ \ \vec{u_6}\ \ \vec{u_7}\ ]^T$$

$$\hat{\vec{\phi}} = [\ -\mathbf{A}_{11}\mathcal{F}_{st}\ \ 0\ \ \vec{\phi_{m4}}\ \ \vec{\phi_{m5}}\ \ \vec{\phi_{m6}}\ \ \vec{\phi_{m7}}\ ]^T$$

7.5.2 Solution of MEC

In order to calculate the flux through each element of Fig. 7.6, the Magnetic Scalar Potential (MSP) of each node was computed first. For this purpose, the non-linear system (7.9) was solved iteratively for every time step using Successive Over Relaxation (SOR) method [65]. The calculation of $\vec{u_1}$ was worked out from (7.8) and the first equation of system(7.7), and it resulted into (7.10):

$$u_1 = (I + R_{st}A_{11})^{-1}(u_2 + \mathcal{F}_{st}) \tag{7.10}$$

The solution was obtained for half the cycle of the input current due to current symmetry. The stator nodes position was fixed, however, the rotor surface nodes were moving due to machine rotation, and their position was tracked in the solution of MEC. The overlap angle between stator and rotor nodes varied at each time step, and this affected the reluctance and connections of the air gap elements. Linear reluctance elements (other than in the air gap) were calculated only once, while the air gap reluctance was computed for every time step. The relative permeability of saturated elements was adjusted in every iteration. A cubic spline interpolation was used to represent the curve from discrete BH data points and flux density was calculated from the MSP of the nodes. The magnetic flux and flux density in each element was calculated from the MSP of the nodes and the respective area of the elements.

7.6 Calculation of Iron and Magnetic Losses

7.6.1 Iron losses

The iron losses were calculated by post processing of the MSP of the nodes of MEC. The iron losses are divided into three categories:

1. Hysteresis losses

$$W_h = K_h K_f B_m^2 f \tag{7.11}$$

2. Eddy current losses

$$W_e = \frac{1}{T} \int_0^T K_f \sigma \frac{d^2}{12} \left(\frac{dB}{dt}\right)^2 dt \tag{7.12}$$

3. Excess losses

$$W_{ex} = \frac{1}{T} \int_0^T K_e K_f \left(\frac{dB}{dt}\right)^{1.5} dt \tag{7.13}$$

where

k_h = Coefficient of hysteresis losses $(W/T^2 s^{-1} m^3)$

k_e = Coefficient of excess losses $(W/(T s^{-1})^{3/2} m^3)$

σ = Conductivity of laminations $(\Omega m)^{-1}$

d = Thickness of laminations (m)

k_f = Fill factor of laminations (0–1)

f = Frequency of stator current (Hz)

B_m= Maximum flux density (T)

Here, f is known for the stator and it is zero for the rotor. B was calculated from MSP for each element at each time step, σ and d were readily available from the manufacturer's information of laminations. and K_f was calculated from lamination thickness and stack length of the machine. The iron losses coefficients (K_h and K_e) were computed from the loss data of the laminations steel as described in section 3.4.2.

7.6.2 Losses in the permanent magnets

In magnets, for operation on the recoil line, hysteresis losses are not significant, nor are excess losses. The eddy current losses in the permanent magnets were calculated by considering the eddy current paths there as shown in Fig. 7.7 [66]. Considering L, T and W as length, thickness and width of the magnet respectively; B is flux density and $A = LW$ is magnet area perpendicular to the flux. The time varying flux in the magnet induces EMF (V), and hence the eddy currents. The magnet length is along the axis of machine stack. EMF (V) is induced in each side of the magnet along its length, causing eddy currents to flow. The eddy loop has $2V$ voltage source due to two voltage sources in series.

$$2V = \frac{d\phi}{dt} = \frac{d(BA)}{dt} \quad \Rightarrow \quad V = \frac{A}{2}\frac{dB}{dt} \tag{7.14}$$

Representing the flux density in Fourier series,

$$\begin{aligned} V &= \frac{A}{2}\frac{d}{dt}\sum_{n=1}^{\infty}\left(C_n \cos(n\omega t) - \theta_n\right) \\ &= \frac{A\omega}{2}\sum_{n=1}^{\infty}\left(-nC_n \sin(n\omega t)\right) \end{aligned} \tag{7.15}$$

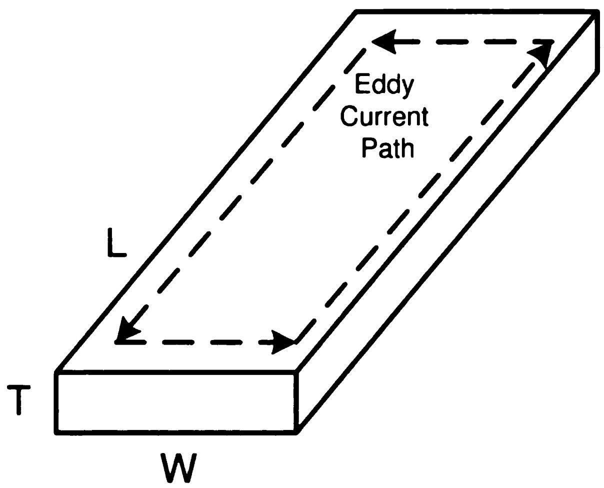

Figure 7.7: Eddy current flow in the magnets

The current in the magnets will be V_{rms}/R_{path}, and the V_{rms} is calculated as:

$$\begin{aligned} V_{rms} &= \sqrt{\frac{1}{2\pi}\int_0^{2\pi} V^2 d\omega t} \\ &= \sqrt{\frac{A^2\omega^2}{4}\frac{1}{2\pi}\int_0^{2\pi}\sum_{n=1}^{\infty}\left(n^2C_n^2\sin^2 n\omega t\right) d\omega t} \\ &= \frac{A\omega}{2}\sqrt{\sum_{n=1}^{\infty}\frac{n^2C_n^2}{2}} \end{aligned} \tag{7.16}$$

Assuming that the magnets are much longer than wide, the major current path is along the length of magnet. The current path in each direction occupies half of the magnet. Then area of eddy current path is

$$A_{path} = \frac{TW}{2} \quad \Rightarrow \quad R_{path} = \rho\frac{4L}{TW} \tag{7.17}$$

ρ is the resistivity of the magnets. The current density in the magnets is:

$$J = \frac{I}{A} = \frac{V_{rms}}{R_{path}}\frac{1}{A_{path}} = \frac{V_{rms}}{2\rho L} = \frac{W\pi f}{2\rho}\sqrt{\sum_{n=1}^{\infty}\frac{n^2C_n^2}{2}} \tag{7.18}$$

Magnet eddy current power density distribution is given by:

$$P_e = \rho J^2 = \frac{W^2\pi^2 f^2}{4\rho}\sum_{n=1}^{\infty}\frac{n^2C_n^2}{2} \tag{7.19}$$

From MSP of all nodes of the MEC, the flux density in the magnets is calculated from the linear relationship of mmf and flux. Magnet losses at different loads are calculated using (7.19) and Fast Fourier Transform (FFT).

7.7 Application of the Proposed Method

7.7.1 Flux density in the stator teeth

The flux density calculated from MEC was compared to that computed using FEM. One pole in FEM had 4092 elements and 8138 nodes, whereas there are only 144 elements (88 saturating and 56 non-saturating) and 72 nodes in a pole pair of the machine for MEC. Fig. 7.8 and 7.9 show the comparison of space and time variation of the flux density at no load. Fig. 7.8 shows the flux density on an arc path in the stator teeth at an instant of time and Fig. 7.9 shows the time variation of the flux density in a stator tooth. Similar comparison is shown for rated machine current in Fig. 7.10 and 7.11. Flux density calculated by the

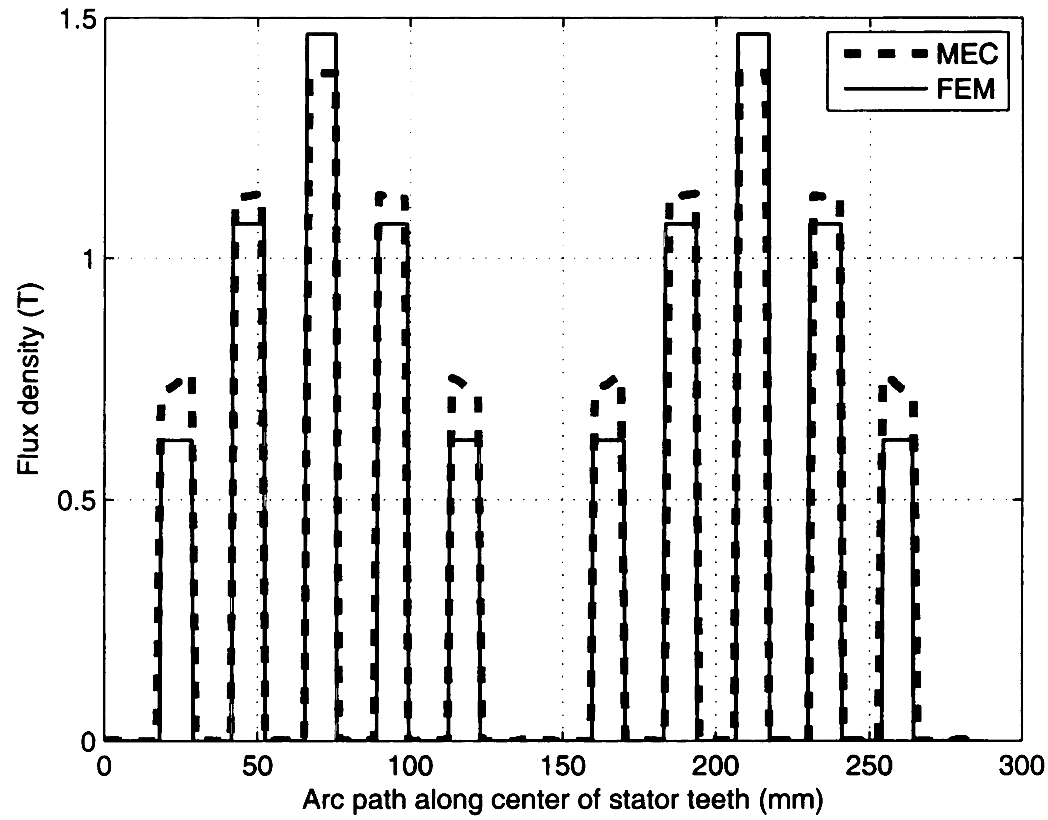

Figure 7.8: Space variation of flux density in stator teeth at no load

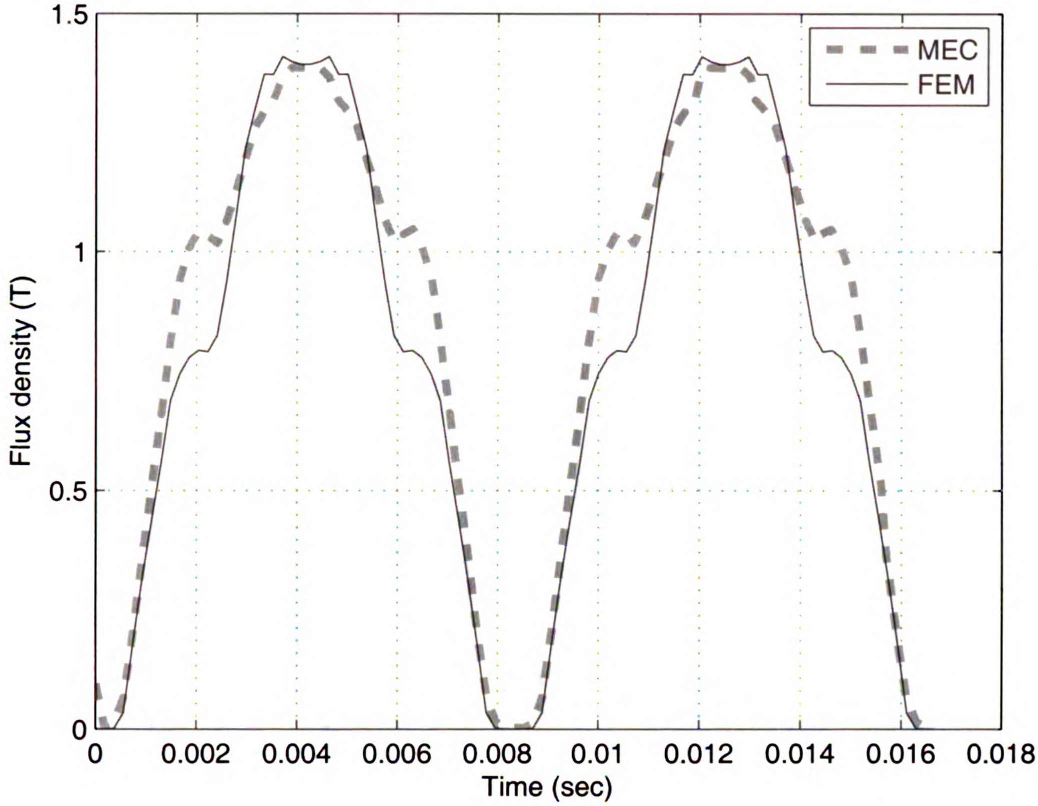

Figure 7.9: Time variation of flux density in a stator tooth at no load

proposed method in the stator teeth agrees with that computed by FEM.

7.7.2 Iron and magnet losses

The proposed method was used in two variations of a machine design to calculate iron and magnet losses. The baseline machine has the geometry of Fig. 7.2, 7.4 and 7.5, while the modified one has 1.5 times thicker magnets in its interior layer. All other parameters were the same. The results are compared to those of FEM in Table 7.2.

The losses were calculated at three different load current levels: no load, half load, and full load. MEC gives losses between 6-12% lower than those calculated by FEM at all load conditions, in both machines. Errors are in the same direction. Losses of the modified

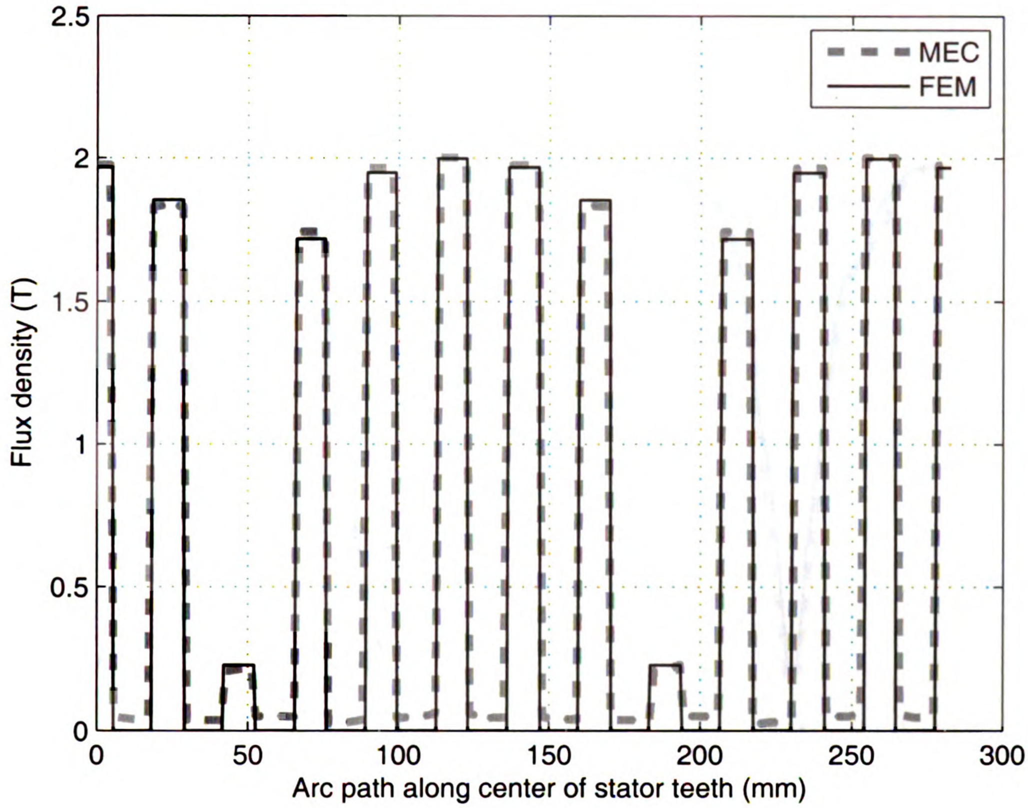

Figure 7.10: Space variation of flux density in stator teeth at full load

Table 7.2: Comparison of iron and magnet losses calculated using FEM and MEC

Machine Type	Load Current	FEM (W)	MEC (W)	% Error
Baseline Machine	0 %	68.2	60.7	-11.0 %
	50 %	146.5	138.3	-5.6 %
	100 %	212.3	194.6	-8.3%
Modified Machine	0 %	72.4	65.1	-10.1 %
	50 %	140.9	134.7	-4.4 %
	100 %	204.2	180.8	-11.4 %

machine calculated by FEM are higher at no load, and lower at half and full load than those of the baseline machine. This relation is similar to the results obtained from the proposed method using MEC model. An alternate and more accurate method to calculate the iron

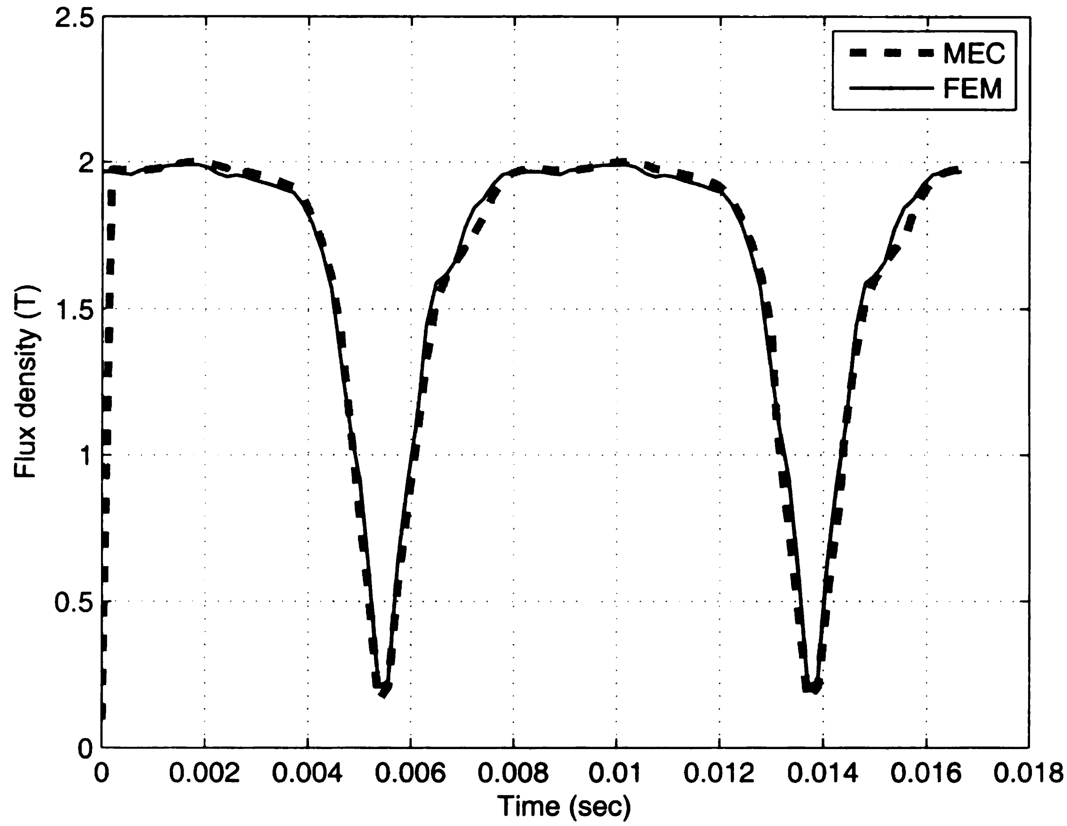

Figure 7.11: Time variation of flux density in a stator tooth at full load

and magnet losses from the flux density of each reluctance of the MEC using piece wise linear model is discussed in [46] and [47].

7.7.3 Developed torque

The developed torque of the machine was calculated by Arkkio's method, a variant of Maxwell Stress Tensor method [67, 68]. From the MSP at each node of the MEC, normal (B_n) and tangential (B_t) components of the flux density in the air gap were calculated for all stator and rotor overlapping elements at each time step. Arkkio's method uses (7.20) to calculate the instantaneous torque of the machine:

$$T = \frac{L}{\mu_0 (r_s - r_r)} \int\limits_S r_{ag} B_n B_t ds \tag{7.20}$$

where L is stack length of the machine, r_{ag} is the mean air gap radius and r_s, r_r are stator inner and rotor outer radius respectively, and the integration is over all elements of the air gap. Since there exists only one air gap element between every overlapping stator and rotor element. Therefore ds of (7.20) is expressed as $ds = (r_s - r_r) r_{ag} d\theta$, where θ is the overlapping angle between every stator and rotor elements. Then, (7.20) is written as:

$$T = \frac{L}{\mu_0} r_{ag}^2 \int\limits_0^{2\pi} B_n B_t d\theta \tag{7.21}$$

Table 7.3 compares average torque of the two machines discussed earlier in this section. The torque was calculated by FEM and MEC at rated current applied in the quadrature axis of the machine. The error is within 12% in the same direction as that of the losses in Table 7.2, which shows that torque calculation results are also consistent with those of iron and magnet losses. Losses and torque calculation took 195 s using the proposed method, whereas FEM spent about 3 hours.

Table 7.3: Torque comparison rated current calculated using FEM and MEC

Machine Type	FEM (Nm)	MEC (Nm)	% Error
Baseline Machine	26.1	24.4	-6.5 %
Modified Machine	28.8	25.5	-11.4 %

7.8 Conclusions

A numerical method based on a MEC model was developed for the calculation of iron and magnet losses and torque of IPMSMs. Starting from the basic geometry, winding configuration and input currents of the machine, a system of non-linear equations was derived and solved in the time domain for the MSP of the nodes. The system of equations is non-linear, and it was solved iteratively at each time step, using the BH data points of the iron core material. The flux density in each element was calculated from the MSP of the nodes, and this led to the calculation of the iron and magnet losses of the machine.

The results of the proposed method were compared to those obtained using FEM. The proposed method gave lower iron and magnet losses and torque than those calculated by FEM when it was applied to two different machines. Although this difference is significant, the results of the loss calculations for these designs show similar trends as those obtained using FEM. The proposed method requires much less time for calculation of iron losses and torque than FEM. Therefore this method can be useful for early sizing and efficiency comparison of several machine designs in reduced time. The MEC model of a machine can be developed easily from its geometry, thus shortening the total computation time. Furthermore, the dimensions of elements for each run can be generated automatically through parametrization.

Chapter 8

Summary and Future Work

The summary of the research tasks accomplished and their future research growth is given here:

8.1 Machine Design Based Upon ADCE

A design approach of IPMSM was presented for an HEV series bus for an urban driving cycle. The approach is based upon the maximization of average driving cycle efficiency. Inverter losses and power required for the machine and inverter cooling are also included in the calculation of ADCE to optimize the design of IPMSM. The applicability of this approach was demonstrated by two machine designs. During the calculation of machine efficiency by FEM, the machine current was assumed sinusoidal and therefore the losses due to PWM effects were not taken into account. Also the power required by the cooling effort was assumed as fixed percentage of the total machine and inverter losses. As a future extension of this work, a PWM model of inverter can be added in the calculation of machine losses. Furthermore, transient thermal analysis of the machine and inverter may also be included in the computation of ADCE to obtain more accurate results.

8.2 Overload Operating Conditions of IPMSM

The design and operation of an IPMSM has been explored for overload conditions using cross saturated dq model for more accurate machine parameters than obtained using conventional dq model.

Machine operation for higher than rated stator current can be achieved with increased cooling. Any specific design of IPMSM can operate safely up to power higher than rated, if such room is provided by the designer. Analysis of a baseline design of 105 kW IPMSM is presented for gradually increasing overload conditions. Demagnetization is shown to be the result not only of negative d-axis current, but also of the cross-saturation caused by the q-axis current component.

The IPMSM can be redesigned in more than one configurations to increase the operation range with increased cooling. Efficiency and torque speed range of various designs was studied. Among three design modifications in the rotor geometry, it was found that thicker magnets design allowed more overload operation with full speed range but with reduced efficiency as compared to the baseline design. As an alternate to increased machine cooling, use of SmCo magnets was also analyzed. Transient thermal analysis may be included in future work to remove the assumption of availability of sufficient cooling to keep the machine temperature within its specified limits.

8.3 Consideration of Different Magnet Materials for PM Machine Design

Design and analysis of two IPMSMs has been presented for a series hybrid bus application for high temperatures using NdFeB and SmCo magnets. Reduced flux density in the magnets was taken into account with temperature rise. The machine operation for a hybrid bus was analyzed at a low and a high end temperature. A 4-pole NdFeB baseline machine provides the efficient and wide speed range operation. SmCo magnets is the feasible option for higher temperature operation of the machine. However, the machine efficiency is reduced when NdFeB magnets are replaced by SmCo magnets. Redesigning of machine with SmCo magnets showed a little improvement.

The design of high power density machines was also investigated without using rare earth magnet materials considering the high temperature operation. Interior PM and flux squeeze design was explored using ferrite magnets with increased number of poles. Although ferrite magnets can operate at higher temperature than NdFeB, but they provide lesser flux density than that of the NdFeB and SmCo magnets. Interior PM design showed better performance than flux squeeze design for ferrite magnets due to availability of reluctance torque.

In the future work, transient thermal analysis of the machine may be explored to find out actual machine temperature for a specific driving cycle. Experimental work to test the performance and efficient control of three machines designed and built with different magnets, may also be undertaken as future work.

8.4 Losses and Torque Calculation of IPMSMs Using MEC

A numerical method based on a MEC model was developed for the calculation of iron and magnet losses and torque of IPMSMs. Starting from the basic geometry, winding configuration and input currents of the machine, a system of non-linear equations was derived and solved in the time domain for the MSP of the nodes. The system of equations is non-linear, and it was solved iteratively at each time step using the BH data points of the iron core material. The flux density in each element was calculated from the MSP of the nodes, and this led to the calculation of the iron and magnet losses of the machine.

The results of the proposed method were compared to those obtained using FEM. The results are comparable and the proposed method requires much less time for calculation of iron losses and torque than the FEM. Therefore the suggested method can be useful for early sizing and efficiency comparison of several machine designs in reduced time. The MEC model of a machine can be developed easily from its geometry, thus shortening the total computation time. Furthermore, the dimensions of elements for each run can be generated automatically through parametrization, that can be explored in the future work of this task.

APPENDICES

APPENDIX A

Experimental Work

This appendix describes the activities and information related to the PMSMs that were designed, built and tested during this research work.

A.1 20 kW Lab Model IPMSM

Initially, an IPMSM was designed and built locally to validate the design parameters and to run the control experiments. The machine was not built in regular housing, instead aluminium plates were used to provide housing structure for its operation in the lab environment. The machine has the following design parameters:

- NdFeB magnets
- Three phase
- 24 slots
- 4 poles
- Line voltage 480 V
- Stack length 101.6 mm
- Winding pitch of 120° electrical
- Double layer winding with 30 turns per coil of copper conductor AWG 14 or equivalent.

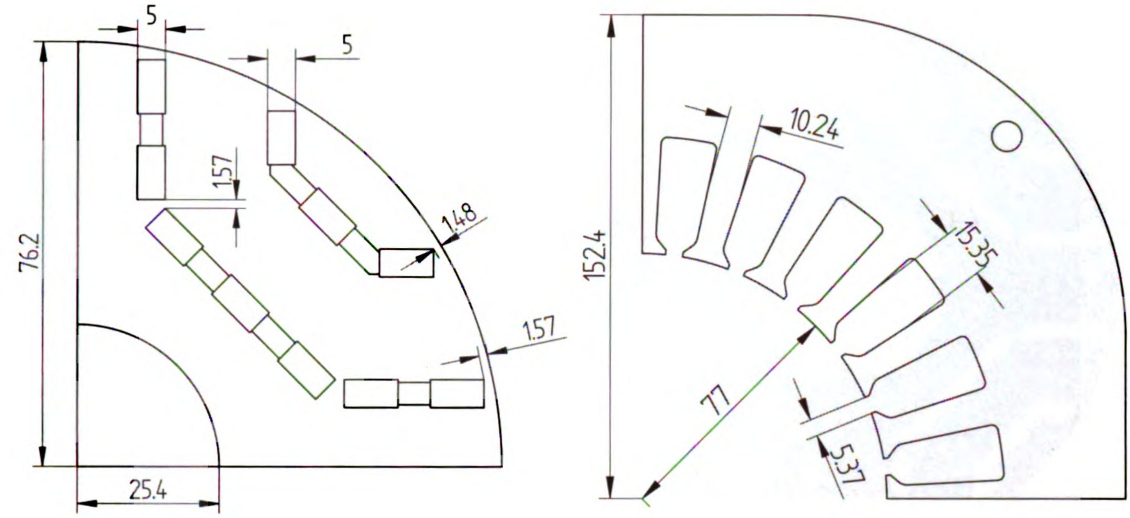

(a) Rotor (b) Stator

Figure A.1: Stator and rotor geometry for one pole of 20 kW NdFeB IPMSM

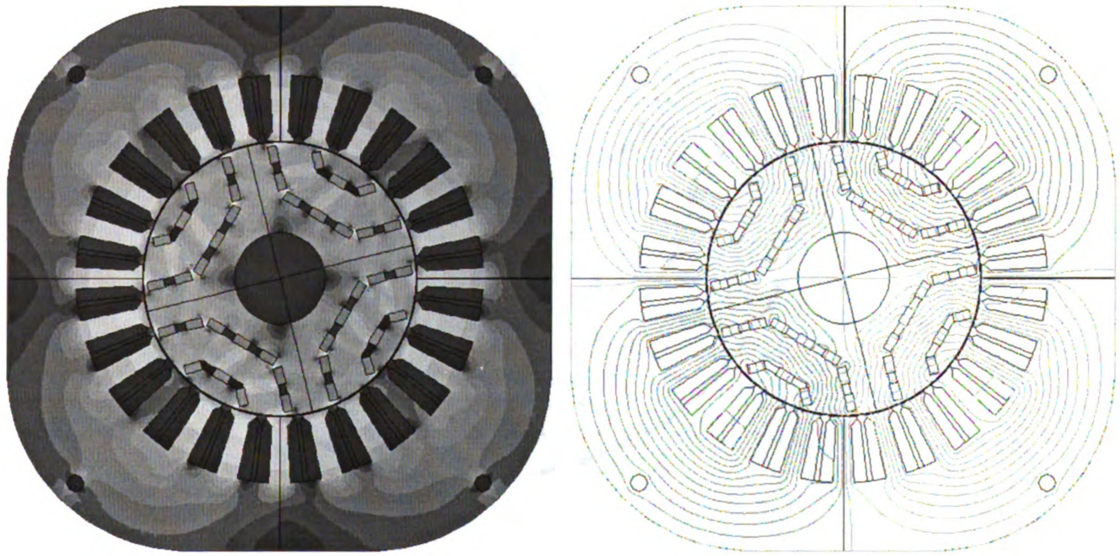

(a) Flux density (b) Flux paths

Figure A.2: 20 kW NdFeB IPMSM; FEM flux density and flux paths at rated current in q-axis

Fig. A.1 shows the geometry of the machine. All dimensions are in millimeters (mm).

Fig. A.2 shows FEM results of flux density and flux path in the machine, when rated current was applied along q-axis of the machine. Fig. A.3 shows stator and rotor lamina-

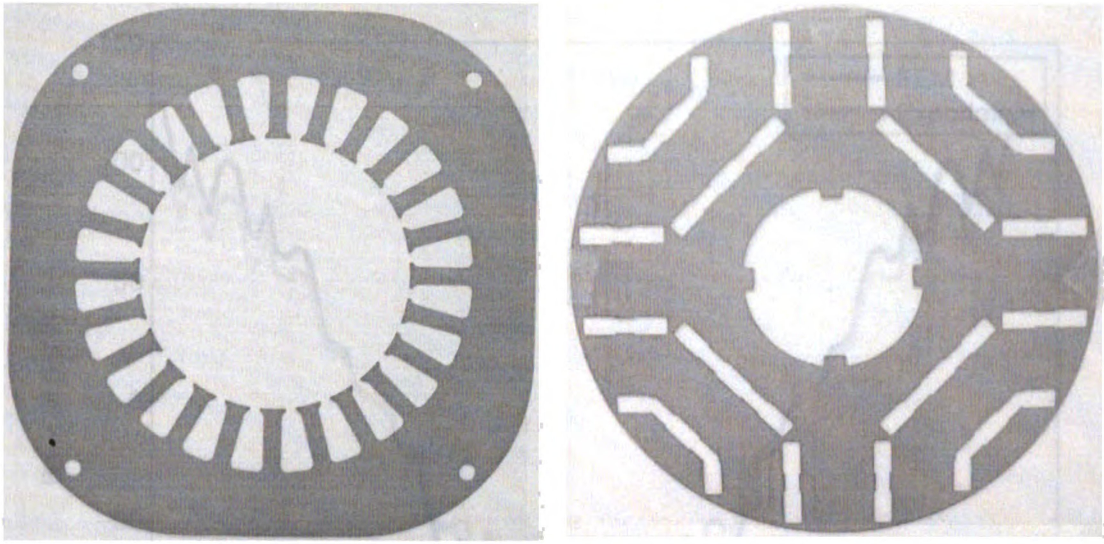

(a) Stator (b) Rotor

Figure A.3: Stator and rotor laminations of 20 kW NdFeB IPMSM

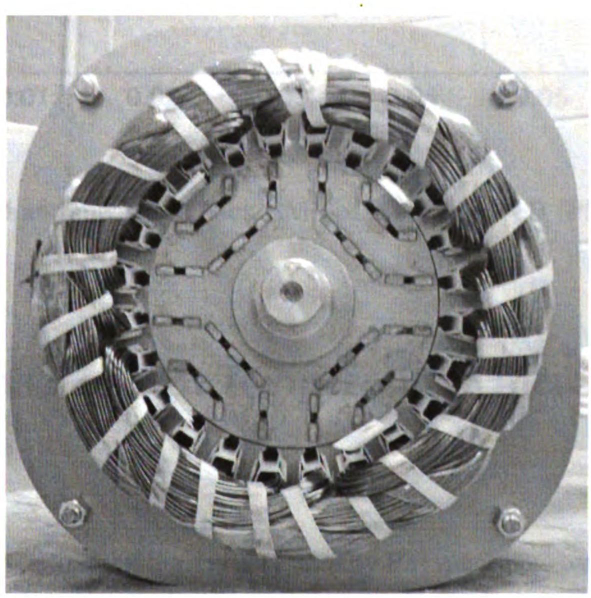

Figure A.4: Assembly of 20 kW NdFeB IPMSM

tions. Fig.A.4 exhibits the assembly of the machine, when permanent magnet rotor was installed in the stator. Fig. A.5 shows the FEM and measured back EMF. The difference is about 15 % and it might be due to the collar of mild steel rotor shaft that provides path for leakage flux of the permanent magnets.

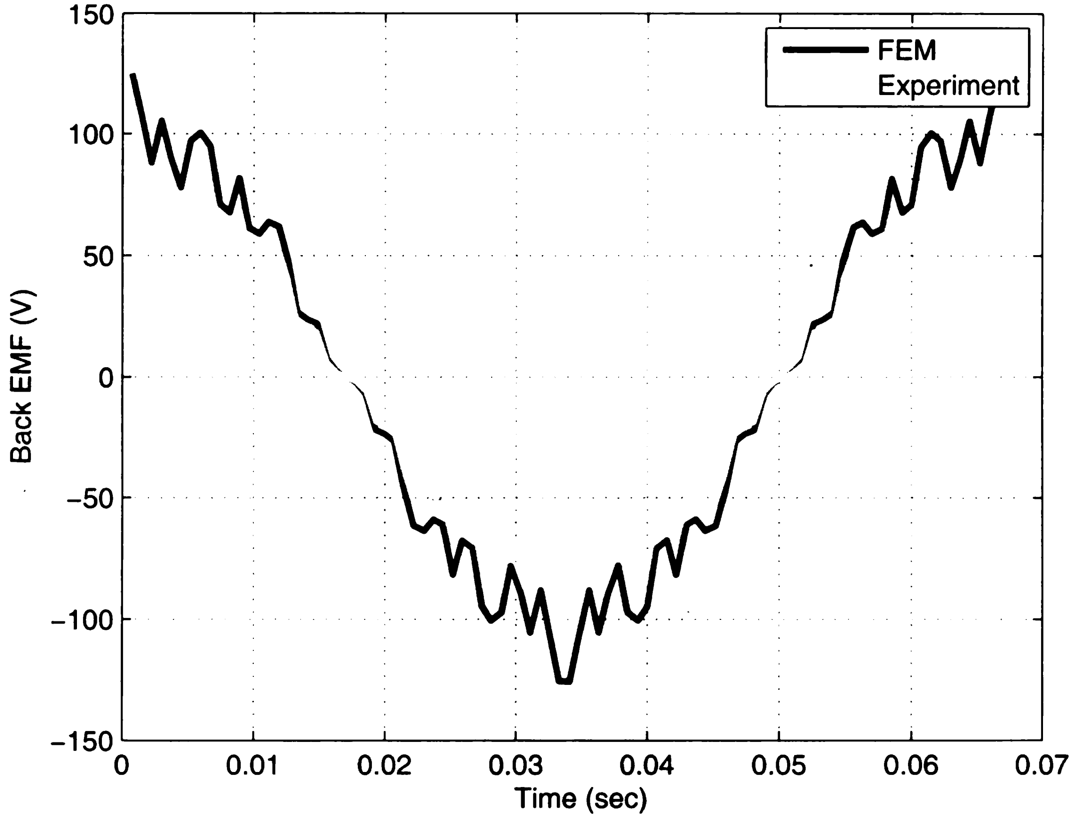

Figure A.5: FEM and measured back EMF of 20 kW NdFeB IPMSM at 450 rpm

A.2 Machines for High Temperature Operation

To evaluate the design options of high power density PM machines for the hybrid bus application and intended for high temperature operation, scaled down models of the bus driving machines are designed, built and tested using NdFeB and SmCo magnets. Additionally, the machine design options without using rare earth magnet materials was also explored and a flux squeeze PM machine with ferrite magnets is designed to build. To reduce the cost of manufacturing of housing for customized prototype machines, these three machines are built in the housing of commercially available 3 kW induction machine.

A.2.1 10 kW NdFeB machine

Fig. A.6 shows the geometry of the 10 kW NdFeB machine. It has the following design parameters:

- NdFeB magnets
- Three phase
- 24 slots
- 4 poles
- Line voltage 480 V
- Stack length 72 mm
- Winding pitch of 150° electrical
- Double layer winding with 32 turns per coil of copper conductor AWG 16 or equivalent.

Fig. A.7 shows the FEM results of flux density and flux paths at rated current applied in q-axis. Fig. A.8 shows the stator and rotor laminations stacks.

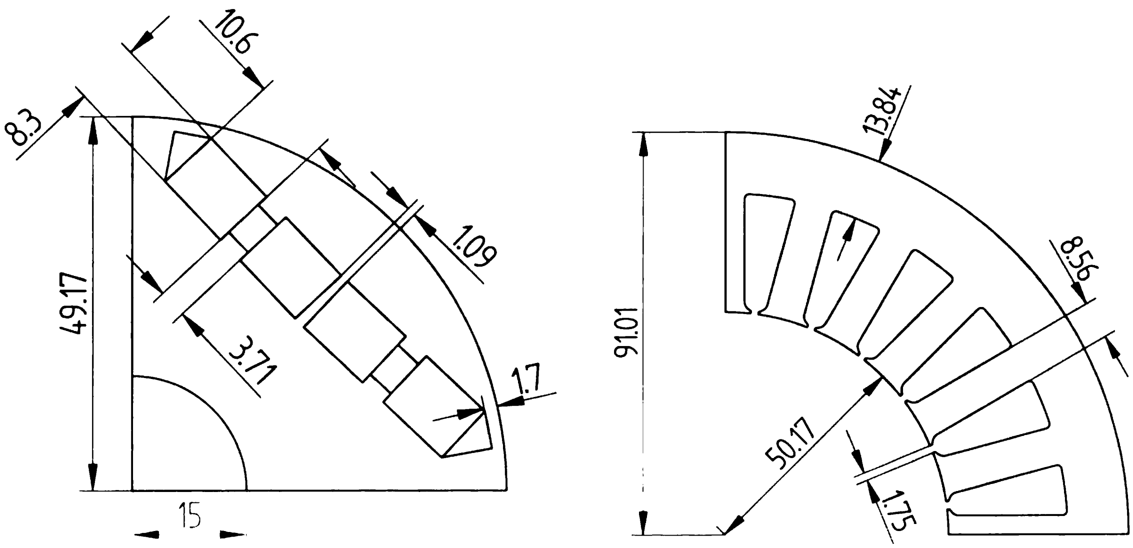

(a) Rotor (b) Stator

Figure A.6: Stator and rotor geometry for one pole of 10 kW NdFeB IPMSM

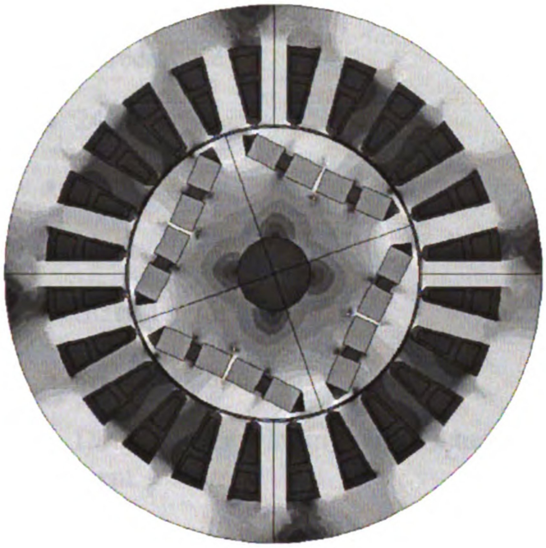

(a) Flux density

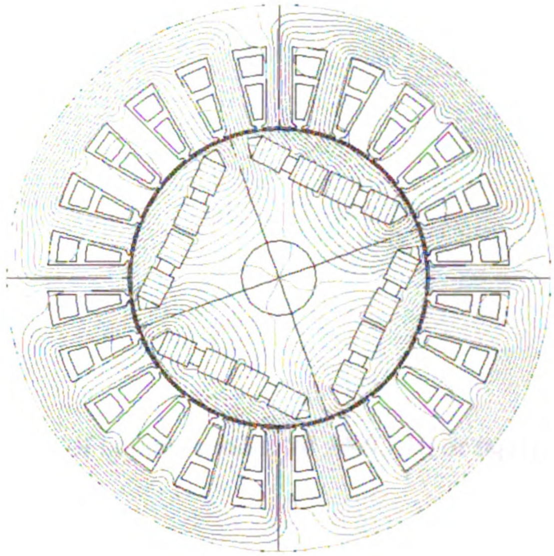

(b) Flux paths

Figure A.7: 10 kW NdFeB IPMSM; FEM flux density and flux paths at rated current in q-axis

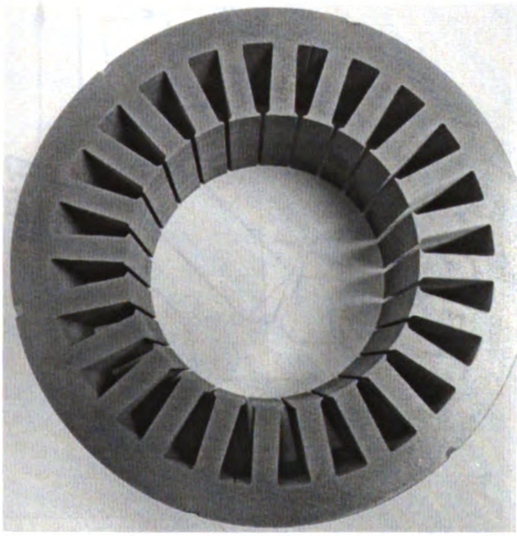

(a) Stator

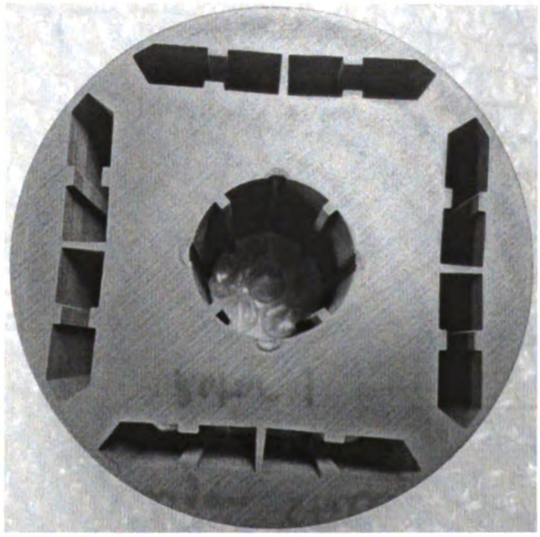

(b) Rotor

Figure A.8: Stator and rotor laminations stack of 10 kW NdFeB IPMSM

A.2.2 10 kW SmCo machine

Fig. A.9 shows the geometry of 10 kW SmCo machine. It has the following design parameters:

- SmCo magnets
- Three phase
- 24 slots
- 4 poles
- Line voltage 480 V
- Stack length 72 mm
- Winding pitch of 150° electrical
- Double layer winding with 32 turns per coil of copper conductor AWG 16 or equivalent.

Fig. A.10 shows the FEM results of flux density and flux paths at rated current applied in q-axis. Fig. A.11 shows the stator and rotor laminations stacks.

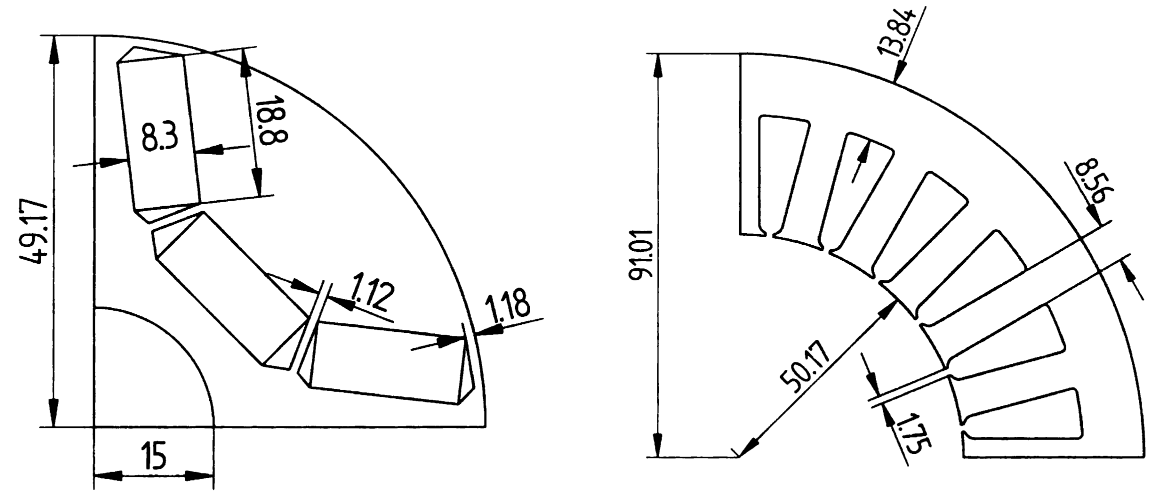

(a) Rotor (b) Stator

Figure A.9: Stator and rotor geometry for one pole of 10 kW SmCo IPMSM

A.2.3 6 kW ferrite machine

Fig. A.12 shows the geometry of 6 kW ferrite magnet machine. It has the following design parameters:

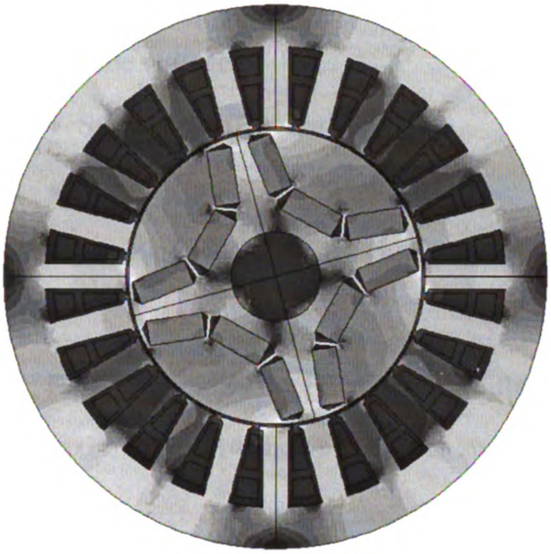

(a) Flux density

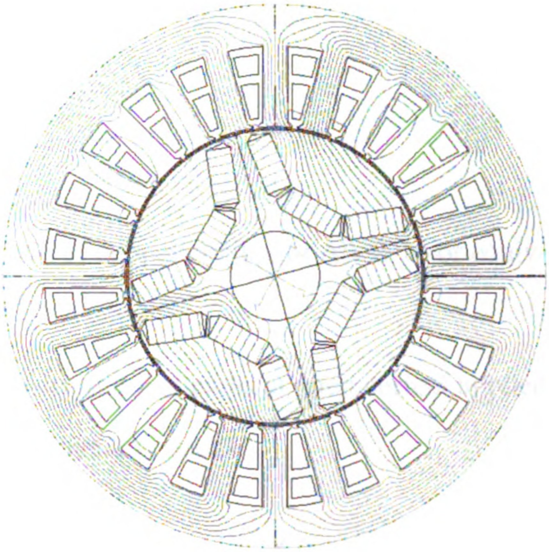

(b) Flux paths

Figure A.10: 10 kW SmCo IPMSM; FEM flux density and flux paths at rated current in q-axis

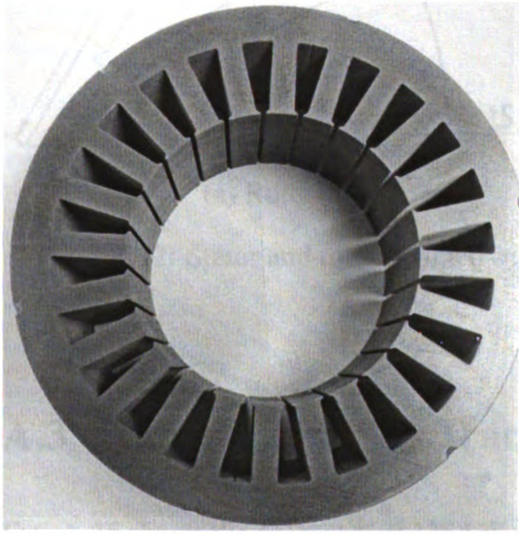

(a) Stator

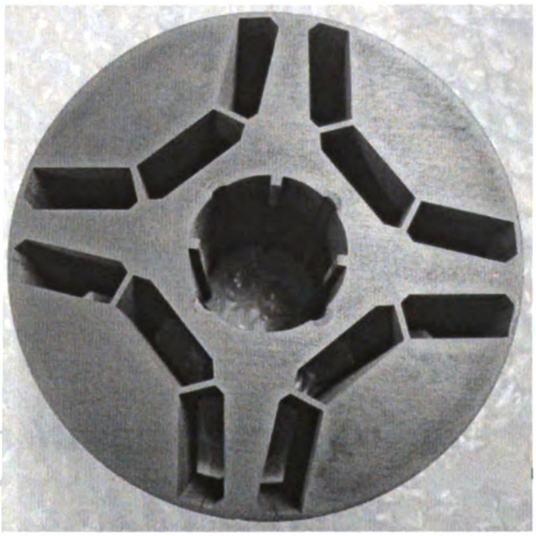

(b) Rotor

Figure A.11: Stator and rotor laminations stack of 10 kW SmCo IPMSM

- Ferrite magnets
- Three phase
- 36 slots

- 12 poles
- Line voltage 480 V
- Stack length 72 mm
- Winding pitch of 120° electrical
- Double layer winding with 27 turns per coil of copper conductor AWG 16 or equivalent.

Fig. A.13 shows the FEM results of flux density and flux paths at rated current applied in q-axis. Fig. A.14 shows the stator and rotor laminations stacks.

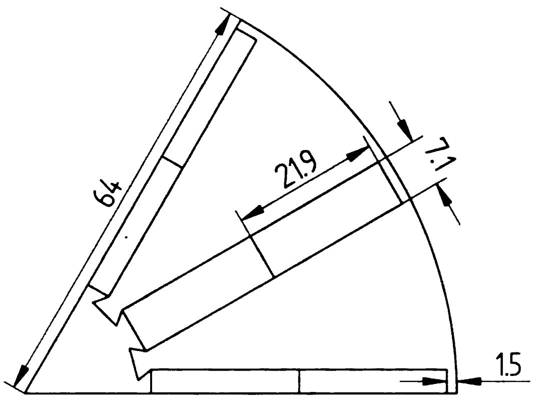

(a) Rotor

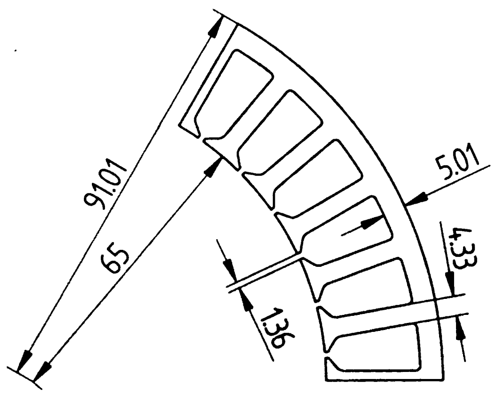

(b) Stator

Figure A.12: Stator and rotor geometry for a pole pair 6 kW flux squeeze ferrite PMSM

A.3 125 kW IPMSM Traction Machine for Hybrid Bus

Fig. A.15 shows the geometry of 125 kW water cooled IPMSM design for traction of series hybrid bus. The machine has following parameters:

- NdFeB magnets
- Three phase
- 24 slots
- 4 poles

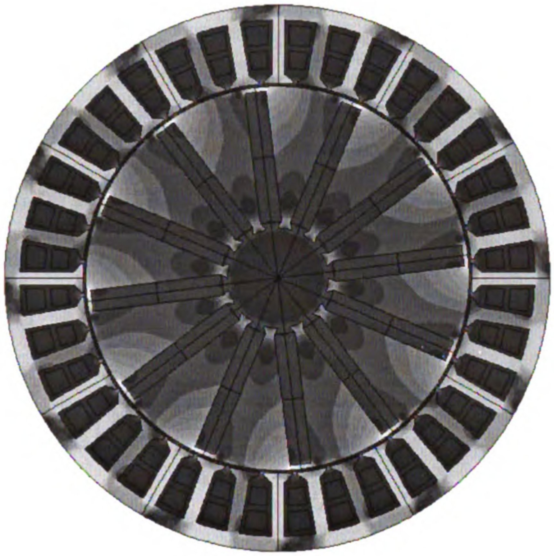

(a) Flux density

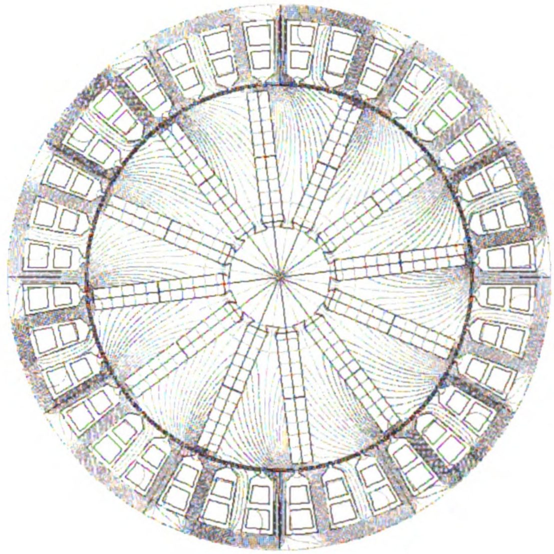

(b) Flux paths

Figure A.13: 6 kW flux squeeze ferrite PMSM; FEM flux density and flux paths at rated current in q-axis

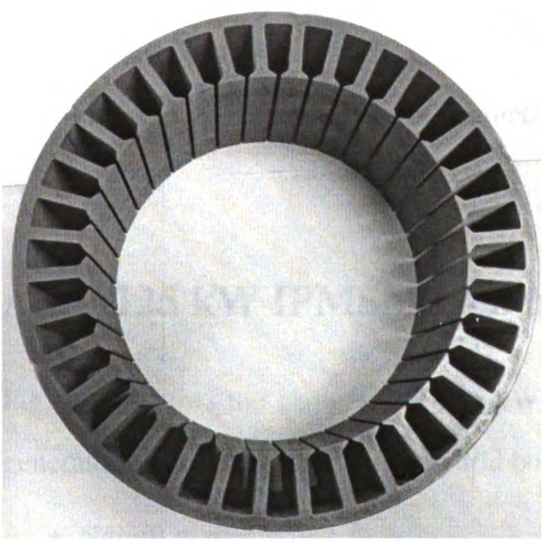

(a) Stator

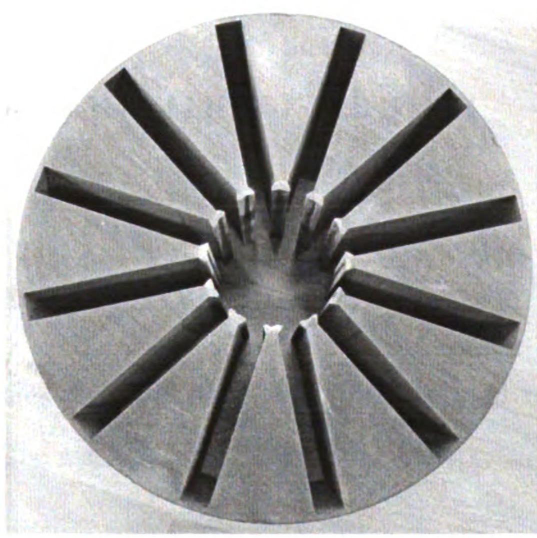

(b) Rotor

Figure A.14: Stator and rotor laminations stack 6 kW flux squeeze ferrite PMSM

- Line voltage 480 V
- Stack length 200 mm
- Winding pitch of 150° electrical

- Double layer winding with 6.5 turns per coil of copper conductor AWG 10 or equivalent.

Fig. A.16 shows the FEM results of flux density and flux paths at rated current applied in q-axis. Fig. A.17 shows the rotor lamination and its mandrel fixture to stack the laminations.

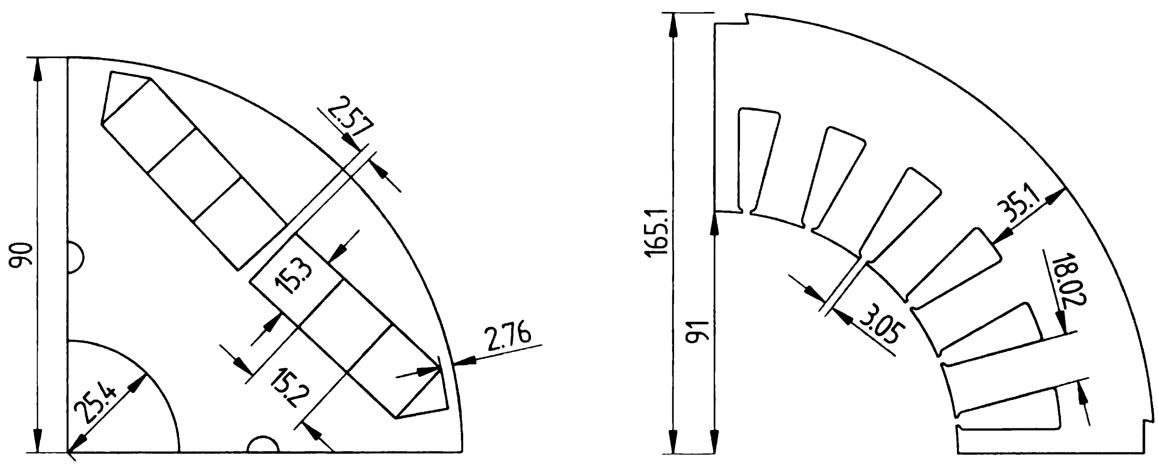

(a) Rotor (b) Stator

Figure A.15: Stator and rotor geometry for one pole of 125kW NdFeB IPMSM

A.4 125 kW IPMSM Generator for Hybrid Bus

Fig. A.18 shows the geometry of 125 kW water cooled IPMSM, which will be used as generator/engine starter for series hybrid bus. The machine has following parameters:

- NdFeB magnets
- Three phase
- 48 slots
- 8 poles
- Line voltage 480 V
- Stack length 150 mm

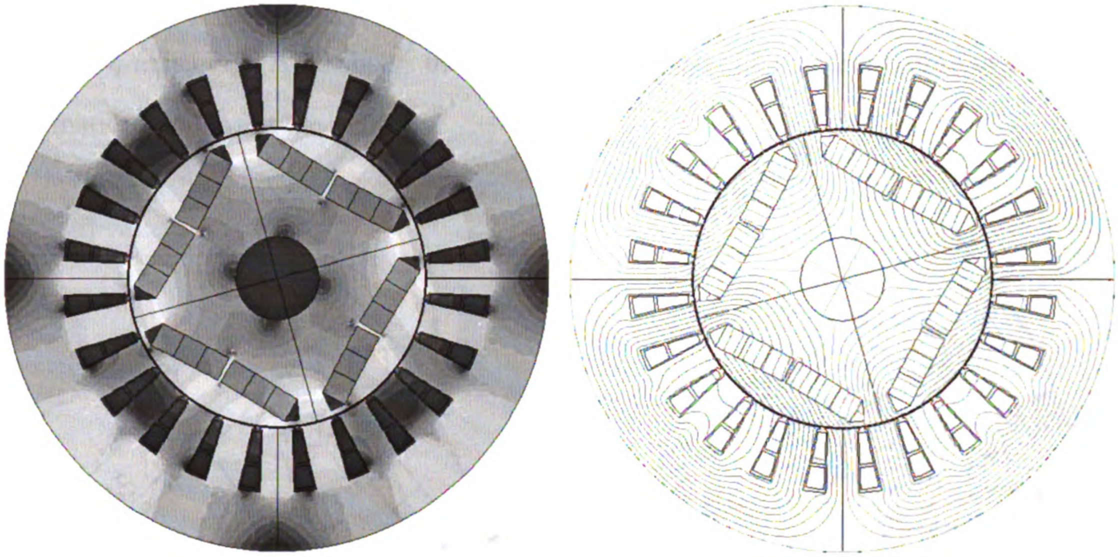

(a) Flux density (b) Flux paths

Figure A.16: 125kW NdFeB IPMSM; FEM flux density and flux paths at rated current in q-axis

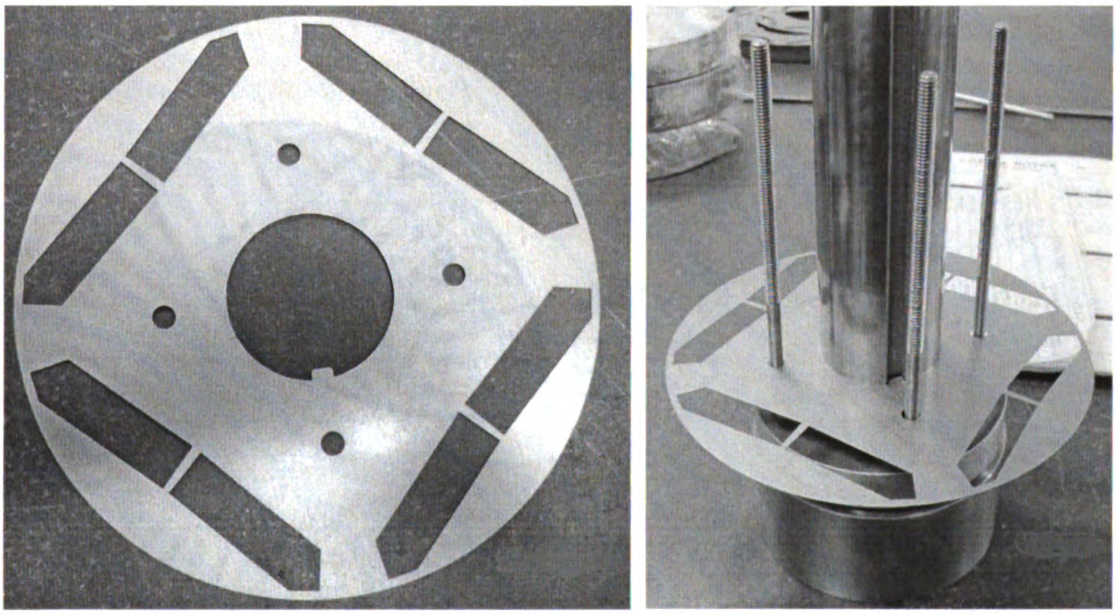

(a) Rotor (b) Rotor lamination stacking fixture

Figure A.17: Rotor laminations and its stacking fixture of 125kW NdFeB IPMSM

- Winding pitch of 150° electrical
- Double layer winding with 7 turns per coil of copper conductor AWG 7 or equivalent.

Fig. A.19 shows the FEM results of flux density and flux paths at rated current applied in q-axis. Fig. A.20 shows the rotor lamination and its mandrel fixture to stack the laminations and insert the magnets.

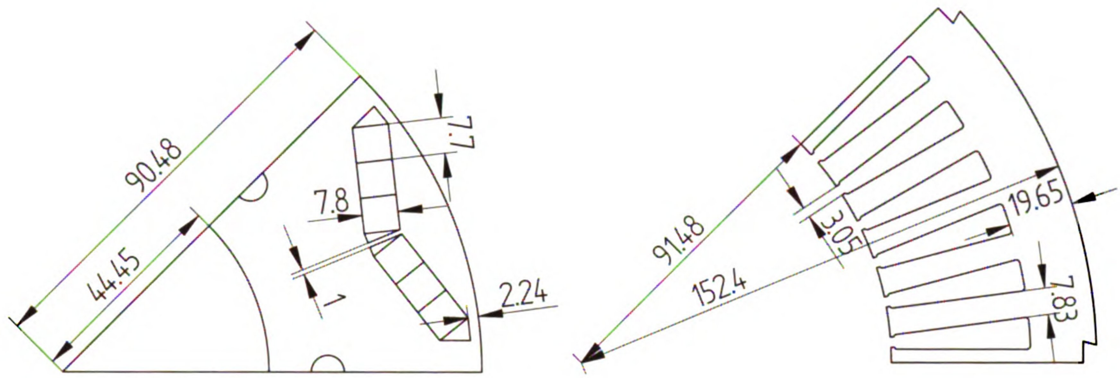

(a) Rotor (b) Stator

Figure A.18: Stator and rotor geometry for one pole of 125 kW NdFeB IPM generator

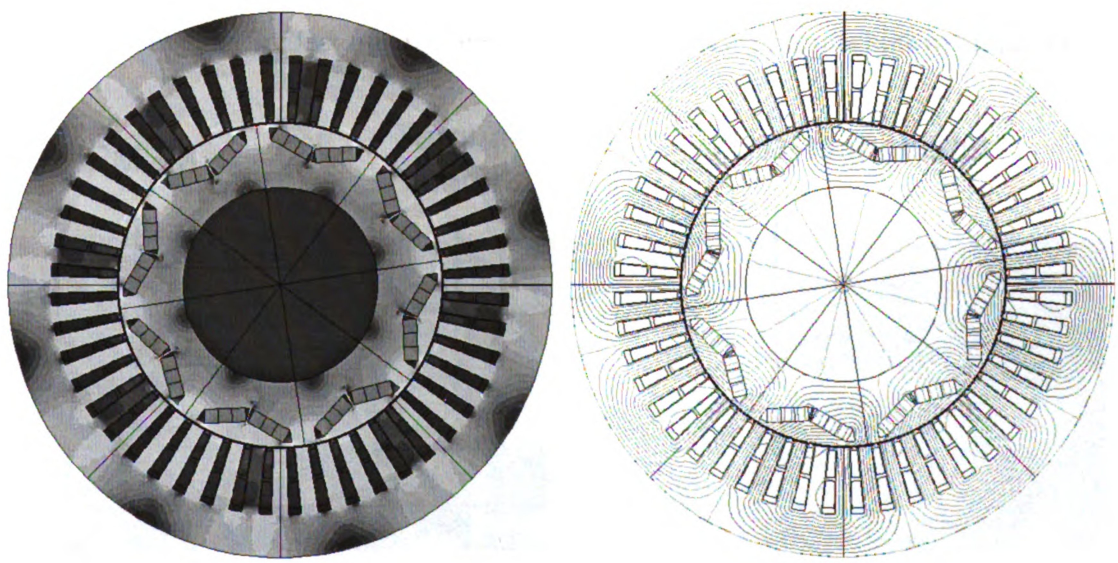

(a) Flux density (b) Flux paths

Figure A.19: 125 kW NdFeB IPM generator; FEM flux density and flux paths at rated current in q-axiss

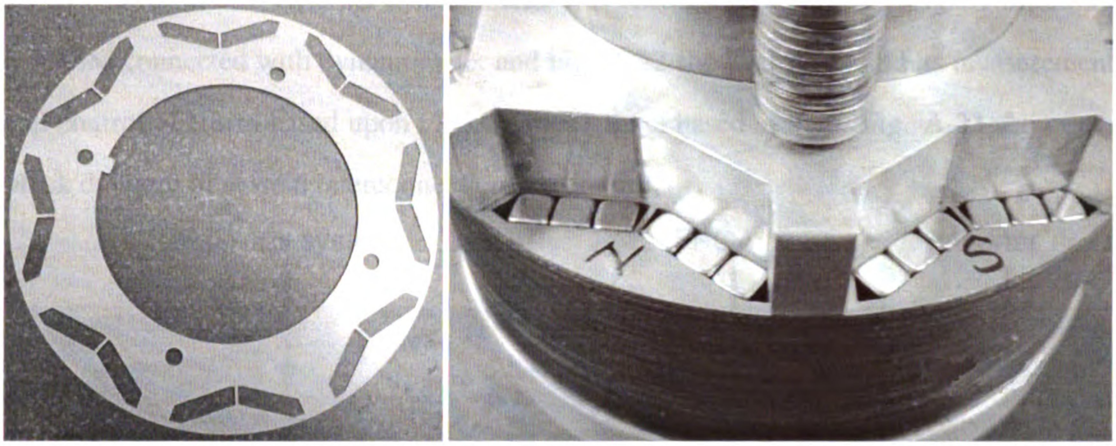

(a) Rotor (b) Rotor magnets installation fixture

Figure A.20: Rotor laminations and its stacking/magnets installation fixture of 125 kW NdFeB generator

A.5 Laboratory Test Setup for PMSMs

This section describes the experimental setup that was built to test and verify the parameters of manufactured PM machines. Two types of tests were planned for every machine; measurement of back Electromotive Force (EMF) and driving the machine in torque and/or

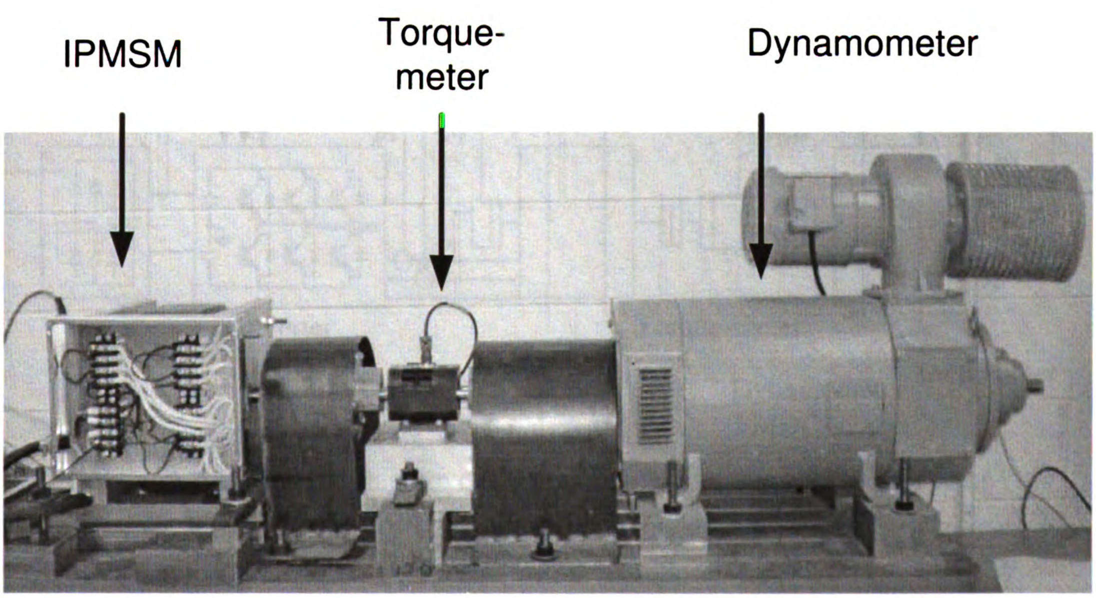

Figure A.21: PM machine and dynamometer

speed control mode. External dynamometer was used for this purpose. Fig. A.21 shows a PMSM connected with dynamometer and Fig. A.22 shows inverter and its measurement and control platform based upon FPGA and RT-linux based system. Fig. A.23 shows the block diagram of system interconnection and control.

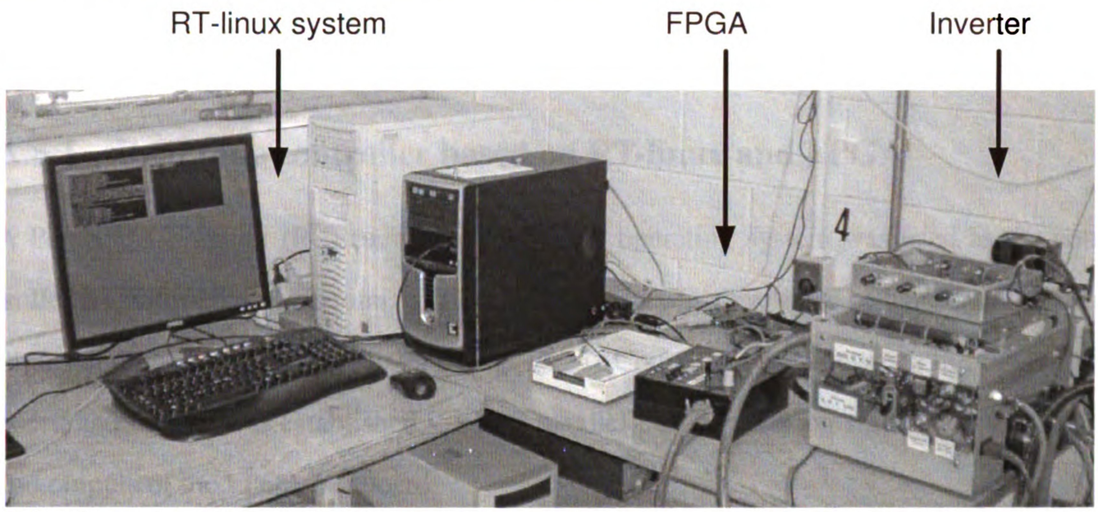

Figure A.22: Controller and inverter

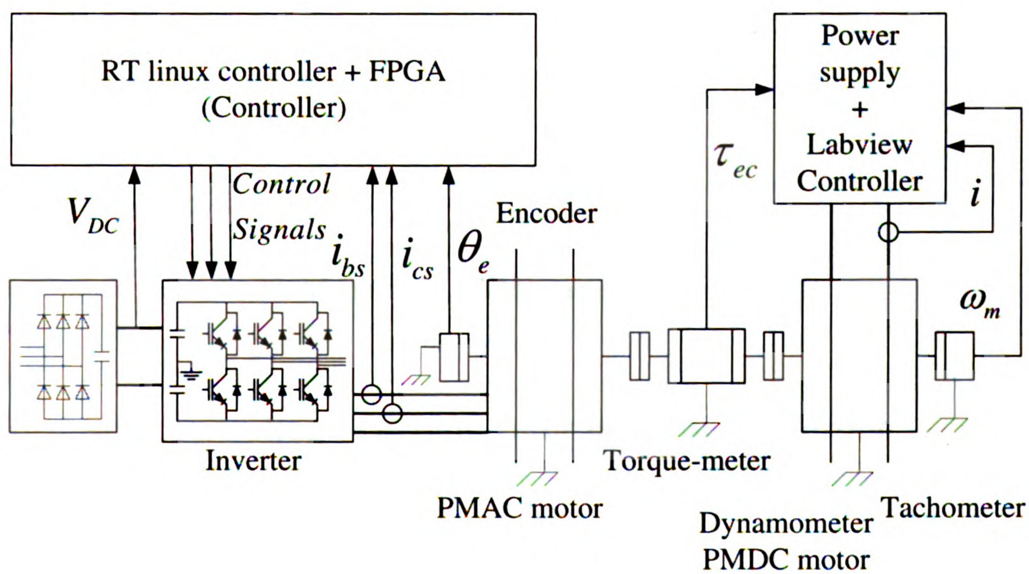

Figure A.23: Block diagram of system interconnection and control setup

The test setup developed is composed of the the following devices:

- Real time controller based on RT-linux and Field Programmable Gate Array (FPGA).

- Sensors: Voltage, current, rotor position and torque.
- Inverter.
- Dynamomceter and its control.
- PMSM under test.

A.5.1 Real time controller based on RT-linux and FPGA

A Personal Computer (PC) running on RT-linux operating system was used as the controller. A Xilinx based customized FPGA I/O board was developed to handle the control Inputs and Outputs (I/O) as shown in Fig. A.24. Communication between the FPGA I/O board and the PC was established via EPP parallel port. Following signals are the inputs and outputs of the FPGA I/O board.

- Measure: DC-link voltage.
- Measure: Phase currents.
- Measure: Phase voltage.
- Measure: Rotor position.
- Output: Pulse Width Modulated (PWM) pulses for inverter.

A.5.2 Sensors: voltage, current, rotor position and torque

Following sensors were used to acquire signals for measurement, control and analysis. Current and voltage sensors are shown in Fig. A.25

- Two phase currents were measured using current transducers LEM (LA-100p) with rated accuracy of 0.45% and bandwidth of 0-200kHz. The measured currents were used as feedback signal for control running in RT-linux.

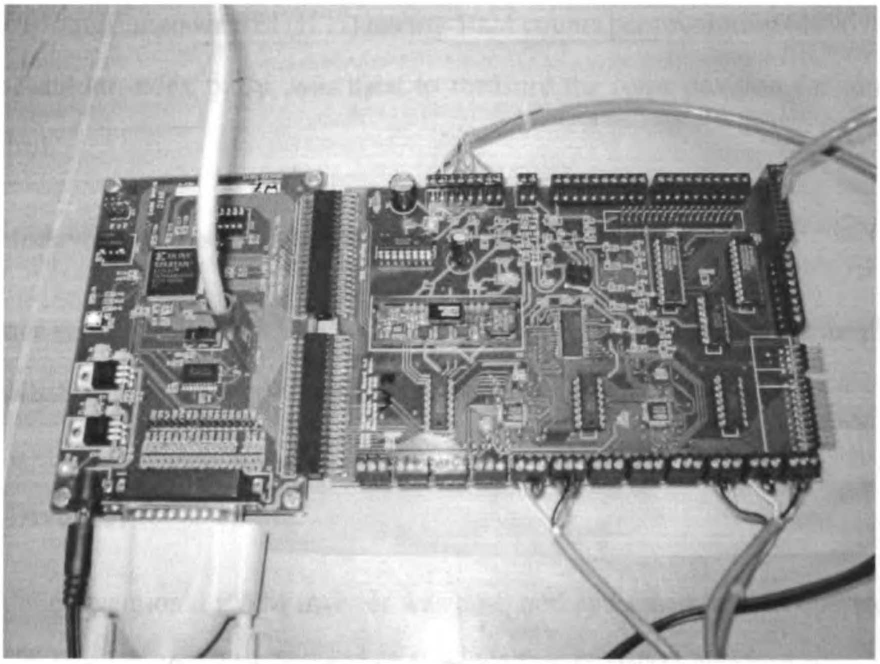

Figure A.24: FPGA and I/O board

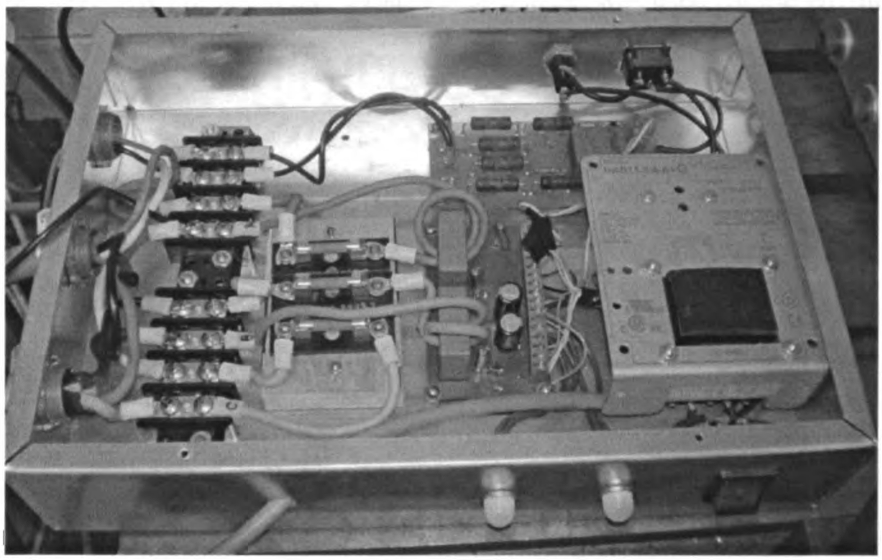

Figure A.25: Current and voltage sensors

- Phase voltage was measured using voltage transducer LEM (LV-25p) with rated accuracy of 0.45% and bandwidth of 0-200kHz. It was used to calibrate the rotor position sensor.

- A quadrature encoder BEI (H25) having 1024 counts per revolution (4096 for quadrature) and an index pulse, was used to measure the rotor position for torque/speed control.
- DC link voltage was measured with voltage sensor LEM (LV-100p).
- Torque sensor PCB (STS 5100) with a peak torque of 110 Nm with an amplifier PCB (SERIES 8159) was used to measure the shaft torque.

A.5.3 Inverter

A lab model conventional PWM inverter was designed and assembled to operate PMSMs as shown in Fig. A.26. The Integrated Power Module (IPM) selected was a Powerex (pm75cla120) with a rated voltage of 1200 V DC and a rated current of 75 A. The gate drive was Powerex BP7B. A bank of capacitor of 240 μF was used for the DC-link.

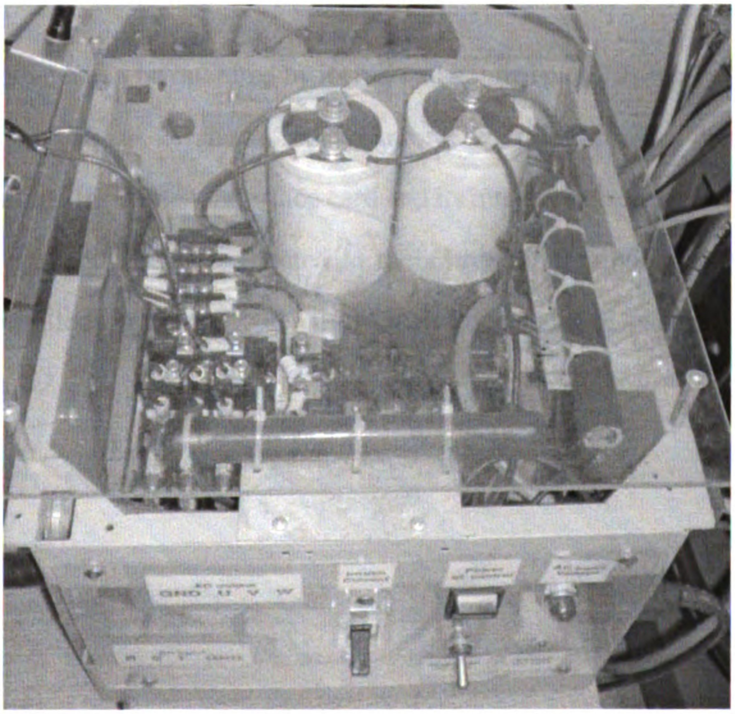

Figure A.26: Inverter

A.5.4 Dynamometer and its control

An Emerson dynamometer based on DC machine of 20 HP is used in the experiments to control the speed (or torque) of the test machine. The DC machine has a maximum current of 60 A, maximum voltage of 220 V and maximum torque of 80 Nm. It operates at a rated speed with full field of 1750 rpm, and during field weakening up to maximum speed of 2400 rpm.

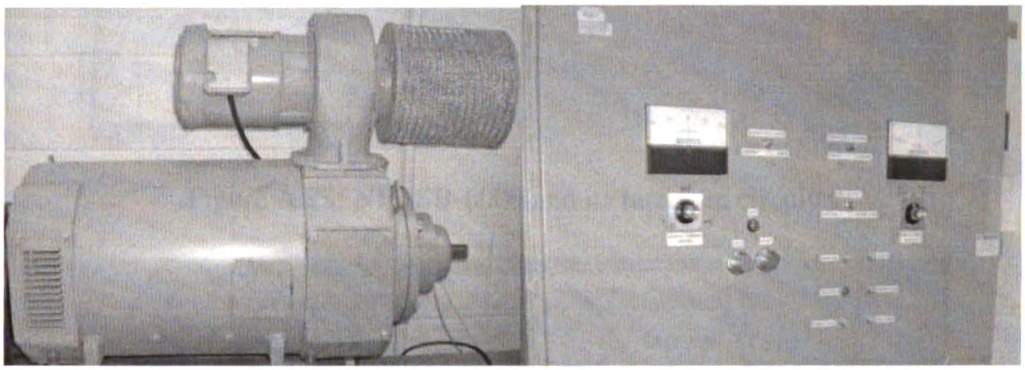

Figure A.27: Dynamometer and its manual control panel

The dynamometer can be operated by its manual control panel as well as through remote computer interface. Fig. A.27 shows the dynamometer and its manual control panel. Fig. A.28 shows National Instrument interface card and its interface circuitry that was developed for remote control, and it was connected to the computer through USB port. Lab-view software was installed on the PC and virtual instrument control panel was developed as shown in Fig. A.29.

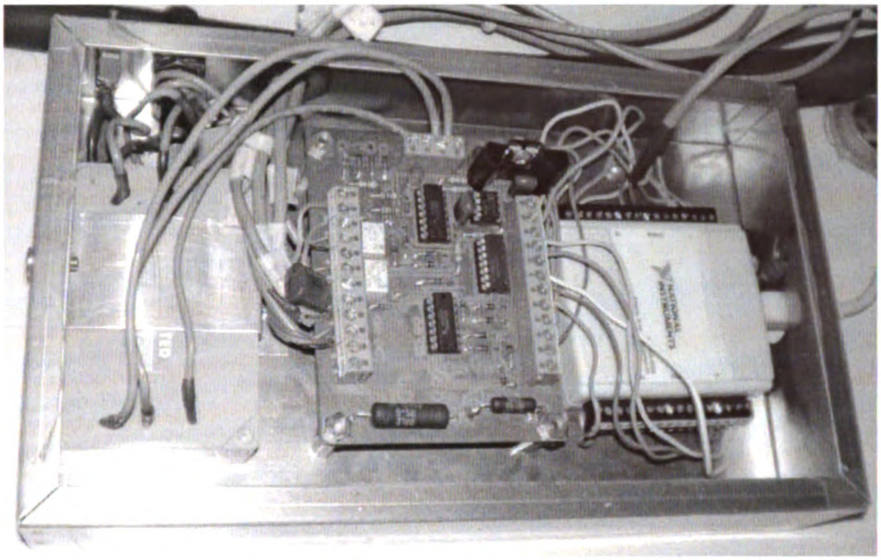

Figure A.28: NI USB-6009 and its interface circuitry

Figure A.29: Virtual instrument in the Lab-view

BIBLIOGRAPHY

BIBLIOGRAPHY

[1] R. Krishnan, *Electric Motor Drives Modelling, Analysis, and Control.* Prentice Hall, Inc., 2001.

[2] *Flux 10.3 2D Application User guide Volume 1-4.* CEDRAT GROUP, 2009.

[3] N. Chen, S. Ho, and W. Fu, "Optimization of permanent magnet surface shapes of electric motors for minimization of cogging torque using fem," *IEEE Transactions on Magnetics*, vol. 46, no. 6, pp. 2478 –2481, 2010.

[4] K. Yamazaki and H. Ishigami, "Rotor-shape optimization of interior-permanent-magnet motors to reduce harmonic iron losses," *IEEE Transactions on Industrial Electronics*, vol. 57, no. 1, pp. 61 –69, 2010.

[5] P. Niazi, H. Toliyat, and A. Goodarzi, "Robust maximum torque per amp (MTPA) control of PM-assisted synRM for tractions applications," in *IEEE Vehicle Power and Propulsion Conference, 2005*, Sept. 2005, pp. 624–630.

[6] C.-T. Pan and S.-M. Sue, "A linear maximum torque per ampere control for IPMSM drives over full-speed range," *IEEE Transactions on Energy Conversion*, vol. 20, no. 2, pp. 359–366, June 2005.

[7] P. Pillay and R. Krishnan, "Modeling of permanent magnet motor drives," *IEEE Transactions on Industrial Electronics*, vol. 35, no. 4, pp. 537–541, Nov 1988.

[8] C. Nino, A. Tariq, S. Jurkovic, and E. Strangas, "Optimal speed control of an interior permanent magnet synchronous motor including cross saturation," in *IEEE International Electric Machines and Drives Conference, 2009. IEMDC '09.*, May 2009, pp. 292–298.

[9] S. Williamson, M. Lukic, and A. Emadi, "Comprehensive drive train efficiency analysis of hybrid electric and fuel cell vehicles based on motor-controller efficiency modeling," *IEEE Transactions on Power Electronics*, vol. 21, no. 3, pp. 730 –740, May 2006.

[10] Z. Rahman, M. Ehsani, and K. L. Butler, "An investigation of electric motor drive characteristics for EV amd HEV propulsion systems," in *SAE International, Future Transportation Technology Conference & Exposition*, Aug. 2000.

[11] N. Schofield and C. Giraud-Audine, "Design procedure for brushless PM traction machines for electric vehicle applications," in *IEEE International Conference on Electric Machines and Drives, IEMDC '05*, May 2005, pp. 1788 –1792.

[12] N. Schofield, C. Giraud-Audine, D. Powell, and D. Howe, "Optimal design of permanent magnet brushless AC machines for electric vehicle applications," *International Journal of Applied Electromagnetics and Mechanics*, vol. 15, no. 1-4, pp. 143–148, 2001/2002.

[13] X. Liu, D. Diallo, and C. Marchand, "Cycle-based design methodology of hybrid electric vehicle powertrain: Application to fuel cell vehicles," in *IEEE Vehicle Power and Propulsion Conference, VPPC '09*, Sept. 2009, pp. 1853 –1857.

[14] Z. Rahman, K. L. Butler, and M. Ehsani, "A study of design issues on electrically peaking hybrid electric vehicle for diverse urban driving patterns," in *SAE International, International Congress & Exposition*, Mar. 1999.

[15] J. Gao, F. Sun, H. He, G. Zhu, and E. Strangas, "A comparative study of supervisory control strategies for a series hybrid electric vehicle," in *Asia-Pacific Power and Energy Engineering Conference, APPEEC' 2009*, Mar. 2009, pp. 1–7.

[16] K. Wipke and M. Cuddy. Using an advanced vehicle simulator ADVISOR to guide hybrid vehicle propulsion system developments. [Online]. Available: http://www.nrel.gov/docs/legosti/fy96/21615.pdf

[17] A. R. Tariq, C. E. Nino-Baron, and E. G. Strangas, "Overload considerations for design and operation of IPMSMs," *IEEE Transactions on Energy Conversion*, vol. 25, no. 4, pp. 921–930, Dec. 2010.

[18] Semikron Innovation and Service. (Sep. 2010) Semisel - simulation software version 3.1.1.3. [Online]. Available: http://semisel.semikron.com/Circuit.asp

[19] M. Kondo, Y. Shimizu, and J. Kawamura, "Development of totally enclosed permanent magnet synchronous motor," *Quarterly Report of RTRI*, vol. 49, no. 1, pp. 16–19, 2008.

[20] M. Negrea and M. Rosu, "Thermal analysis of a large permanent magnet synchronous motor for different permanent magnet rotor configurations," in *IEEE International Electric Machines and Drives Conference, IEMDC 2001.*, 2001, pp. 777–781.

[21] M. Rosu, A. Arkkio, T. Jokinen, J. Mantere, and J. Westerlund, "Demagnetisation state of permanent magnets in large output power permanent magnet synchronous motor," in *IEEE International Electric Machines and Drives Conference, IEMDC '99,*, May 1999, pp. 776–778.

[22] N. Demerdash, T. Nyamusa, and T. Nehl, "Comparison of effects of overload on parameters and performance of samarium-cobalt and strontium-ferrite radially oriented permanent magnet brushless dc motors," *IEEE Transactions on Power Apparatus and Systems*, vol. PAS-104, no. 8, pp. 2223–2231, Aug. 1985.

[23] J. Sprooten and J.-C. Maun, "Influence of saturation level on the effect of broken bars in induction motors using fundamental electromagnetic laws and finite element simulations," *IEEE Transactions on Energy Conversion*, vol. 24, no. 3, pp. 557–564, Sept. 2009.

[24] M. Aydin, S. Huang, and T. Lipo, "Optimum design and 3d finite element analysis of nonslotted and slotted internal rotor type axial flux pm disc machines," in *IEEE Power Engineering Society Summer Meeting, 2001*, vol. 3, 2001, pp. 1409–1416 vol.3.

[25] M. Dai, A. Keyhani, and T. Sebastian, "Torque ripple analysis of a pm brushless dc motor using finite element method," *IEEE Transactions on Energy Conversion*, vol. 19, no. 1, pp. 40–45, March 2004.

[26] A. Wang, H. Li, and C.-T. Liu, "On the material and temperature impacts of interior permanent magnet machine for electric vehicle applications," *IEEE Transactions on Magnetics*, vol. 44, no. 11, pp. 4329–4332, Nov. 2008.

[27] P. Lindh, H. Jussila, M. Niemela, A. Parviainen, and J. Pyrhonen, "Comparison of concentrated winding permanent magnet motors with embedded and surface-mounted rotor magnets," *IEEE Transactions on Magnetics*, vol. 45, no. 5, pp. 2085–2089, May 2009.

[28] N. Bianchi and A. Canova, "FEM analysis and optimisation design of an IPM synchronous motor," in *International Conference on Power Electronics, Machines and Drives, 2002.*, June 2002, pp. 49–54.

[29] T. Sebastian, "Temperature effects on torque production and efficiency of PM motors using NdFeB magnets," *IEEE Transactions on Industry Applications*, vol. 31, no. 2, pp. 353–357, Mar/Apr 1995.

[30] S. Constantinides. (Nov. 2009) Magnet selection. [Online]. Available: http://www.arnoldmagnetics.com/mtc/pdf/SteveC_Gorham_030923_Commented.pdf

[31] J. Liu and M. Walmer, "Thermal stability and performance data for smco 2:17 high-temperature magnets on ppm focusing structures," *IEEE Transactions on Electron Devices*, vol. 52, no. 5, pp. 899–902, May 2005.

[32] J. F. Gieras and M. Wing, *Permanent Magnet Motor Technology*. Marcel Dekker, Inc, 2002.

[33] K. Bradsher. (Oct. 2010) The New York Times, Global News : China Said to Widen Its Embargo of Minerals. [Online]. Available: http://www.nytimes.com/2010/10/20/business/global/20rare.html?_r=1\&hp

[34] J. R. Hendershot Jr. and T. J. E. Miller, *Design of Brushless Permanent Magnet Motors.* Magna Physics Publishing and Oxford University Press, 1994.

[35] M. Negrea and M. Rosu, "Thermal analysis of a large permanent magnet synchronous motor for different permanent magnet rotor configurations," in *IEEE International Electric Machines and Drives Conference, IEMDC 2001*, 2001, pp. 777–781.

[36] B. Stumberger, A. Hamler, M. Trlep, and M. Jesenik, "Analysis of interior permanent magnet synchronous motor designed for flux weakening operation," *IEEE Transactions on Magnetics*, vol. 37, no. 5, pp. 3644–3647, Sep 2001.

[37] C. Siguimoto, N. Sadowski, M. Luz, and C. Cezario, "Design and analysis of interior permanent magnet synchronous motors with optimized performance," in *18th International Conference on Electrical Machines, 2008. ICEM 2008.*, Sept. 2008, pp. 1–5.

[38] A. R. Tariq, C. E. Nino, and E. G. Strangas, "Effect of cooling conditions on the design and operation of IPMSM," in *IEEE Power and Energy Society General Meeting, 2009. PES GM '09.*, July 2009, pp. 1–10.

[39] J. M. Miller, *Propulsion Systems for Hybrid Vehicles.* The Institution of Electrical Engineers, 2004.

[40] V. Ostovic, *Dynamics of Saturated Electric Machines.* Springer-Verlag, 1989.

[41] A. Tariq, C. Nino, and E. Strangas, "A novel numerical method for the calculation of iron and magnet losses of IPMSMs," in *IEEE International Electric Machines and Drives Conference, 2009. IEMDC '09.*, May 2009, pp. 1605–1611.

[42] A. R. Tariq, C. E. Nino, and E. G. Strangas, "Iron and magnet losses and torque calculation of ipmsms using magnetic equivalent circuit," *IEEE Transactions on Magnetics*, vol. 46, no. 12, pp. 4073–4080, Dec. 2010.

[43] C. Mi, G. Slemon, and R. Bonert, "Modeling of iron losses of permanent-magnet synchronous motors," *IEEE Transactions on Industry Applications*, vol. 39, no. 3, pp. 734–742, May-June 2003.

[44] W. Roshen, "Iron loss model for permanent-magnet synchronous motors," *IEEE Transactions on Magnetics*, vol. 43, no. 8, pp. 3428–3434, Aug. 2007.

[45] E. Dlala, "A simplified iron loss model for laminated magnetic cores," *IEEE Transactions on Magnetics*, vol. 44, no. 11, pp. 3169–3172, Nov. 2008.

[46] W. Roshen, "Magnetic losses for non-sinusoidal waveforms found in AC motors," *IEEE Transactions on Power Electronics*, vol. 21, no. 4, pp. 1138 – 1141, Jul. 2006.

[47] W. A. Roshen, "A practical, accurate and very general core loss model for nonsinusoidal waveforms," *IEEE Transactions on Power Electronics*, vol. 22, no. 1, pp. 30 –40, Jan. 2007.

[48] K. Yamazaki and Y. Seto, "Iron loss analysis of interior permanent-magnet synchronous motors-variation of main loss factors due to driving condition," *IEEE Transactions on Industry Applications*, vol. 42, no. 4, pp. 1045–1052, July-Aug. 2006.

[49] J.-H. Seo, T.-K. Chung, C.-G. Lee, S.-Y. Jung, and H.-K. Jung, "Harmonic iron loss analysis of electrical machines for high-speed operation considering driving condition," *IEEE Transactions on Magnetics*, vol. 45, no. 10, pp. 4656–4659, Oct. 2009.

[50] A. Belahcen and A. Arkkio, "Comprehensive dynamic loss model of electrical steel applied to FE simulation of electrical machines," *IEEE Transactions on Magnetics*, vol. 44, no. 6, pp. 886–889, June 2008.

[51] T. J. E. Miller, *Combined user's manual for Windows version of SPEED Software*. Glasgow UK, SPEED Laboratory, University of Glasgow, 2007.

[52] J. K. Kim, S. W. Joo, S. C. Hahn, J. P. Hong, D. H. Kang, and D. H. Koo, "Static characteristics of linear BLDC motor using equivalent magnetic circuit and finite element method," *IEEE Transactions on Magnetics*, vol. 40, no. 2, pp. 742–745, March 2004.

[53] K. Nakamura, S. Fujio, and O. Ichinokura, "A method for calculating iron loss of an SR motor based on reluctance network analysis and comparison of symmetric and asymmetric excitation," *IEEE Transactions on Magnetics*, vol. 42, no. 10, pp. 3440–3442, Oct. 2006.

[54] J. Perho, "Reluctance netwrork for analysing induction machines," *Acta Polytechnica Scandinavica, Elect. Engg. Series No. 110, PhD Dissertation*, vol. 1, pp. 1–147, Dec. 2002.

[55] S. D. Sudhoff, B. T. Kuhn, K. A. Corzine, and B. T. Branecky, "Magnetic equivalent circuit modeling of induction motors," *IEEE Transactions on Energy Conversion*, vol. 22, no. 2, pp. 259–270, June 2007.

[56] M. Moallem and G. E. Dawson, "An improved magnetic equivalent circuit method for predicting the characteristics of highly saturated electromagnetic devices," *IEEE Transactions on Magnetics*, vol. 34, no. 5, pp. 3632–3635, Sep 1998.

[57] M. A. Batdorff and J. H. Lumkes, "High-fidelity magnetic equivalent circuit model for an axisymmetric electromagnetic actuator," *IEEE Transactions on Magnetics*, vol. 45, no. 8, pp. 3064–3072, Aug. 2009.

[58] M. Amrhein and P. T. Krein, "Force calculation in 3-D magnetic equivalent circuit networks with a maxwell stress tensor," *IEEE Transactions on Energy Conversion*, vol. 24, no. 3, pp. 587–593, Sept. 2009.

[59] ——, "3-D magnetic equivalent circuit framework for modeling electromechanical devices," *IEEE Transactions on Energy Conversion*, vol. 24, no. 2, pp. 397–405, June 2009.

[60] H. W. Derbas, J. M. Williams, A. Koenig, and S. D. Pekarek, "A comparison of nodal- and mesh-based magnetic equivalent circuit models," *IEEE Transactions on Energy Conversion*, vol. 24, no. 2, pp. 388–396, June 2009.

[61] Z. Zhu, Y. Pang, D. Howe, S. Iwasaki, R. Deodhar, and A. Pride, "Analysis of electromagnetic performance of flux-switching permanent-magnet machines by nonlinear adaptive lumped parameter magnetic circuit model," *IEEE Transactions on Magnetics*, vol. 41, no. 11, pp. 4277–4287, Nov. 2005.

[62] W. Soong, D. Staton, and T. Miller, "Validation of lumped-circuit and finite-element modelling of axially-laminated brushless motors," in *Sixth International Conference on Electrical Machines and Drives*, Sep 1993, pp. 85–90.

[63] E. Lovelace, T. Jahns, and J. Lang, "A saturating lumped-parameter model for an interior PM synchronous machine," *IEEE Transactions on Industry Applications*, vol. 38, no. 3, pp. 645–650, May/Jun 2002.

[64] L. Zhu, S. Z. Jiang, Z. Q. Zhu, and C. C. Chan, "Analytical modeling of open-circuit air-gap field distributions in multisegment and multilayer interior permanent-magnet machines," *IEEE Transactions on Magnetics*, vol. 45, no. 8, pp. 3121–3130, Aug. 2009.

[65] D. S. Watkins, *Fundamentals of Matrix Computations*. John Wiley and Sons Press, 2002.

[66] X. Wang, J. Li, and P. Song, "The calculation of eddy current losses density distribution in the permanent magnet of PMSM," in *2005 Asia Pacific Microwave Conference Proceedings, APMC 2005*, vol. 3, Dec. 2005, pp. 4 pp.–.

[67] A. Arkkio, "Time-stepping finite element analysis of induction motors," in *International Conference on Electrical Machines, ICEM' 88*, Sep 1988.

[68] N. Sadowski, Y. Lefevre, M. Lajoie-Mazenc, and J. Cros, "Finite element torque calculation in electrical machines while considering the movement," *IEEE Transactions on Magnetics*, vol. 28, no. 2, pp. 1410–1413, Mar 1992.